TWO NONLINEAR LATTICE PROBLEMS IN MATERIALS

by

Lifeng Liu

B. S. in Mathematics, University of Science and Technology of China, 2010

Submitted to the Graduate Faculty of

the Kenneth P. Dietrich School of Arts and Sciences in partial fulfillment

of the requirements for the degree of

Doctor of Philosophy

University of Pittsburgh

2015

UNIVERSITY OF PITTSBURGH

KENNETH P. DIETRICH SCHOOL OF ARTS AND SCIENCES

This dissertation was presented

by

Lifeng Liu

It was defended on

May 12, 2015

and approved by

Prof. Anna Vainchtein, Dept. of Mathematics, University of Pittsburgh

Prof. Dehua Wang, Dept. of Mathematics, University of Pittsburgh

Prof. Ming Chen, Dept. of Mathematics, University of Pittsburgh

Prof. Kaushik Dayal, Civil and Environmental Engineering, Carnegie Mellon University

Dissertation Director: Prof. Anna Vainchtein, Dept. of Mathematics, University of Pittsburgh

TWO NONLINEAR LATTICE PROBLEMS IN MATERIALS

Lifeng Liu, PhD

University of Pittsburgh, 2015

The interplay of spatial discreteness and nonlinearity plays an important role in the dynamics of nonlinear lattice systems, as illustrated by two problems considered in this thesis.

The first problem concerns kinetics of a step propagating along a twin boundary in a cubic lattice undergoing an antiplane shear deformation. To model twinning, we consider a piecewise quadratic double-well interaction potential with respect to one component of the shear strain and harmonic interaction with respect to another. We construct semi-analytical traveling wave solutions that correspond to a steady step propagation and obtain the kinetic relation between the applied stress and the velocity of the step. We show that this relation strongly depends on the width of the spinodal region where the double-well potential is nonconvex and on the material anisotropy parameter. In the limiting case when the spinodal region degenerates to a point, we construct new solutions that extend the kinetic relation obtained in the earlier work of Celli, Flytzanis and Ishioka into the low-velocity regime. Numerical simulations suggest stability of some of the obtained solutions, including low-velocity step motion when the spinodal region is sufficiently wide. When the applied stress is above a certain threshold, nucleation and steady propagation of multiple steps are observed.

In the second part of the thesis we explore a novel locally resonant granular material bearing harmonic internal resonators in a chain of beads interacting via Hertzian elastic contacts. Dynamics of the system can range from strongly to weakly nonlinear, depending on the solution amplitude and the amount of static precompression. We provide numerical and analytical evidence of the existence of discrete dark breathers solutions, exponentially

localized, time-periodic states mounted on top of a non-vanishing background. Our results are obtained by means of an asymptotic reduction to suitably modified versions of the discrete p-Schrödinger and nonlinear Schrödinger modulation equations in the strongly and weakly nonlinear regime, respectively. Stability and bifurcation structure of numerically computed exact dark breathers are examined. In some parameter regimes we also find small-amplitude periodic traveling waves, long-lived standing and traveling bright breathers, i.e., localized time-periodic solutions with exponentially decaying tails.

Keywords: lattice model, kinetic relation, twinning step, radiative damping, spinodal region, granular materials, resonators, discrete breathers, modulation equations, stability, bifurcation.

TABLE OF CONTENTS

LIST OF FIGURES

PREFACE

Pursuing this Ph.D. degree over the past five years has been a truly life-changing experience for me and I would like to give my sincere thanks to a great number of individuals who have made the memory so treasurable.

First and foremost, I would like to thank Professor Anna Vainchtein, my advisor and also a great collaborator, for her continued support throughout each stage of my graduate study. Anna is always available for help and advice in every aspect of my research journey. Without her guidance and encouragement, I never would have made it this far.

Many thanks also to my other research collaborators, Professor Panos Kevrekidis, Professor Guillaume James and Yangyang Wang, for generously sharing their time and ideas. I have learned much through our many constructive discussions.

I would also like to thank my dissertation committee of Professors Dehua Wang, Ming Chen and Kaushik Dayal, for their invaluable time and insightful comments.

I wish to thank all my fellow graduate students, faculty and staff members, all of whom have built this wonderful community. My deep appreciation goes to all my friends, who have helped me in countless ways. A special thank to my girlfriend, Jing, for her constant encouragement and support.

Finally, no words can properly express my gratitude to all my family members. I would like to say a heartfelt thank you to my parents, for their unconditional love along the way.

1.0 INTRODUCTION

The general theme of my thesis research is modeling and analysis of nonlinear phenomena in materials. In particular, I am interested in problems where the interplay of spatial discreteness and nonlinearity plays an important role in the dynamics of the system, which is described by nonlinear lattice differential equations. In this dissertation, I focus on two nonlinear lattice problems: kinetics of twinning steps in crystals and nonlinear waves in resonant granular materials.

1.1 KINETICS OF A TWINNING STEP

Deformation twinning is a phenomenon observed in many metals and alloys. A twin boundary separates two adjacent regions of a crystal lattice (two variants) that are related to one another by simple shear. Martensites, in particular, are known to form twinning microstructures under mechanical deformation [1]. Formation and motion of twin boundaries are responsible for the ability of these materials to accommodate very large deformations (up to 8-10% strain). A twin boundary propagates forward via the motion of steps, or ledges, along it [2–5]. Lattice dynamics of steps thus largely determines the macroscopic kinetics of a twin boundary [6, 7].

Chapter 2 describes the study of the kinetics of a twinning step in a cubic lattice, a project in collaboration with Yangyang Wang, a mathematics Ph.D. student, and my advisor Prof. Anna Vainchtein [8]. We assume that the lattice is undergoing an antiplane shear deformation, which reduces the problem to two dimensions with displacement field $u_{m,n}(t)$.

To model twinning in a way that captures the essential nonlinearity of the problem while allowing us to construct semi-analytical solutions, we consider a piecewise quadratic double-well interaction potential Φ with respect to one component of the shear strain and harmonic interaction with respect to another. The two wells represent two different twin variants and are separated by a *spinodal* region where the potential is nonconvex. The dimensionless equations of motion are then given by

$$\ddot{u}_{m,n} = \chi(u_{m+1,n} - 2u_{m,n} + u_{m-1,n}) + \Phi'(u_{m,n+1} - u_{m,n}) - \Phi'(u_{m,n} - u_{m,n-1}), \tag{1.1}$$

where $\ddot{u}_{m,n}$ denote the second time derivative of the displacement and the parameter χ measures the material anisotropy.

To find the *kinetic relation* between the applied stress and the velocity of the step, we construct semi-analytical traveling wave solution representing the steady motion of a twinning step at a given velocity and use this solution to compute the far-field stress necessary to maintain such motion. Following the approach developed in [9], we use Fourier transform methods and reduce the problem to a convolution-type linear integral equation that is solved numerically. We show that the resulting kinetic relation strongly depends on the width of the spinodal region and the material anisotropy. We also consider the singular limit when the width of the spinodal region tends to zero. This problem was studied in [10, 11] but in the earlier work no solutions were found at velocities below a certain threshold. We use the integral equation approach to construct new solutions in the low-velocity region below the threshold.

In addition to stability of sufficiently fast step propagation, numerical simulations of (1.1) suggest that slow step motion may become stable when the spinodal region is wide enough. As we show, a slowly moving step requires very small stress and emits short-length lattice waves that propagate both behind and ahead of the moving front. Meanwhile, fast step propagation takes place at higher stress and features lattice waves only behind the front. When the applied stress exceeds a certain critical value, the large amplitude of these waves causes island nucleation on top of a moving step, and the constructed solutions break down. Numerical simulations show cascade nucleation, growth and coalescence of multiple islands.

1.2 NONLINEAR WAVES IN A RESONANT GRANULAR CHAIN

Granular crystals are tightly packed arrays of solid particles that deform elastically upon contact via nonlinear Hertzian interactions [12–14]. The dynamics of these systems ranges from *weakly nonlinear*, when the initial overlap of the neighboring particles due to the static precompression is much larger than their relative displacement, to the *strongly nonlinear* regime characterized by relatively small or zero precompression. This provides an ideal setting for exploring nonlinear waves that emerge in granular materials. Among them, arguably, the most prototypical ones are traveling waves [12–14], shock waves [15,16] and exponentially localized (in space), periodic (in time) states that are referred to as *discrete breathers* [17–25].

Discrete breathers originate from the combined effects of nonlinearity and spatial discreteness. They constitute a generic excitation that emerges in a wide variety of systems and has been thoroughly reviewed [26, 27]. Discrete breathers can be divided into two distinct types, which are often referred to as *bright* and *dark* breathers. Bright breathers have tails in relative displacement decaying to zero and are known to exist in dimer (or more generally heterogeneous) granular chains with precompression [17, 23, 25], monatomic granular chains with defects [24] (see also [22]) and in Hertzian chains with harmonic onsite potential [20,21]. Dark breathers, on the other hand, are spatially modulated standing waves whose amplitude is constant at infinity and vanishes at the center of the chain (see Fig. 3.9, for example). Their existence, stability and bifurcation structure have been studied in a homogeneous granular chain under precompression [18]. Recently, experimental investigations utilizing laser Doppler vibrometry have systematically revealed the existence of such states in damped, driven granular chains in [19]. However, to the best of our knowledge, dark breathers have *not* been identified in a monatomic granular chain without precompression.

In a joint work with Professors Panos Kevrekidis (University of Massachusetts at Amherst), Guillaume James (Grenoble University) and Anna Vainchtein, we focus on a recent, yet already emerging as particularly interesting, modification of the standard granular chain, namely the so-called locally resonant granular chain. The latter belongs to a new type of granular "metamaterial" that has additional degrees of freedom and exhibits a very rich nonlinear dynamic behavior. In particular, in these systems it is possible to engineer tunable

band gaps, as well as to potentially utilize them for shock absorption and vibration mitigation. Such metamaterials have been recently designed and experimentally tested in the form of chains of spherical beads with internal linear resonators inside the primary beads (mass-in-mass chain) [28], granular chains with external ring resonators attached to the beads (mass-with-mass chain) [29] (see also [30]) and woodpile phononic crystals consisting of vertically stacked slender cylindrical rods in orthogonal contact [31]. An intriguing feature that has already been reported in such systems is the presence of weakly nonlinear solitary waves or nanoptera [32] (see also [33] for more detailed numerical results). Under certain conditions, each of these systems can be described by a granular chain with a secondary mass attached to each bead in the chain by a linear spring. The attached linear oscillator has the natural frequency of the internal resonator in the mass-in-mass chain (Fig. 1 in [28]), the piston normal vibration mode of the ring resonator attached to each bead in the mass-with-mass system (Fig. 9 in [29]) or the primary bending vibration mode of the cylindrical rods in the woodpile setup (Fig. 1 in [31]). The dimensionless equations of motion are

$$\ddot{u}_n = (\delta_0 + u_{n-1} - u_n)_+^\alpha - (\delta_0 + u_n - u_{n+1})_+^\alpha - \kappa(u_n - v_n), \quad \rho\ddot{v}_n = \kappa(u_n - v_n) \tag{1.2}$$

where $u_n(t)$ and $v_n(t)$ are the displacements of nth primary and secondary beads, respectively, $(x)_+ = x$ when $x > 0$ and equals zero otherwise, κ measures the relative strength of the linear elastic spring, $\rho = m_2/m_1$ is the ratio of two masses, α is the Hertzian nonlinear exponent which is equal to $3/2$ for spherical beads, and $\delta_0 \geq 0$ measures the amount of static precompression in the granular chain.

One of the particularly appealing characteristics of a locally resonant granular chain of this type is the fact that it possesses a number of special case limits that have previously been studied. More specifically, in the limit when the ratio of secondary to primary masses tends to zero, our model reduces to the non-resonant, homogeneous granular chain, while at a very large mass ratio and zero initial conditions for the secondary mass the system approaches a model of Newton's cradle [20, 21], a granular chain with quadratic onsite potential. We are interested in investigating the system's dynamics at finite ρ, when the equations are coupled, making the analysis more difficult.

In Chapter 3, we study the locally resonant granular chain in the absence of precompression. The dynamics of this system belongs to the strongly nonlinear regime, due to the fully nonlinear character of the interactions between beads. In particular, we prove that the non-attracting character of Hertzian interactions leads in this case to the non-existence of nontrivial bright breathers at finite mass ratio. Using a multiple-scale analysis and following the approach developed in [20], we derive the generalized modulation equations of discrete p-Schrödinger (DpS) type, which include a discrete p-Laplacian. The asymptotic DpS-type equations are then used to approximate various types of small-amplitude nonlinear waves existing in the system. First, we show that they capture the dynamics of the small-amplitude periodic traveling waves when the mass ratio is below a critical value. Second, in the case of large enough mass ratio and suitable small-amplitude initial data, we rigorously justify the validity of the limiting DpS equation derived in [20] on the long-time scale and use it to prove the existence of long-lived bright breather solutions in the system. Third, the generalized DpS equations are used to form initial conditions for numerical computation of dark breathers, whose stability and bifurcation structure are also examined. In addition, we identify the period-doubling bifurcations of these dark breather solutions at small mass ratios, as well as investigate their long-time instabilities that lead to steady motions and chaotic evolutions.

In Chapter 4, we consider the locally resonant granular chain under precompression. The precompression suppresses the fully nonlinear character of Hertztian interactions, to which a linear component is effectively added. At finite mass ratio, the dispersion relation for plane wave solutions of the linearized system has optical and acoustic branches. We identify the modulational instability of small-amplitude periodic waves that is typically responsible for breather formation in the weakly nonlinear regime. This is accomplished via derivation and analysis of modulation equations of nonlinear Schrödinger (NLS) type using multiple-scale techniques [34–36]. Depending on the wave number and the branch of the dispersion relation, the NLS equation is either *focusing*, admitting sech-type solutions, or *defocusing*, with tanh-type solutions. In particular, we analyze the focusing NLS and obtain numerical results suggesting that it approximates the dynamics of moving bright breathers quite well at various mass ratios and some wave numbers. We then use solutions of the defocusing NLS to

form initial conditions for numerical computation of exact dark breathers that bifurcate from both optical and acoustic branches. We show that the stability and bifurcation structure of the computed dark breathers are significantly affected by the mass ratio and breather frequency.

2.0 KINETICS OF A TWINNING STEP

In this chapter we study the kinetics of a single step propagating along the twin boundary. To model this phenomenon in the simplest setting, we consider antiplane shear deformation of a cubic lattice, with piecewise quadratic double-well interaction potential with respect to one component of the shear strain and harmonic interaction with respect to another. The two wells represent two different twin variants and are separated by a *spinodal* region where the potential is nonconvex. This is an extension of the model with bilinear interactions that was used in [37, 38] to study high-velocity dynamics of steps along a phase boundary and in [39], where their quasistatic evolution was considered. Piecewise linear interactions were assumed by many authors to describe propagation of phase boundaries, fracture and dislocations in a crystal lattice (see [9–11, 40–50] and references therein). The advantage of such models is that they allow a semi-analytical treatment through the application of Fourier transform, Wiener-Hopf technique and related methods.

To find the kinetic relation between the applied stress and the velocity of the step, we need to construct traveling wave solutions representing the steady motion of a twinning step. The problem trivially reduces to the uniform motion of a screw dislocation studied in [9] (see also [51, 52]), where it is shown that semi-analytical solutions can be obtained by solving a linear integral equation. The kernel of the integral equation is determined by the solution of the problem where spinodal region degenerates into a point, which was studied in [10, 11]; see also [40] for a closely related one-dimensional Frenkel-Kontorova (FK) model. Despite the long history of this problem, some important questions remained open. One of these questions is the existence and stability of the low-velocity motion. In fact, the work in [9, 51, 52] focused primarily on solutions at some fixed velocities in the medium to high range and their dependence on the width of the spinodal region, while the slow propagation

was not investigated. Here we use the approach in [9] to construct solutions for a wide range of velocities, including slow motion, and obtain the associated kinetic relation. We show that this relation strongly depends on the width of the spinodal region and the material anisotropy parameter given by the relative strength of the harmonic bonds. We then conduct numerical simulations to independently verify some of these results and test stability of the obtained solutions. We provide semi-analytical and numerical evidence that not only steady slow dislocation (step) motion exists, it may become stable when the spinodal region is sufficiently wide. Unlike the high-velocity motion, a slowly moving step requires very small stress and emits lattice waves that may propagate both behind and ahead of the moving front. Our work thus complements and extends the results in [9, 51, 52]. It also extends to the higher-dimensional case the work in [49], where a similar investigation was recently undertaken for the FK model.

We also revisit the limiting case when the spinodal region between the two wells degenerates into a single point (spinodal value). In this case the earlier work [10, 11] considered traveling wave solutions in which a transforming bond goes through the spinodal value at a single transition point, which means that it *instantaneously* switches from one well to another and remains there. While this assumption seems reasonable, it generates solutions only at relatively high velocities above a certain threshold value V_0 (and below another critical velocity where the solutions break down). Below V_0, the formally constructed solutions violate the assumption used to obtain them because the transforming bond crosses the spinodal value more than once. This implies that no traveling wave solutions of the form assumed in [10, 11] exist below the threshold value. The same non-existence result has been observed for the Frenkel-Kontorova model [40, 43]. Meanwhile, the results obtained for the models with a non-degenerate spinodal region, both the one studied here and its FK counterpart in [49], suggest that at velocities below V_0 the time interval during which a transforming bond remains in the spinodal region approaches a *nonzero* value as the spinodal region shrinks to a point. This motivated the work [53] for the FK model, where a new type of solutions below the threshold velocity was recently constructed by extending the approach developed in [9] to this limiting case and allowing the transforming bonds to stay at the spinodal value for a *finite* time before switching into another well. Here we apply this idea to the present model

and show that the same result holds. The new solutions fill in the low-velocity gap in the kinetic relation left by the analysis in [10, 11], although, as in [53], they are likely unstable.

Finally, we investigate the solution breakdown at sufficiently high velocities when the amplitude of the lattice waves emitted by a moving step becomes sufficiently large and leads to cascade nucleation, growth and coalescence of islands on top of the existing step. The boundaries of the new islands and the initial step eventually propagate with the same velocity. These results extend the analysis in [38] to the case with a non-degenerate spinodal region, where the island nucleation is no longer instantaneous, and support the dynamic twin nucleation and growth mechanism that was predicted in [54] and studied numerically in [55, 56].

This chapter is organized as follows. Section 2.1 introduces the model, and the solution procedure is summarized in Section 2.2. In Section 2.3 we discuss the admissibility of solutions, obtain the kinetic relation and analyze its dependence on the width of the spinodal region and the material anisotropy parameter. The new solutions for the case of the degenerate spinodal region are obtained and discussed in Section 2.4. In Section 2.5 we numerically investigate stability of the obtained solutions, and some concluding remarks can be found in Section 2.6. Some additional technical results are contained in the Appendix A and B.

2.1 THE MODEL

Consider a three-dimensional cubic lattice with an orthonormal basis $\{\mathbf{e_1}, \mathbf{e_2}, \mathbf{e_3}\}$ undergoing an antiplane shear deformation, which means that the atomic rows parallel to the $\mathbf{e_3}$-direction are rigid and can only move along their length. Let $u_{m,n}(t)$ denote the displacement of (m, n)th row at time t. We assume that each row interacts with its four nearest neighbors. The interaction potentials between the neighboring rows in the horizontal (m) and vertical (n) directions are given by $\Psi(e)$ and $\Phi(y)$, where e and y denote the corresponding components of the shear strain. The equations of motion are then given by the infinite

system of ordinary differential equations:

$$\begin{aligned}\frac{d^2}{dt^2}u_{m,n}(t) = \Psi'(u_{m+1,n}(t) - u_{m,n}(t)) - \Psi'(u_{m,n}(t) - u_{m-1,n}(t)) \\ + \Phi'(u_{m,n+1}(t) - u_{m,n}(t)) - \Phi'(u_{m,n}(t) - u_{m,n-1}(t)).\end{aligned} \tag{2.1}$$

Here all variables are dimensionless after an appropriate rescaling [37].

To model twinning, we assume that the bonds in the vertical direction are governed by a double-well potential, with a continuous *trilinear* derivative:

$$\Phi'(y) = \begin{cases} y + 1, & y < -\delta/2 \quad \text{(variant I)} \\ (1 - 2/\delta)y, & |y| \le \delta/2 \quad \text{(spinodal region)} \\ y - 1, & y > \delta/2 \quad \text{(variant II)} \end{cases} \tag{2.2}$$

The two symmetric quadratic wells of $\Phi(y)$ correspond to two different twin variants I and II and are connected by a downward parabola that represents the spinodal region of width δ such that $0 < \delta < 2$ (see Figure 2.1). In what follows, we will also separately consider the limiting case $\delta = 0$ when the spinodal region degenerates to a single point, and $\Phi'(y)$ becomes *bilinear*, $\Phi'(y) = y \pm 1$, $y \lesseqgtr 0$. We further assume that the elastic interactions between the nearest neighbors in the horizontal bonds are linear:

$$\Psi'(e) = \chi e. \tag{2.3}$$

Here $\chi > 0$ is the dimensionless parameter measuring the anisotropy of the lattice. We note that while in general the interaction potentials are periodic, with alternating slip and twinning energy barriers, here we assume that the energy barrier for twinning is much lower than the one for slip, as is the case, for example, in Cu-Al-Ni alloy [6], so it suffices to consider only two wells. On the continuum level, constitutive laws similar to the one assumed here were used to model twinning in [57, 58].

Suppose now that a twin boundary containing a single step divides the lattice into two regions, as shown in Figure 2.2. The vertical bonds in the blue region are in variant II, the bonds in the red region are in variant I, and there are possibly also some bonds near the step front that have spinodal strain values (the green region). As the step propagates from left to right along the twin boundary, the spinodal (green) bonds switch to variant II (blue),

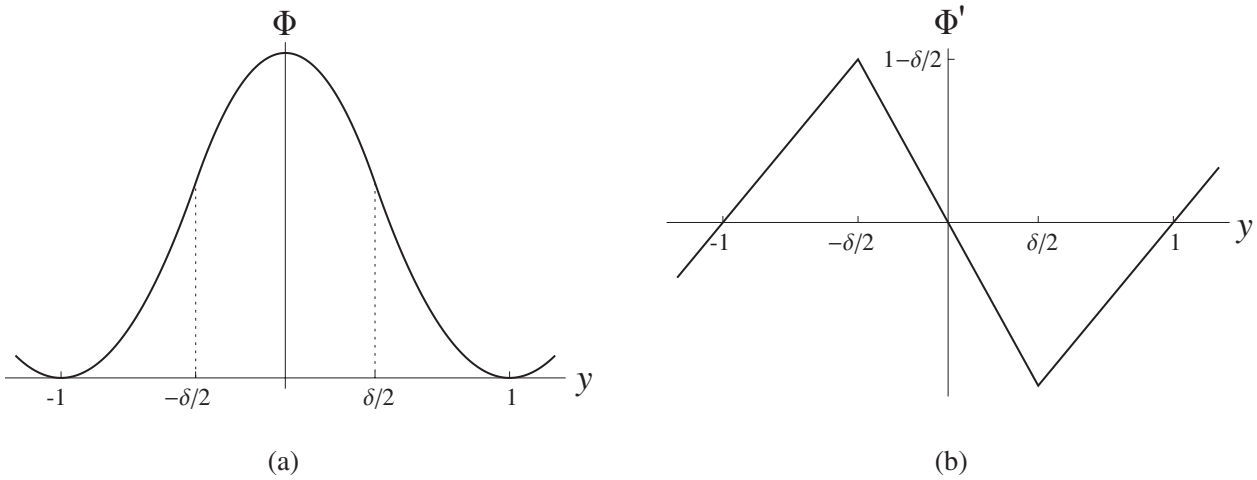

Figure 2.1: The double-well quadratic potential $\Phi(y)$ and its derivative (2.2).

and the variant I (red) bonds switch to the spinodal region (green) and later to variant II. In what follows, we will consider traveling wave solutions describing a steady step propagation and obtain the corresponding *kinetic relations* between the applied stress and the velocity of the step.

2.2 TRAVELING WAVE SOLUTION

To model a steadily moving step front along the twin boundary, we seek solutions of (2.1) in the form of a traveling wave with (constant) velocity $V > 0$:

$$u_{m,n}(t) = u(\xi, n), \quad \xi = m - Vt. \tag{2.4}$$

The vertical strains $y_{m,n}(t) = u_{m,n}(t) - u_{m,n-1}(t)$ are then given by

$$y_{m,n}(t) = y(\xi, n) = u(\xi, n) - u(\xi, n-1).$$

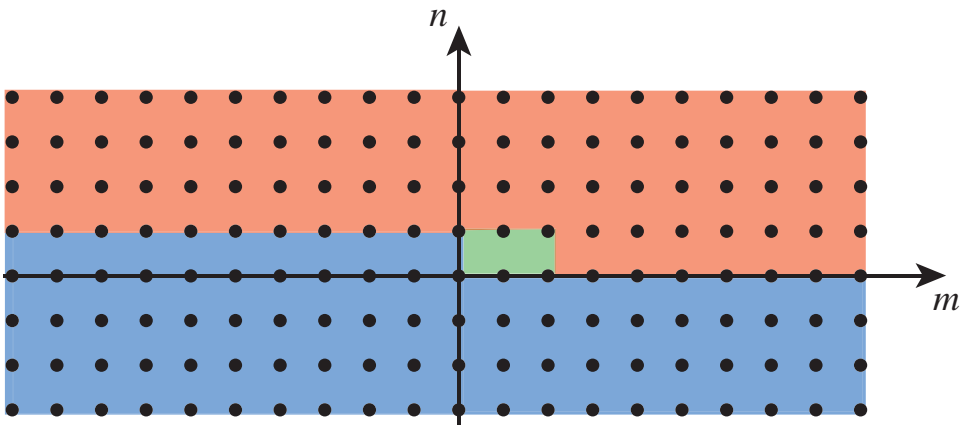

Figure 2.2: A twin boundary with a single step. Vertical bonds inside the blue region are in variant II, bonds in the red region are in variant I, and the strains of the vertical bonds inside the green region have spinodal values.

We assume that at infinity the vertical strain tends to constant values $y_+ < 0$ and $y_- > 0$ in variant I and variant II, respectively:

$$\begin{aligned} &y(\xi, n) \to y_\pm, \quad \text{as } n \to \pm\infty \\ &y(\xi, n) \to \begin{cases} y_+, & n \geq 2 \\ y_\pm, & n = 1 \\ y_-, & n \leq 0, \end{cases} \quad \text{as } \xi \to \pm\infty \end{aligned} \tag{2.5}$$

Furthermore, we assume the horizontal strains vanish at infinity:

$$e_{m,n}(t) = u_{m,n}(t) - u_{m-1,n}(t) \to 0, \quad \text{as} \quad m^2 + n^2 \to \infty.$$

Note that under these assumptions the 31-component of the shear stress tends to zero at infinity, and in view of (2.2), the applied shear stress $\sigma_{32} = \sigma$ is given by $\sigma = y_+ + 1 = y_- - 1$, so that

$$y_\pm = \sigma \mp 1. \tag{2.6}$$

Observe also that the displacement $u_{m,n}(t)$ is determined up to an additive constant which can be fixed by specifying displacement of a lattice point. As illustrated in Figure 2.2, we assume that the vertical bonds at $n \geq 2$ and $n \leq 0$ remain in their respective variants:

$$y(\xi, n) < -\delta/2, \quad n \geq 2 \quad \text{(variant I)}, \qquad y(\xi, n) > \delta/2, \quad n \leq 0 \quad \text{(variant II)}. \tag{2.7}$$

Meanwhile, the vertical bonds at $n = 1$ can switch from the first to second variant as the step propagates to the right by going through the spinodal region. Following the approach used in [9], we assume that $y(\xi, 1)$ takes values inside the spinodal region when $|\xi| < z$, for some $z > 0$ to be determined, and is in the corresponding variant outside this interval:

$$\begin{aligned} y(\xi,1) &< -\frac{\delta}{2}, \quad \xi > z \quad \text{(variant I)} \\ |y(\xi,1)| &< \frac{\delta}{2}, \quad |\xi| < z \quad \text{(spinodal region)} \\ y(\xi,1) &> \frac{\delta}{2}, \quad \xi < -z \quad \text{(variant II)}, \end{aligned} \tag{2.8}$$

and the switch between variant I (II) and the spinodal region takes place at $\xi = \pm z$:

$$y(z,1) = -\frac{\delta}{2}, \quad y(-z,1) = \frac{\delta}{2}. \tag{2.9}$$

Under the above assumptions we can write

$$\Phi'(y(\xi,1)) = y(\xi,1) + 1 - 2\int_{-z}^{z} \theta(s-\xi)h(s)ds, \tag{2.10}$$

where $\theta(s)$ is a unit step function: $\theta(s) = 1$ for $s > 0$, $\theta(s) = 0$ for $s < 0$. Here we have introduced an unknown shape function $h(s)$, which is zero outside the interval $[-z, z]$ and is normalized so that

$$\int_{-z}^{z} h(s)ds = 1 \tag{2.11}$$

Using (2.4), (2.10) and the assumed inequalities (2.7) and (2.8), we rewrite the equations of motion (2.1) as

$$\begin{aligned} V^2 \frac{\partial^2}{\partial \xi^2} u(\xi,n) =& \chi\left(u(\xi+1,n) + u(\xi-1,n) - 2u(\xi,n)\right) + u(\xi,n+1) + u(\xi,n-1) \\ & -2u(\xi,n) + 2\left[\delta_{n,0} + (\delta_{n,1} - \delta_{n,0})\int_{-z}^{z} h(s)\theta(s-\xi)ds\right] \end{aligned} \tag{2.12}$$

The solution of (2.12) can be represented as the sum of the solution of the static problem with a flat twin boundary along $n = 0$ at zero stress and a solution of the dynamic problem for a screw dislocation located at the step front and moving steadily under the applied stress. More precisely, we write

$$u(\xi, n) = u_n^F + w(\xi, n), \tag{2.13}$$

where

$$u_n^F = \begin{cases} 0, & n \geq 0 \\ 2n, & n \leq -1 \end{cases} \tag{2.14}$$

satisfies the static flat-boundary problem

$$u_{n+1}^F + u_{n-1}^F - 2u_n^F + 2\delta_{n,0} = 0, \tag{2.15}$$

and the screw dislocation solution is given, up to an additive constant, by [9]

$$w(\xi, n) = n(\sigma - 1) + \frac{1}{2\pi^2} \int_{-\infty}^{\infty} \frac{e^{-ik_\xi \xi} H(k_\xi) \mathcal{J}(k_\xi, n)}{i(k_\xi - i0)} dk_\xi. \tag{2.16}$$

Here $k_\xi - i0 = \lim_{\varepsilon \to 0+}(k_\xi - i\varepsilon)$, $H(k_\xi)$ is the Fourier transform of $h(\xi)$ and

$$\mathcal{J}(k_\xi, n) = \int_{-\pi}^{\pi} \frac{(1 - e^{i\kappa}) e^{-in\kappa}}{V^2 k_\xi^2 - 4(\chi \sin^2 \frac{k_\xi}{2} + \sin^2 \frac{\kappa}{2})} d\kappa \tag{2.17}$$

is defined for integer n. The integral in (2.17) can be explicitly calculated using the residue theorem, yielding (A.3) in the Appendix A. Using (2.13), (2.14), (2.16) and the convolution properties of the Fourier transform, we obtain the vertical strains in the lattice as

$$y(\xi, n) = \int_{-z}^{z} g_{|n-1|}(\xi - s) h(s) ds + \begin{cases} \sigma - 1, & n \geq 1 \\ \sigma + 1, & n \leq 0. \end{cases} \tag{2.18}$$

Here we defined

$$g_j(\xi) = \frac{1}{\pi} \int_{-\infty}^{\infty} \frac{e^{-ik_\xi \xi}}{i(k_\xi - i0)} \mathcal{S}(k_\xi, j) dk_\xi, \quad j = 0, 1, 2, \ldots, \tag{2.19}$$

where

$$\mathcal{S}(k_\xi, j) = \begin{cases} (\lambda - \sqrt{\lambda^2-1})^{-|j|}(\delta_{j,0} - \sqrt{\frac{\lambda-1}{\lambda+1}}), & \lambda < -1 \\ (\lambda \mp i\sqrt{1-\lambda^2})^{-|j|}(\delta_{j,0} \pm i\sqrt{\frac{1-\lambda}{1+\lambda}}), & |\lambda| < 1, \quad k_\xi \lessgtr 0 \\ (\lambda + \sqrt{\lambda^2-1})^{-|j|}(\delta_{j,0} - \sqrt{\frac{\lambda-1}{\lambda+1}}), & \lambda > 1 \end{cases} \tag{2.20}$$

and

$$\lambda(k_\xi) = 1 + 2\chi \sin^2 \frac{k_\xi}{2} - \frac{1}{2}V^2 k_\xi^2. \tag{2.21}$$

Observe now that on one hand, we have

$$\frac{\partial}{\partial \xi} y(\xi, 1) = -\int_{-z}^{z} q(\xi - s)h(s)ds, \tag{2.22}$$

where, by (2.18) and (2.19),

$$q(\xi) = -g_0'(\xi) = \frac{1}{\pi}\int_{-\infty}^{\infty} e^{-ik_\xi \xi}\mathcal{S}(k_\xi, 0)dk_\xi. \tag{2.23}$$

On the other hand, (2.2) and (2.10) imply that for $|\xi| < z$

$$y(\xi, 1) = \delta\left(\int_{\xi}^{z} h(s)ds - \frac{1}{2}\right),$$

and thus

$$\frac{\partial}{\partial \xi} y(\xi, 1) = -\delta h(\xi). \tag{2.24}$$

Together, (2.22) and (2.24) yield a Fredholm integral equation of the second kind [9]:

$$\int_{-z}^{z} q(\xi - s)h(s)ds = \delta h(\xi), \qquad |\xi| < z, \tag{2.25}$$

where the shape function $h(\xi)$ is an eigenfunction of the integral operator in the left hand side of (2.25) with kernel (2.23) associated with the eigenvalue δ. The problem thus reduces to solving the integral equation (2.25) for z and $h(\xi)$.

Once $h(\xi)$ and z are known, the vertical strains for the traveling wave solution can be computed from (2.18). Substituting (2.18) into the switch conditions (2.9) and subtracting the first condition from the second, we obtain $\int_{-z}^{z}(g_0(-z-s) - g_0(z-s))h(s)ds = \delta$, which is automatically satisfied, as can be verified by integrating (2.25) and recalling (2.11) and the

first equality in (2.23). Meanwhile, adding the two conditions yields the following expression for the applied stress:

$$\sigma = 1 - \frac{1}{2}\int_{-z}^{z} h(s)[g_0(z-s) + g_0(-z-s)]ds. \tag{2.26}$$

Since g_0 depends on V, this defined the *kinetic relation* $\sigma = \Sigma(V)$ between the applied stress σ and the step moving velocity V. The relation also depends on δ and χ.

We remark that the real wave numbers k_ξ such that $|\lambda(k_\xi)| \leq 1$, with λ given by (2.21), correspond to the *lattice waves* emitted by the moving step because this inequality implies the existence of real wave numbers κ such that the velocity of the moving step equals the horizontal component of the phase velocity of some plane waves: $V = \omega/k_\xi$, where $\omega^2 = 4(\chi \sin^2(k_\xi/2) + \sin^2(\kappa/2))$ is the dispersion relation [10]. One can show [9] that only these waves, which carry energy away from the step, contribute to the stress in (2.26). The transfer of energy from long (continuum level) to short (lattice-scale) waves associated with this nonlinearity-induced radiation is known in the physics literature as the radiative damping phenomenon (e.g. [43]). Analyzing the asymptotic strain behavior as in [9, 37, 59], one can show that the amplitude of the lattice waves slowly decays as $|\xi|$ increases, so that the strains tend to constant values at infinity, as assumed in (2.5).

It should be emphasized that the solutions of (2.12) satisfy the original nonlinear equation (2.1) if and only if the *admissibility conditions* (2.7) and (2.8) hold. Solutions of (2.12) that violate any of the admissibility conditions will be called *inadmissible*.

2.3 ADMISSIBLE SOLUTIONS AND KINETIC RELATIONS

We first review the limiting case $z = 0$ that reduces to the screw dislocation problem studied in [9, 11]. One can see that in this limit we must have $\delta = 0$, i.e. spinodal region degenerates to a single point and $\Phi'(y)$ becomes bilinear, while the shape function becomes a Dirac delta function: $h(s) = \delta_D(s)$. Thus, (2.18) reduces to

$$y^0(\xi, n) = u^0(\xi, n) - u^0(\xi, n-1) = g_{|n-1|}(\xi) + \begin{cases} \sigma - 1, & n \geq 1 \\ \\ \sigma + 1, & n \leq 0 \end{cases}, \tag{2.27}$$

where $u^0(\xi, n)$ satisfies

$$V^2 \frac{\partial^2}{\partial \xi^2} u^0(\xi, n) = \chi(u^0(\xi+1, n) + u^0(\xi-1, n) - 2u^0(\xi, n)) + u^0(\xi, n+1) + u^0(\xi, n-1) \\ -2u^0(\xi, n) + 2\left[\delta_{n,0} + (\delta_{n,1} - \delta_{n,0})\theta(-\xi)\right]. \tag{2.28}$$

We observe that the first equality in (2.23) and (2.27) imply that

$$q(\xi) = -\frac{\partial y^0(\xi, 1)}{\partial \xi}. \tag{2.29}$$

Note that the vertical strain $y^0(\xi, n)$ should also satisfy the corresponding admissibility conditions (2.7) and (2.8) at $z = 0$ and $\delta = 0$, which reduce to (with $y = y^0$)

$$y(\xi, n) < 0, \quad n \geq 2 \quad \text{(variant I)}, \qquad y(\xi, n) > 0, \quad n \leq 0 \quad \text{(variant II)}. \tag{2.30}$$

and

$$y(\xi, 1) < 0, \quad \xi > 0 \quad \text{(variant I)}, \qquad y(\xi, 1) > 0, \quad \xi < 0 \quad \text{(variant II)}, \tag{2.31}$$

respectively. The kinetic relation (2.26) can be shown in this case to yield $\sigma = \Sigma_0(V)$ defined by

$$\sigma = 1 - g_0(0) = \frac{2}{\pi} \int_0^\infty \frac{1}{k_\xi} \sqrt{\frac{1 - \lambda(k_\xi)}{1 + \lambda(k_\xi)}} \theta(1 - |\lambda(k_\xi)|) dk_\xi, \tag{2.32}$$

where we recall that $\lambda(k_\xi)$ is given by (2.21). The reader is referred to [10, 11, 37] for more details.

The resulting kinetic relation, shown in Figure 2.3(a), consists of disjoint segments separated by *resonance velocities*, i.e. values of V such that $\lambda(k_\xi) = -1$ and $\lambda'(k_\xi) = 0$ for some real k_ξ (see Figure 2.3(b)). At these velocities the kinetic relation has either a logarithmic singularity (at the resonance velocities that correspond to the local minima of $V(k_\xi)$ such that $\lambda = -1$) or a jump discontinuity (at the local maxima) [11]. A typical admissible solution ($V = 0.5$) above the first resonance $V_1 \approx 0.3158$ is shown in Figure 2.4(a). One can see that the moving step generates lattice waves behind it. As velocity decreases below the first resonance, solution develops oscillations at $\xi > 0$ as well; see, for example, the vertical

strain profile at $V = 0.17$ in Figure 2.4(b), where two modes of emitted lattice waves propagate behind and one mode ahead of the step. However, a closer inspection reveals that this solution is in fact *inadmissible* and should be removed because it violates the first inequality in both (2.30) and (2.31). At $\chi = 1$, our calculations show that the large-velocity segment contains admissible solutions above a certain threshold, $V \geq V_0 \approx 0.4649$, while in several segments of the kinetic relation below the threshold, we only found inadmissible traveling waves that violate (2.31) and sometimes also (2.30), and thus need to be removed. This suggests non-existence of traveling wave solutions with velocity lower than the threshold value in the $z = 0$ case, in agreement with the conjectures made in [10, 11]. Meanwhile, solutions at sufficiently high velocities ($V \geq V_h \approx 0.9908$ at $\chi = 1$) are also inadmissible, because the large amplitude of waves propagating behind the step front causes the $n = 2$ bonds directly above the step to switch from variant I to variant II, which violates the first inequality in (2.30) (see also [37]).

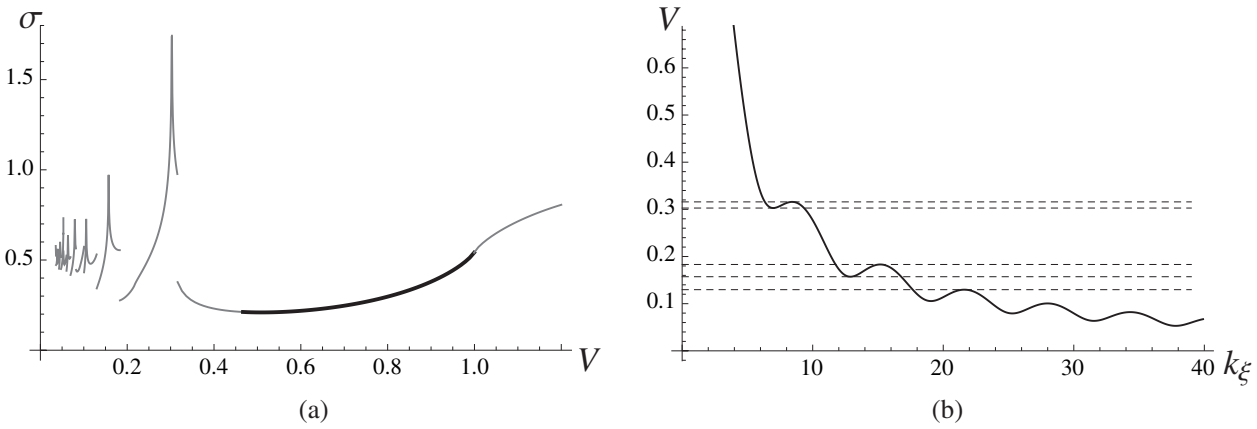

Figure 2.3: (a) Kinetic relation $\sigma = \Sigma_0(V)$ at $z = 0$, $\delta = 0$. Only the first twenty segments are shown. Admissible solutions correspond to the dark portion of the first segment. (b) Velocities V such that $\lambda = -1$ for positive real k_ξ. The dashed lines indicate the first five resonance velocities at which $\lambda(k_\xi) = -1$ and $\lambda'(k_\xi) = 0$. Here $\chi = 1$.

Consider now the trilinear problem with $\delta > 0$. To find $h(s)$ and z for given non-resonant $V > 0$ and $\delta > 0$, we approximate the integral equation (2.25) by a trapezoidal rule with a uniform mesh, obtaining a homogeneous linear system $(\mathbf{Q}(z) - \delta\mathbf{I})\mathbf{h} = \mathbf{0}$, where $\mathbf{Q}(z)$ is the matrix approximating the integral operator, $\mathbf{I}$ is the identity matrix, and $\mathbf{h}$ is the vector approximating the unknown shape function. To find z, we solve the nonlinear algebraic

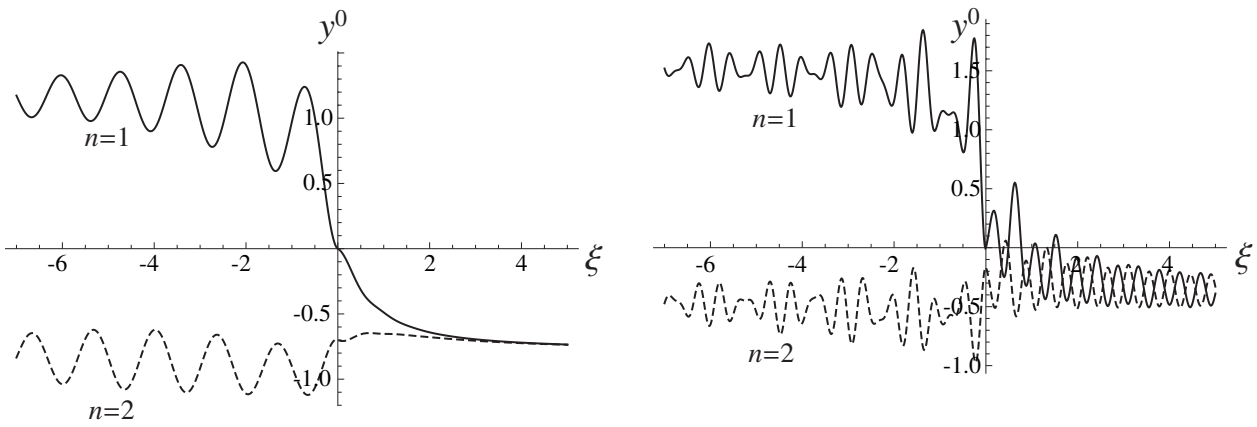

(a) V=0.5 (b) V=0.17

Figure 2.4: Vertical strain $y^0(\xi, n)$ profiles at $n = 1$, 2 formally computed from (2.27) and (2.32) at $z = 0$, $\delta = 0$, $\chi = 1$ and velocities (a) $V = 0.5$ ($\sigma = 0.2096$) and (b) $V = 0.17$ ($\sigma = 0.5736$). Solution in (a) satisfies the constraints (2.30) and (2.31) but the one in (b) violates both constraints at $\xi > 0$. Here and in the pictures below $n = 0$ strains are not shown because by the symmetry of $g_{|n-1|}(\xi)$ and (2.18), $y(\xi, 0) = y(\xi, 2) + 2$.

equation $\det(\mathbf{Q}(z) - \delta\mathbf{I}) = 0$, which ensures that δ is an eigenvalue of $\mathbf{Q}(z)$, and then find the corresponding eigenvector $\mathbf{h}$, normalized by (2.11). In general, there may be more than one value of z but our calculations suggest that at most one value yields admissible solutions. Once z and $\mathbf{h}$ are found, the trapezoidal approximation of the integrals in (2.18) and (2.26) is used to compute the solution $y(\xi, n)$ and the applied stress σ.

The resulting vertical strains of $n = 1$ and $n = 2$ bonds at $V = 0.17$ are shown by Figure 2.5 for $\delta = 0.8$ (which yields $z = 0.424$ and $\sigma = 0.0409$) and $\delta = 1.2$ ($z = 0.875$ and $\sigma = 0.0039$). As in [9], we observe that the main effect of increasing δ, which leads to larger z, is the decreased amplitude of the oscillations due to wave modulation that takes place over the larger time interval. As a result, the solutions at $V = 0.17$ become admissible at $\delta = 0.8$ and $\delta = 1.2$, while the corresponding solution of the bilinear problem at $z = 0$ is not. Note also that the stress decreases as δ is increased due to the smaller contribution of the lattice waves, although it may oscillate at larger values of δ [51, 52].

Figure 2.6 shows the half-width z of the transition region as a function of V for different δ at $\chi = 1$, and the corresponding kinetic relations are shown in Figure 2.7. Due to the pile-

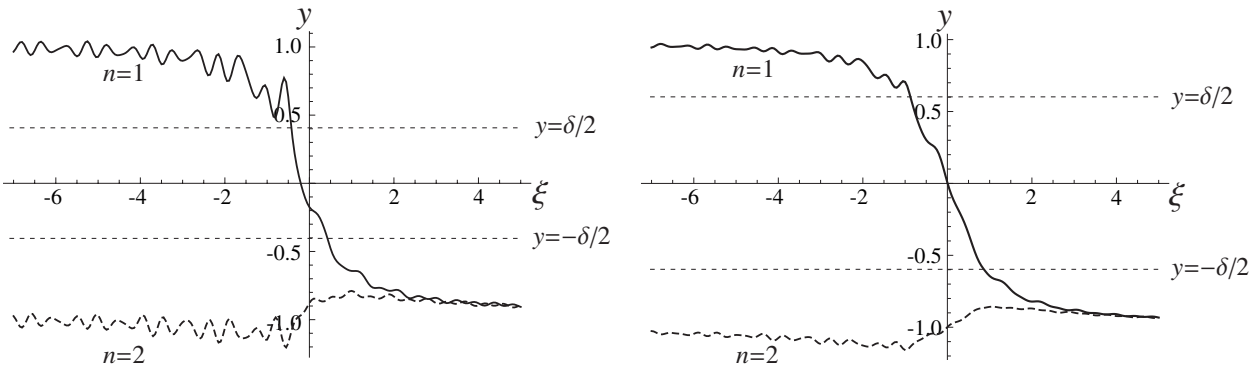

(a) δ=0.8 (b) δ=1.2

Figure 2.5: Vertical strain $y(\xi, n)$ ($n = 1, 2$) profiles at $V = 0.17$, with (a) $\delta = 0.8$ ($z = 0.424$, $\sigma = 0.0409$) and (b) $\delta = 1.2$ ($z = 0.875$, $\sigma = 0.0039$). Both solutions are admissible. Here $\chi = 1$.

up of resonance velocities as V approaches zero, which makes the computation progressively more difficult, only $V \geq 0.1$ were considered. A detailed inspection suggests that all solutions shown except the ones along the grey portions of the curves are admissible. This includes solutions in the immediate vicinity of the resonance velocities, which correspond to the cusps in Figure 2.6 and Figure 2.7. Note that the kinetic relations are highly non-monotone, with larger stress variations at lower δ. Observe also that at $\delta = 1.2$ the low-velocity motion requires very little applied stress, due to the small amplitude of the emitted waves and thus small amount of radiative damping. This "solitonlike" dislocation behavior is discussed in [51, 52].

Interestingly, as in [49], our numerical calculations reveal that as δ approaches zero at velocities below the threshold value $V_0 \approx 0.4649$, the value of z approaches a positive value rather than zero, contrary to the assumption of $z = 0$ in [10, 11] for the bilinear case. This motivates us to construct a new type of traveling wave solutions for the limiting case $\delta = 0$ that has $z > 0$ below the threshold value. We postpone the discussion of these new solutions until Section 2.4, while here we simply show the corresponding curves for comparison.

We now consider the dependence of the kinetic relation $\sigma = \Sigma(V)$ on χ, the dimensionless anisotropy parameter measuring the shear strength of the linearly elastic horizontal bonds relative to the vertical ones. Let $c = \sqrt{\chi}$ be the sound speed of elastic shear waves in the

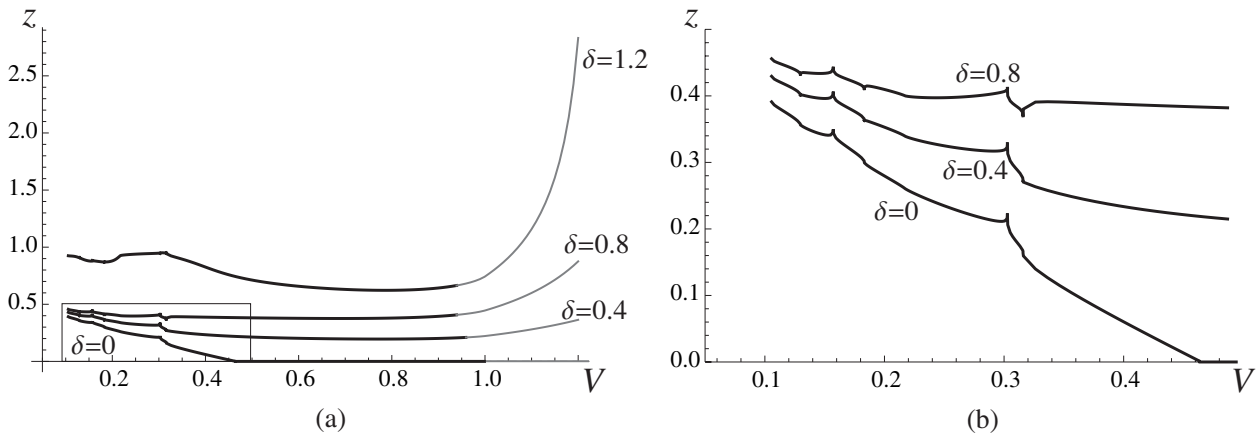

Figure 2.6: (a) The half-width $z(V)$ of the transition region for different δ calculated for $V \geq 0.1$. (b) Zoom-in of the small-velocity region inside the rectangle. Here $\chi = 1$. The thicker black segments contain admissible solutions, while the gray segments correspond to inadmissible solutions.

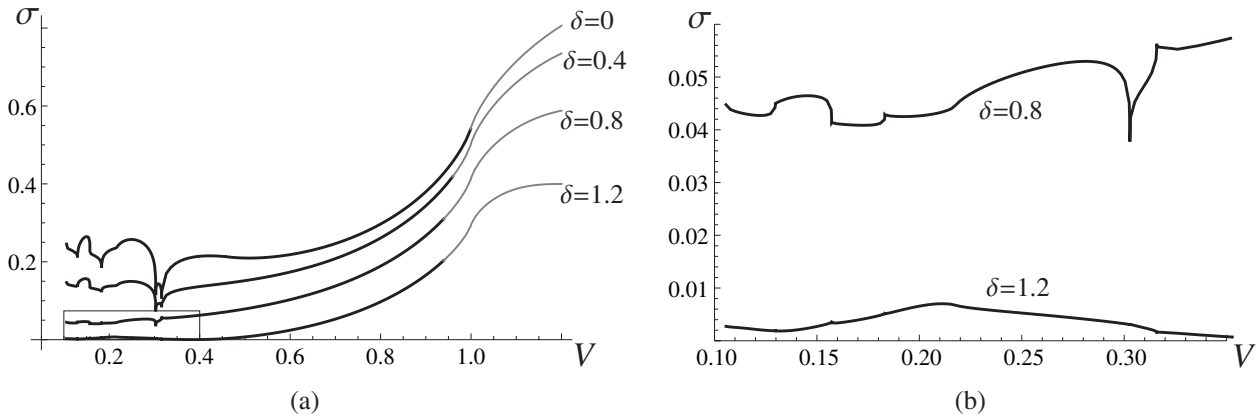

Figure 2.7: (a) Kinetic relations $\sigma = \Sigma(V)$ for different δ and $V \geq 0.1$. (b) Zoom-in of the small-velocity region inside the rectangle. Here $\chi = 1$. The thicker black segments contain admissible solutions, while the gray segments correspond to inadmissible solutions.

horizontal direction of the step motion. At $\delta = 0.8$, typical kinetic relations at different χ are shown in Figure 2.8(b), and the corresponding $z(V)$ graphs in Figure 2.8(a). Note that the resonance velocities take different values for different χ, so the locations of the cusps in the kinetic relation changes. One can see that a higher χ results in a lower applied stress at the same normalized velocity V/c because it means a stronger coupling of the vertical bonds.

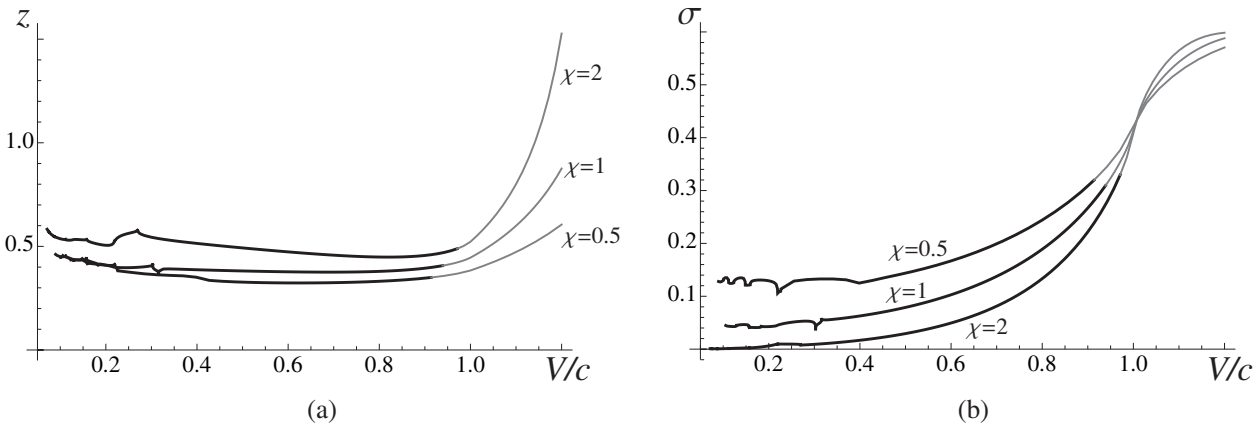

Figure 2.8: (a) The half-width $z(V)$ of the transition region and (b) kinetic relations $\sigma = \Sigma(V)$ at different χ. The thicker black segments contain admissible solutions, while the gray segments corresponding to inadmissible solutions. Here $\delta = 0.8$, and the velocities are normalized by $c = \sqrt{\chi}$.

At sufficiently large velocities above a threshold V_h (for example, $V > V_h \approx 0.9389$ at $\delta = 0.8$ and $\chi = 1$), the amplitude of the waves propagating behind the step front becomes so large that strain in some $n \geq 2$ bonds above the step enters the spinodal region from variant I, violating the first constraint in (2.7) and thus rendering the corresponding solutions inadmissible (see the gray large-velocity segments in Figures 2.6(a), 2.7(a) and 2.8). One can observe that at $\chi = 1$ the upper threshold V_h increases as δ decreases. Meanwhile, at the same $\delta = 0.8$, the normalized upper threshold V_h/c increases as χ is increased. As we will see in Section 2.5, this solution failure at $\sigma > \sigma_h = \Sigma(V_h)$ corresponds to a cascade nucleation of new steps.

In addition to the traveling wave solutions, there are equilibrium states ($V = 0$) that exist when the applied stress is in the *trapping region* $|\sigma| \leq \sigma_P$, where σ_P is the Peierls stress (B.9). One can show [60] that at $0 < \delta < 2$ there are two equilibrium states with

the assumed single-step configuration for $|\sigma| < \sigma_P$, a stable state with m_s spinodal vertical bonds near the step front and an unstable state with $m_s + 1$ spinodal bonds, where m_s and σ_P determined by δ and χ (see Appendix B for more details). These solutions are given by (B.4) for $m_s = 0$ and (B.7), (B.8) for $m_s \geq 1$.

2.4 NEW TRAVELING WAVE SOLUTIONS

We now revisit the bilinear problem ($\delta = 0$) with degenerate spinodal region, where, as we recall, no admissible solutions were found for $V < V_0$ at $z = 0$. However, as we already mentioned above, our results for small δ in this velocity region suggest that z tends to a *nonzero* value as δ approaches zero. This suggests that following the approach recently pursued for the one-dimensional problem [53], we should seek solutions with $z > 0$ and replace the admissibility conditions (2.31) by the more general conditions

$$\begin{aligned} &y(\xi, 1) < 0, \quad \xi > z \quad \text{(variant I)}, \\ &y(\xi, 1) = 0, \quad |\xi| \leq z \quad \text{(degenerate spinodal region)}, \\ &y(\xi, 1) > 0, \quad \xi < -z \quad \text{(variant II)}, \end{aligned} \tag{2.33}$$

while leaving (2.30) (or, equivalently, (2.7) at $\delta = 0$) the same. Note that (2.9) at $\delta = 0$ is included in (2.33), so we seek solutions of (2.12) subject to (2.30) and (2.33).

Observe now that (2.22) still holds. At the same time, our assumption that $y(\xi, 1) \equiv 0$ at $|\xi| \leq z$ implies $\frac{\partial}{\partial \xi} y(\xi, 1) \equiv 0$ in the interval $(-z, z)$. Together with (2.22), this yields a Fredholm integral equation of the first kind:

$$\int_{-z}^{z} h(s) q(\xi - s) ds = 0 \quad |\xi| < z. \tag{2.34}$$

Thus the shape function $h(s)$ is an eigenfunction of the integral operator in the left hand side of (2.34) with kernel (2.23) associated with the zero eigenvalue. As before, we solve this problem numerically using the trapezoidal approximation, which now involves finding the roots of $\det \mathbf{Q}(z) = 0$, and find that at most one of these roots yields admissible solutions that satisfy (2.30) and (2.33). For example, Figure 2.9 shows $y(\xi, 1)$ and $y(\xi, 2)$ obtained

at $V = 0.17$, which yields $z = 0.322$. One can see that unlike the $z = 0$ solution (the gray curves), which is inadmissible since it violates (2.30) and (2.31), the new solution (black curves) satisfies the more general admissibility condition (2.33) within the numerical error. We verified that it also satisfies (2.30) and thus is admissible. Note that like its counterparts at $\delta > 0$ at the same velocity, it involves lattice waves propagating both behind and ahead of the step.

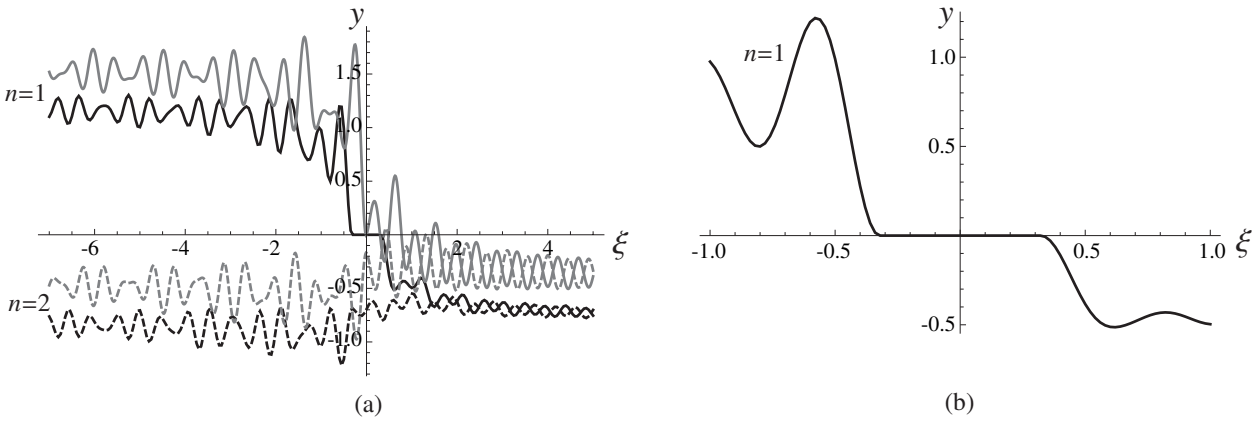

Figure 2.9: (a) New traveling wave solution $y(\xi, n)$ at $n = 1$, 2 and $V = 0.17$ with $z = 0.322$ (black curves), shown together with the inadmissible $z = 0$ solution $y^0(\xi, n)$ (gray curves). (b) Zoom-in of the $z = 0.322$ solution at $n = 1$. Here $\delta = 0$, $\chi = 1$ and $\sigma = 0.2139$ for the new solution.

Repeating this procedure for a range of velocities, we obtain the relation $z(V)$ between z and V at $\chi = 1$ shown in Figure 2.6. Note that $z(V)$ tends to zero as the velocity approaches the value $V = V_0 \approx 0.4649$. Recall that this is the threshold above which (and below $V_h \approx 0.9908$) $z = 0$ solutions of the bilinear problem become admissible. This suggests that as in [53], the new solutions with $z > 0$ bifurcate from $z = 0$ solutions at V_0. To see this, we follow the argument in [53] and consider the piecewise linear approximation of the kernel (2.23) in (2.34), as in [9]. Note that $q(\xi)$ is continuous, while $q'(\xi)$ has a jump discontinuity at $\xi = 0$, as can be shown from (2.29) and (2.28). Thus for small ξ the kernel can be approximated by

$$\hat{q}(\xi) = \begin{cases} q_0 + q_+\xi, & \xi > 0 \\ q_0 + q_-\xi, & \xi < 0, \end{cases} \tag{2.35}$$

where

$$q_0 = q(0), \quad q_\pm = q'(0\pm), \quad q_+ - q_- = 4/V^2, \tag{2.36}$$

with the last relation is implied by (2.28) and (2.29). Solving the approximate version of (2.34), i.e. $\int_{-z}^{z} h(s)\hat{q}(\xi - s)ds = 0$, $|\xi| < z$, one obtains [53]

$$z = \frac{q_0(q_+ - q_-)}{2q_+q_-} \tag{2.37}$$

and

$$h(\xi) = \frac{q_-}{q_- - q_+}\delta_D(\xi + z) - \frac{q_+}{q_- - q_+}\delta_D(\xi - z), \tag{2.38}$$

in the sense of distributions. Numerical evaluation of (2.23) and the last of (2.36) show that $(q_+ - q_-)/(2q_+q_-) < 0$ when V is near the threshold V_0. Thus the positive solution z given by (2.37) exists provided that $-q_0 = \frac{\partial}{\partial\xi}y^0(0,1) > 0$. Meanwhile, the admissibility conditions (2.31) imply that $\frac{\partial}{\partial\xi}y^0(0,1) \leq 0$. This indicates that bifurcation of the new type of traveling wave with $z > 0$ occurs precisely at the threshold velocity V_0, at which $q_0(V_0) = 0$, and below which the $z = 0$ solutions are inadmissible because (2.31) is violated. As shown in Figure 2.10, the values of $z(V)$ obtained from the numerical solution of (2.34) with the original kernel (2.23) near the threshold velocity V_0 approach the values (2.37) resulting from the linear approximation near the threshold velocity.

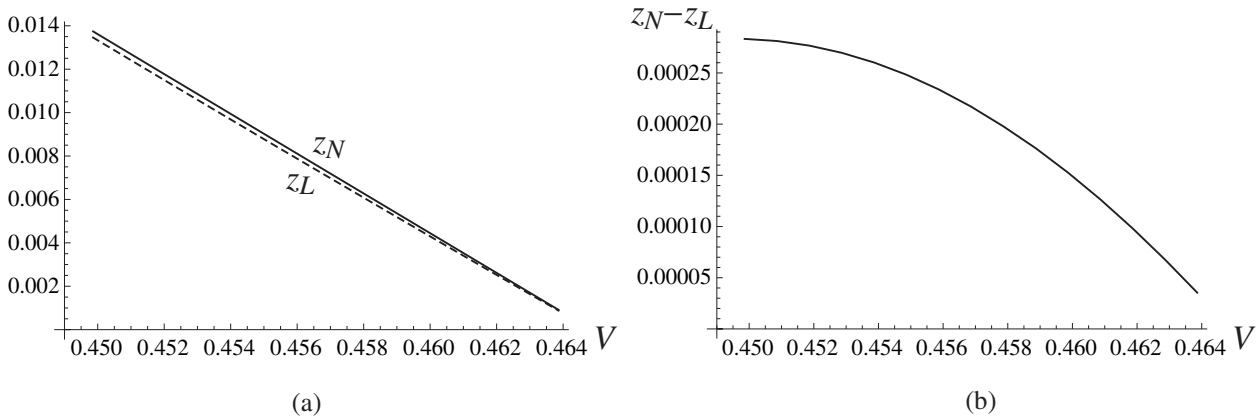

Figure 2.10: Comparison of the function $z_N(V)$ computed numerically using the kernel (2.23) (solid line) and $z_L(V)$ obtained from (2.37) using the linear approximation (2.35) of the kernel (dashed line) near the bifurcation point $V_0 \approx 0.4649$.

The corresponding kinetic relation $\sigma = \Sigma(V)$ is shown in Figure 2.7. It coincides with the $z = 0$ relation $\Sigma_0(V)$ above the velocity V_0, while below this threshold, where $z > 0$, it provides lower values of the applied stress and replaces the singularities in $\Sigma_0(V)$ at the

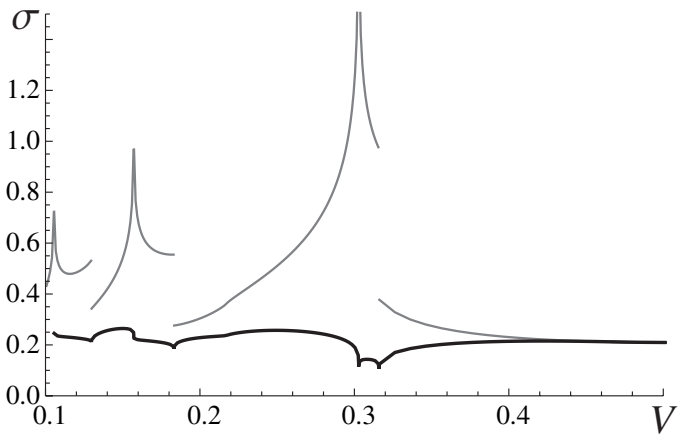

Figure 2.11: Comparision of the kinetic relation $\sigma = \Sigma(V)$ generated by the new solutions with $z > 0$ with the relation $\Sigma_0(V)$ obtained from the formal $z = 0$ solutions of the bilinear ($\delta = 0$) problem. The two curves coincide above the threshold velocity $V_0 \approx 0.4649$. The gray curves correspond to *inadmissible* $z = 0$ solutions below V_0.

resonance velocities by cusps; see Figure 2.11 for comparison. This result thus extends the kinetic relation obtained in [10, 11] for $\delta = 0$ case into the region of velocities $V < V_0$, where the new solutions with $z > 0$ "fill the gap" left by the non-existence of admissible solutions with $z = 0$.

2.5 STABILITY OF THE TRAVELING WAVES: NUMERICAL SIMULATIONS

To investigate stability of the obtained traveling waves solutions and obtain an independent verification of our results, we solve the equations (2.1) numerically without assuming any particular motion pattern and then compare the numerical results with the traveling wave solutions. We use the velocity Verlet algorithm in the computational domain Ω given by a truncated 400×8 lattice. The initial configuration has a flat twin boundary with a single step in the center of the domain, as in Figure 2.2. To avoid reflection of lattice waves from the boundary of Ω, we use the non-reflective boundary conditions (NRBC) developed

in [38]. Assuming that the initial condition *outside* the computational domain satisfies the equilibrium equations with zero initial velocity and that the problem there remains linear (i.e. the vertical bonds remain in their respective variants), the NRBC conditions prescribe the displacement on $\partial\Omega^+$, a set of lattice points outside the computational domain Ω that have at least one nearest neighbor belonging to $\partial\Omega$, the boundary of Ω.

To construct the initial condition for given δ and applied stress below the Peierls threshold, $0 < \sigma < \sigma_P$, we start with an equilibrium state (stable or unstable), given by (B.4) if there are no spinodal bonds and (B.7), (B.8) if there is at least one such bond. To trigger step propagation, we perturb this state by changing the vertical strain in front of the step. Above the Peierls threshold, no equilibrium state exists but we use the same formulas to ensure that the initial state satisfies the equilibrium equations outside Ω, as required by the NRBC conditions we use. Inside the computational domain, this yields a non-equilibrium displacement. If it does not satisfy the assumed initial phase distribution, we modify the initial displacement in Ω by prescribing strains in some vertical bonds and solving a constrained equilibrium problem that ensures the assumed inequalities hold. Initial velocities are set to zero.

We find that for sufficiently small σ below the Peierls threshold the numerical solution gets trapped in a stable equilibrium state. For higher applied stress, the step propagates, and after some transient time its motion becomes steady, which means that the time period during which the front moved from one vertical bond in the lattice to the next approaches a constant value T. The velocity is then obtained by computing $V = 1/T$ as the average over the last ten periods.

Figures 2.12 and 2.13 compare (V, σ) obtained from the numerical results (circles) for $\delta = 1.2$ and $\delta = 0.8$ (at $\chi = 1$) with the corresponding semi-analytical kinetic relation curves. One can see that the numerical results are in very good agreement with some increasing portions of the kinetic curves, which suggests stability of the traveling wave solutions with the corresponding velocities. The fact that the numerical results only fall on the increasing portions of the curves supports the conjecture in [49] that $\Sigma'(V) > 0$ is necessary but not sufficient for stability. Note, in particular, that the results indicate stability of an entire range of low-velocity motion ($0.139 \leq V \leq 0.21$) at $\delta = 1.2$ at very small values of the

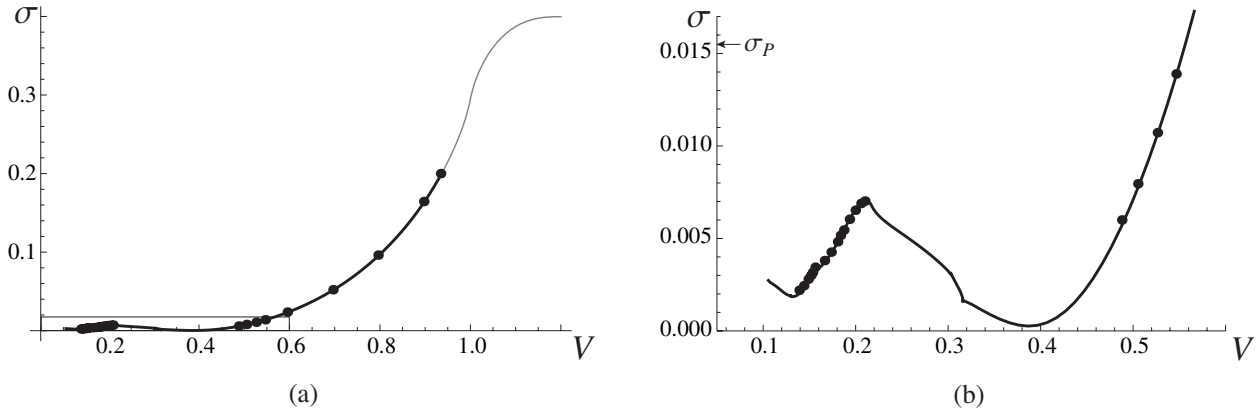

Figure 2.12: (a) Results of the numerical simulations for $\delta = 1.2$ (circles), shown together with the kinetic curve. (b) Zoom-in of the small-velocity region inside the rectangle in (a).

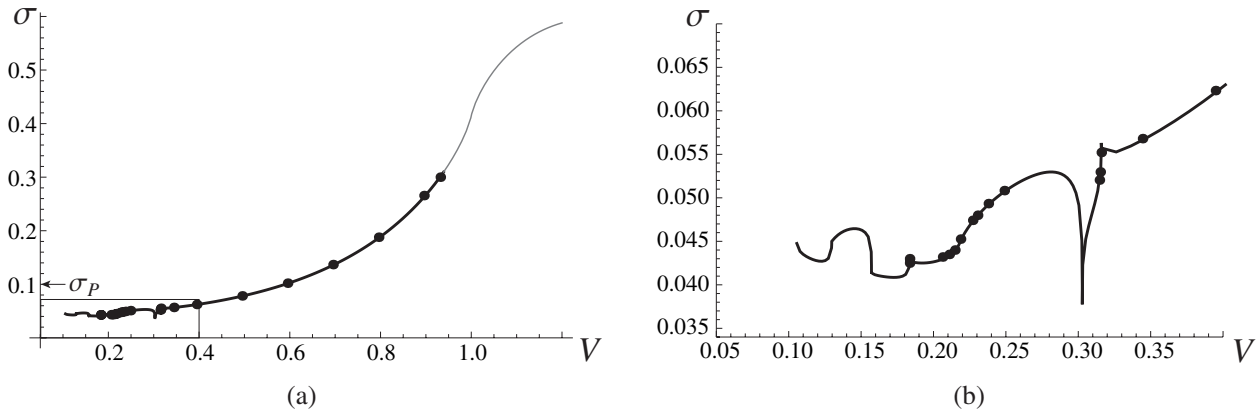

Figure 2.13: (a) Results of the numerical simulations for $\delta = 0.8$ (circles), shown together with the kinetic curve. (b) Zoom-in of the small-velocity region inside the rectangle in (a) (below the Peierls stress).

applied stress where the solutions coexist with stable equilibrium states. Observe also that stable solutions with different velocities may coexist at the same value of σ. For example, at $\delta = 1.2$, numerical simulations at $\sigma = 0.006$ yield steady motion at either $V = 0.193$ or $V = 0.488$, depending on the perturbation introduced in the initial conditions. Low-velocity solutions appear to be stable only when δ is sufficiently high. Meanwhile, at small δ our results indicate stability of only relatively fast traveling waves. In particular, we did not find any numerical evidence that the new traveling wave solutions constructed in Section 2.4 for $\delta = 0$ are stable.

As discussed in Section 2.3, when the applied stress is above a certain critical value $\sigma_h = \Sigma(V_h)$, which depends on δ and χ, the traveling wave solutions become inadmissible because the large-amplitude lattice waves emitted by the moving step force some vertical bonds above the step ($n \geq 2$) to have strain values outside variant I and hence violate the first inequality in (2.7). Our numerical simulations reveal that at the applied stress $\sigma > \sigma_h$, nucleation of new islands of variant II takes place on top of the existing step configuration. For example, at $\delta = 0.8$ and $\chi = 1$ we have $\sigma_h \approx 0.309$, and at $\sigma = 0.45$ above this threshold, after some transient time, an initial single step propagates steadily with velocity $V \approx 1.01$. This can be seen in Figure 2.14(a), which shows the evolution in time of the step front positions $x_n(t)$, defined by $x_n(t) = m$, where m is such that $y_{m,n}(t) > \delta/2$ and $y_{m+1,n}(t) \leq \delta/2$ for the initial step, $n = 1$. Eventually, however, a vertical bond above the step enters the spinodal region, nucleating a new island that starts propagating on top of the initial step. For example, at $t = 12$ in Figure 2.15 one can see six vertical bonds that have strains in either spinodal region (green) or variant II (blue). As this island grows, its boundaries soon attain the same velocity as the initial step, as can be seen in Figure 2.14(a) ($n = 2$). Later on, more islands nucleate, grow and coalesce, and all the fronts eventually propagate with the same velocity; see Figure 2.14(a) and Figure 2.15. At higher applied stress, $\sigma = 0.55$, island nucleation occurs sooner, and new islands nucleate and merge more frequently (see Figure 2.14(b)). While these observations are similar to the results obtained in [38] for a potential with a degenerate spinodal region, the new feature here is that island nucleation no longer occurs instanteneously but requires some time to develop. For example, the right island at $n = 3$ in Figure 2.15 starts forming already around $t = 29$, where one

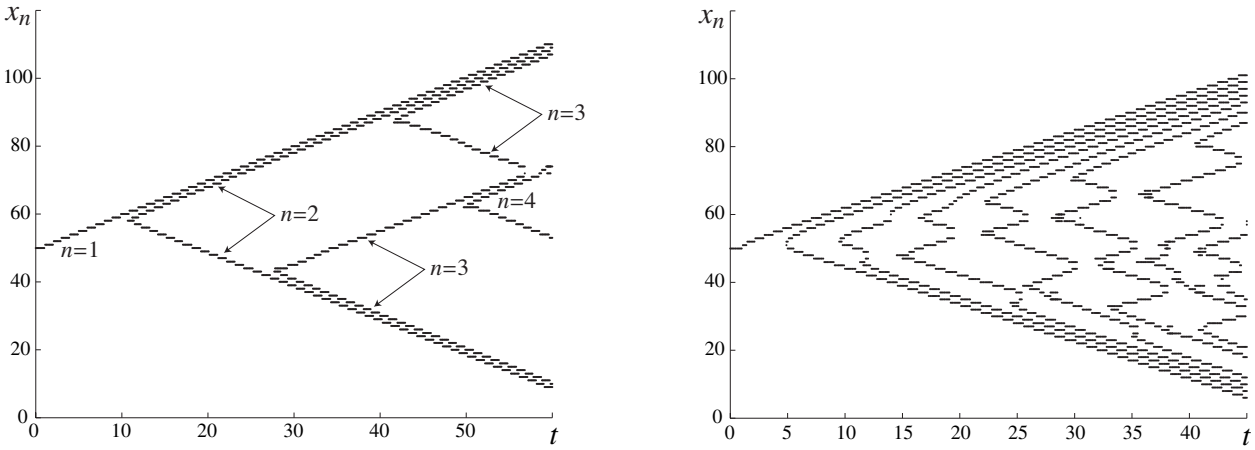

(a) σ=0.45 (b) σ=0.55

Figure 2.14: Evolution of step front positions $x_n(t)$ during island nucleation, propagation and coalescence at different values of the applied stress above the threshold value σ_h. Here $\delta = 0.8$ and $\chi = 1$.

can see a bond inside the spinodal region, but it does not fully develop and start growing until a much later time, as can be seen from $t = 42$ snapshot, where the island has only grown by a few bonds (see also Figure 2.14(a)). The cascade island nucleation observed here is in agreement with the dynamic twin nucleation and growth due to lattice waves emitted by a sufficiently fast motion of a screw dislocation that was predicted in [54] and studied numerically in [55] and [56].

2.6 CONCLUDING REMARKS

In this chapter, we used a simple antiplane shear lattice model with piecewise linear interactions to study the motion of a step propagating along a twin boundary. Following the approach developed in [9], we constructed semi-analytical traveling wave solutions for a wide range of the velocities and showed that the width of the spinodal region and the material anisotropy have a significant effect on the resulting kinetic relation between the applied stress and the velocity of the step. Our results extend and complement the work

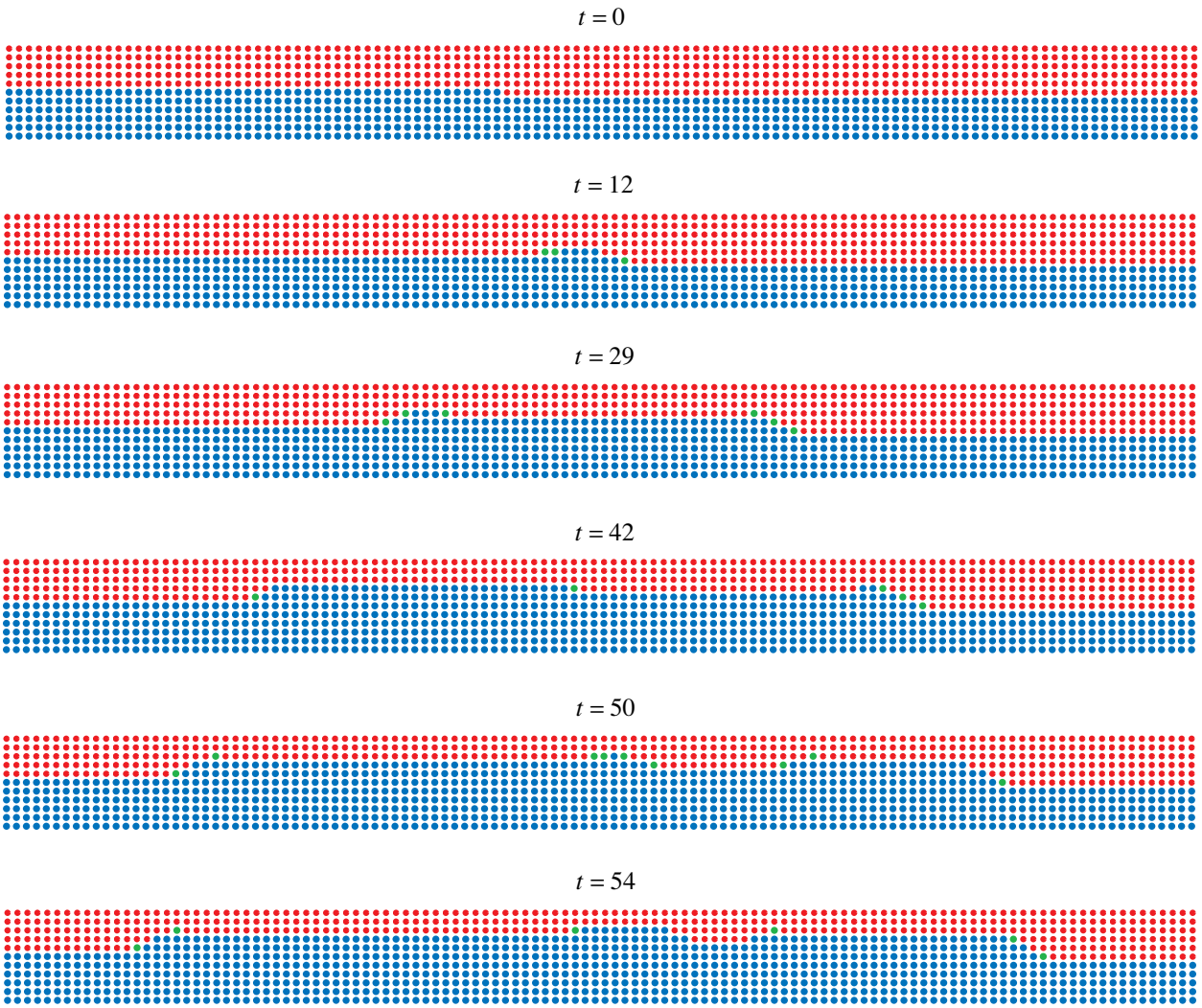

Figure 2.15: Time snapshots of island nucleation and growth at $\sigma = 0.45$, $\delta = 0.8$ and $\chi = 1$. The corresponding evolution of step fronts is shown in Figure 2.14(a). Here the blue points represent vertical bonds that have strain in variant II, the red ones are in variant I, and the green ones are in the spinodal region.

in [9, 51, 52] by considering slow step propagation that was not previously investigated. Our semi-analytical results and numerical simulations strongly suggest that such motion does not only exist but may become stable if the spinodal region is sufficiently wide. The slow step motion requires very small applied stress and involves emitted lattice wave that may propagate both behind and ahead of the moving step. This is in contrast to the previously studied high-velocity motion that features waves only behind the step and requires a larger stress. We also numerically investigated the solution breakdown when the applied stress is above a certain critical value. In this case the lattice waves emitted by the moving step and propagating behind it enter the spinodal region and lead to a cascade nucleation, growth and coalescence of multiple islands on top of the moving step. Compared to the similar results in [38], where the spinodal region was degenerate, in our case the island nucleation does not happen instantaneously.

The solution procedure was also used to find new admissible traveling wave solutions at low velocities in the case when the spinodal region degenerates to a single point. Applying the method in [53], we showed that these new solutions, in which the transforming bonds stay at the spinodal value before switching to the new twin variant, bifurcate from the solutions where the transition is instantaneous precisely at the threshold velocity where the latter become inadmissible. This allowed us to extend the kinetic relation in [10, 11] to lower velocities, where no admissible solutions were previously found.

We remark that the kinetic relations obtained here are in general quantitatively different from the ones obtained in [49, 53] for the closely related one-dimensional Frenkel-Kontorova model due to the different kernel (2.23) in the integral equation (2.25). In particular, the amplitude of the oscillations in our kernel decays at infinity [37], while in the one-dimensional case it remains constant. Note also that the one-dimensional problem has stronger singularities at the resonance velocities in the $z = 0$ case [11]. Nevertheless, qualitatively many of the results are similar, suggesting that the one-dimensional model, which is technically much less involved, captures the basic features of the kinetics of a single step. One important exception is the solution breakdown at high velocities in the present model, which is an essentially higher-dimensional phenomenon, since it involves step nucleation at $n \geq 2$.

The work in this chapter can be extended to the case of multiple steps as in [37, 38] and

to other lattice geometries. The ultimate challenge is the multiscale problem of obtaining the kinetic relation for a twin boundary from the step kinetics that takes into account the interaction between the steps.

3.0 NONLINEAR WAVES IN A STRONGLY NONLINEAR LOCALLY RESONANT CHAIN

In this chapter, we explore nonlinear waves in locally resonant granular crystals in the absence of precompression. In this case, the dynamics of the system is strongly nonlinear and governed by (1.2) with $\delta_0 = 0$. As mentioned in Section 1.2, in the limit when the mass ratio ρ tends to infinity and the initial conditions for the secondary masses are zero, the system approaches the Newton's cradle model, a granular chain with onsite harmonic potential. This problem was studied in [20] (see also [21]), where the discrete p-Schrödinger (DpS) modulation equation governing slowly varying small amplitude of oscillations was derived and used to prove existence of time-periodic traveling wave solutions. The DpS equation was also used to compute and study these and other periodic solutions, such as standing and traveling bright breathers. The other limiting case, when $\rho = 0$, corresponds to the non-resonant homogeneous Hertzian chain problem, which is well known to have solitary wave solutions [12–14] but admits no bright breathers [21].

To investigate the case of finite mass ratio (i.e., away from the above studied limits), we follow the approach in [20] and derive generalized modulation equations of the DpS type. We show that these equations capture small-amplitude periodic traveling waves of the system quite well when the mass ratio is below a critical value. When the mass ratio ρ is large enough and the secondary masses satisfy zero initial conditions, these equations degenerate to the original DpS equation obtained in [20]. Using the technique established in [61], we prove that for suitable small-amplitude initial conditions and large enough ρ, solutions are well described by the limiting DpS equation over a long but finite time. We further show that when the mass ratio is large enough, the system admits *long-lived* bright breathers, spatially localized solutions of the system that remain close to a time-periodic oscillation over a long

time. However, we also prove that at finite ρ the problem has only trivial exact bright breather solutions, which do not involve Hertzian interactions between the primary masses. As in $\rho = 0$ case [21], this is mainly due to non-attracting character of such interactions.

To further explore the dynamics of the system at finite ρ, we use solutions of the generalized DpS equations to form initial conditions for the numerical computation of dark breather solutions, which come in two families of *site-centered* and *bond-centered* type. We then examine stability and bifurcation structure of both types of dark breathers at different mass ratios. When the breather frequency is above but sufficiently close to the linear frequency of the resonator, the dark breather solutions of site-centered type are long-lived and exhibit marginal oscillatory instability, while the bond-centered solutions exhibit real instability. This can lead to the emergence of steadily traveling dark breathers in the numerical simulations. In addition, we identify period-doubling bifurcations for the bond-centered solutions. The instability of breather solutions is also affected by the mass ratio. In particular, the real instability of the bond-centered breather solutions at a given frequency gradually becomes stronger as the mass ratio increases.

The chapter is organized as follows. Sec. 3.1 introduces the model, and the generalized DpS equations are derived in Sec. 3.2.1. In Sec. 3.2.2 we show that for sufficiently large mass ratio the equations reduce to the DpS equation derived in [20] and rigorously justify the validity of this equation on the long-time scale for suitable small-amplitude initial data. We use the modulation equations in Sec. 3.3 to numerically investigate small-amplitude time-periodic traveling waves, including their stability, the accuracy of their DpS approximation and the effect of the mass ratio. In Sec. 3.4 we show that the system admits only trivial exact bright breather solutions that do not involve Hertzian interactions. We then prove and numerically demonstrate the existence of long-lived nontrivial bright breathers at sufficiently large mass ratio. In Sec. 3.5.1 we construct the approximate dark breather solutions using the DpS equations. We use these solutions and a continuation procedure based on Newton-type method to compute numerically exact dark breathers in Sec. 3.5.2 and examine their stability and bifurcation structure in Sec. 3.6. Concluding remarks can be found in Sec. 3.7.

3.1 THE MODEL

Consider a chain of identical particles of mass m_1 and suppose a secondary particle of mass m_2 is attached to each primary one via a linear spring of stiffness $K > 0$ and constrained to move in the horizontal direction. As mentioned in Sec. 1.2, the harmonic oscillator is meant to represent the primary vibration mode of a ring resonator attached to each primary mass or a cylindrical rod. Let $\tilde{u}_n(\tilde{t})$ and $\tilde{v}_n(\tilde{t})$ denote the displacements of the nth primary and secondary masses, respectively. The dynamics of the resulting locally resonant granular chain is governed by

$$\begin{aligned} m_1 \frac{d^2\tilde{u}_n}{d\tilde{t}^2} &= \mathcal{A}(\tilde{u}_{n-1} - \tilde{u}_n)_+^\alpha - \mathcal{A}(\tilde{u}_n - \tilde{u}_{n+1})_+^\alpha - K(\tilde{u}_n - \tilde{v}_n) \\ m_2 \frac{d^2\tilde{v}_n}{d\tilde{t}^2} &= K(\tilde{u}_n - \tilde{v}_n) \end{aligned} \tag{3.1}$$

Here $\mathcal{A}(\tilde{u}_n - \tilde{u}_{n+1})_+^\alpha$ is the Hertzian contact interaction force between nth and $(n+1)$th particles, where $(x)_+ = x$ when $x > 0$ and equals zero otherwise, so the particles interact only when they are in contact, $\mathcal{A} > 0$ is the Hertzian constant, which depends on the material properties of the contacting particles and radius of the contact curvature, and $\alpha > 1$ is the nonlinear exponent of the contact interaction that depends on the shape of the particles and the mode of contact (e.g. $\alpha = 3/2$ for spherical beads and orthogonally stacked cylinders). Typically, we find $\alpha > 1$, although settings with $\alpha < 1$ have also been proposed; see e.g. [62] and references therein. In writing (3.1) we assume that the deformation of the particles in contact is confined to a sufficiently small region near the contact point and varies slowly enough on the time scale of interest, so that the static Hertzian law still holds [14]; this is known to be a well justified approximation in a variety of different settings [12, 13]. We also assume that dissipation and plastic deformation are negligible, which is generally a reasonable approximation, although dissipation effects have been argued to potentially lead to intriguing features in their own right, including secondary waves [63] (see also [64]). Choosing R to be a characteristic length scale, for example, the radius of spherical or cylindrical particles, we can introduce dimensionless variables

$$u_n = \frac{\tilde{u}_n}{R}, \quad v_n = \frac{\tilde{v}_n}{R}, \quad t = \tilde{t}\sqrt{\frac{R^{\alpha-1}\mathcal{A}}{m_1}}$$

and two dimensionless parameters

$$\rho = \frac{m_2}{m_1}, \quad \kappa = \frac{K}{\mathcal{A}R^{\alpha-1}},$$

where ρ is the ratio of two masses and κ measures the relative strength of the linear elastic spring. In the dimensionless variables the equations (3.1) become

$$\begin{aligned} \ddot{u}_n &= (u_{n-1} - u_n)_+^\alpha - (u_n - u_{n+1})_+^\alpha - \kappa(u_n - v_n) \\ \rho\ddot{v}_n &= \kappa(u_n - v_n), \end{aligned} \tag{3.2}$$

where $\ddot{u}_n$ and $\ddot{v}_n$ are the accelerations of the primary and secondary masses, respectively. In what follows, it will be sometimes convenient to consider (3.2) rewritten in terms of relative displacement (strain) variables $x_n = u_n - u_{n-1}$ and $y_n = v_n - v_{n-1}$:

$$\begin{aligned} \ddot{x}_n &= 2(-x_n)_+^\alpha - (-x_{n+1})_+^\alpha - (-x_{n-1})_+^\alpha - \kappa(x_n - y_n) \\ \rho\ddot{y}_n &= \kappa(x_n - y_n). \end{aligned} \tag{3.3}$$

Note that in the limit $\rho \to 0$, the model reduces to the one for a regular (non-resonant) homogeneous granular chain. Meanwhile, at $\rho \to \infty$ and zero initial conditions for $v_n(t)$ the system approaches a model of Newton's cradle, a granular chain with quadratic onsite potential, which is governed by [20, 65]

$$\ddot{u}_n + \kappa u_n = (u_{n-1} - u_n)_+^\alpha - (u_n - u_{n+1})_+^\alpha. \tag{3.4}$$

In [20], the discrete p-Schrödinger (DpS) equation

$$2i\tau_0 \frac{\partial A_n}{\partial \tau} = (A_{n+1} - A_n)|A_{n+1} - A_n|^{\alpha-1} - (A_n - A_{n-1})|A_n - A_{n-1}|^{\alpha-1} \tag{3.5}$$

has been derived at $\kappa = 1$ to capture the modulation of small-amplitude nearly harmonic oscillations in the form

$$u_n^{app}(t) = \varepsilon(A_n(\tau)e^{it} + \bar{A}_n(\tau)e^{-it}), \quad \tau = \varepsilon^{\alpha-1}t, \tag{3.6}$$

where $\varepsilon > 0$ is a small parameter, $A_n(\tau)$ is a slowly varying amplitude of the oscillations and τ_0 is a constant depending on α. In the next section, we follow a similar approach and use multiscale expansion to derive generalized modulation equations of the DpS type for (3.2) with finite ρ.

3.2 MODULATION EQUATIONS FOR SMALL-AMPLITUDE WAVES

3.2.1 Derivation of generalized DpS equations at finite ρ

Using the two-timing asymptotic expansion as in [20], we seek solutions of (3.2) in the form

$$u(t) = \varepsilon U(t,\tau), \quad v(t) = \varepsilon V(t,\tau)$$

where $\tau = \varepsilon^{\alpha-1}t$ is the slow time, and u, v, U and V are vectors with components u_n, v_n, U_n, V_n, respectively. The governing equations (3.2) then yield

$$\begin{aligned}(\partial_t + \varepsilon^{\alpha-1}\partial_\tau)^2 U &= \varepsilon^{\alpha-1}G(U) + \kappa(V-U)\\ (\partial_t + \varepsilon^{\alpha-1}\partial_\tau)^2 V &= \frac{\kappa}{\rho}(U-V),\end{aligned} \tag{3.7}$$

where the nonlinear term is given by

$$G(U)_n = (U_{n-1}-U_n)_+^\alpha - (U_n - U_{n+1})_+^\alpha.$$

The solution has the form

$$U = U^0 + \varepsilon^{\alpha-1}U^1 + o(\varepsilon^{\alpha-1}), \quad V = V^0 + \varepsilon^{\alpha-1}V^1 + o(\varepsilon^{\alpha-1}).$$

The 0th order terms satisfy a linear system, which after the elimination of secular terms yields

$$U^0 = B(\tau) + \kappa[A(\tau)e^{i\omega t} + \bar{A}(\tau)e^{-i\omega t}], \quad V^0 = B(\tau) - \frac{\kappa}{\rho}[A(\tau)e^{i\omega t} + \bar{A}(\tau)e^{-i\omega t}], \tag{3.8}$$

where $\omega = \sqrt{\kappa + \kappa/\rho}$ is the frequency of harmonic oscillations. This internal frequency of each resonator is associated with the out-of-phase motion of the displacements U and V. On the order $O(\varepsilon^{\alpha-1})$, the system (3.7) results in

$$\begin{aligned}(\partial_t^2 + \kappa)U^1 - \kappa V^1 &= -2\kappa\partial_\tau A i\omega e^{i\omega t} + c.c. + G(U^0)\\ \partial_t^2 V^1 - \frac{\kappa}{\rho}(U^1 - V^1) &= \frac{2\kappa}{\rho}\partial_\tau A i\omega e^{i\omega t} + c.c.\end{aligned} \tag{3.9}$$

where $c.c.$ denotes the complex conjugate. Let

$$J(f) = \frac{\omega}{2\pi}\int_0^{2\pi/\omega} f(t)e^{-i\omega t}dt \tag{3.10}$$

denote the projection of $f(t)$ on $e^{i\omega t}$ and define the averaging operator as

$$E(f) = \frac{\omega}{2\pi}\int_0^{2\pi/\omega} f(t)dt. \tag{3.11}$$

The projection operator on all remaining Fourier modes (of the form $e^{ij\omega t}$, $j \neq \pm 1$, $j \neq 0$) is given by

$$\Pi_h = I - E - e^{i\omega t}J - e^{-i\omega t}\bar{J}, \tag{3.12}$$

Let $U_h^1 = \Pi_h U^1$, $V_h^1 = \Pi_h V^1$. Then (3.9) yields

$$\begin{aligned}(\partial_t^2 + \kappa)U_h^1 - \kappa V_h^1 &= \Pi_h G(U^0)\\ \partial_t^2 V_h^1 - \frac{\kappa}{\rho}(U_h^1 - V_h^1) &= 0.\end{aligned}$$

Note that this equation has a unique $2\pi/\omega$-periodic solution $(U_h^1, V_h^1)^T$ because for each j such that $j \neq \pm 1$, $j \neq 0$, the matrix

$$\begin{bmatrix} \kappa - j^2\omega^2 & -\kappa \\ -\kappa/\rho & \kappa/\rho - j^2\omega^2 \end{bmatrix}$$

for the left hand side of the above equation associated with jth harmonic is invertible. Let

$$U^1 = U_h^1 + C^0(\tau) + C^1(\tau)e^{i\omega t} + c.c., \quad V^1 = V_h^1 + D^0(\tau) + D^1(\tau)e^{i\omega t} + c.c.$$

and project (3.9) on $e^{i\omega t}$, recalling that $\omega = \sqrt{\kappa + \kappa/\rho}$:

$$\begin{aligned}-(\kappa/\rho)C^1 - \kappa D^1 &= -2\kappa\partial_\tau A i\omega + J(G(U^0))\\ -(\kappa/\rho)C^1 - \kappa D^1 &= (2\kappa/\rho)\partial_\tau A i\omega.\end{aligned}$$

This yields the compatibility condition

$$2i\kappa\omega^3\partial_\tau A = J(G(U^0)) \tag{3.13}$$

and

$$D^1 = -\frac{\kappa}{\rho}(C^1 + 2i\omega\partial_\tau A).$$

Taking the average of (3.9), we obtain

$$\kappa(C^0 - D^0) = E(G(U^0))$$
$$-\frac{\kappa}{\rho}(C^0 - D^0) = 0.$$

Since ρ is finite, this yields $C^0 = D^0$, and hence the following condition can be obtained for the leading order solution:

$$E(G(U^0)) = 0. \tag{3.14}$$

To obtain the generalized DpS equations, we now consider the conditions (3.13) and (3.14) in more detail. Observe that for $b \in \mathbb{R}$, $z = re^{i\phi} \in \mathbb{C}$, we have

$$E[(-b + \kappa z e^{i\omega t} + \kappa \bar{z} e^{-i\omega t})_+^\alpha] = \frac{1}{2\pi}\int_0^{2\pi} (-b + 2\kappa r \cos t)_+^\alpha dt \equiv g_\alpha(b, r), \quad r = |z|. \tag{3.15}$$

Here we rescaled time in the averaging integral and used the fact that the result is independent of ϕ since we can always shift time when averaging. Similarly,

$$J[(-b+\kappa z e^{i\omega t} + \kappa \bar{z} e^{-i\omega t})_+^\alpha] = \frac{z}{2\pi r}\int_0^{2\pi} e^{-it}(-b+2\kappa r \cos t)_+^\alpha dt \equiv z h_\alpha(b, r), \quad r = |z|. \tag{3.16}$$

Defining the forward and backward shift operators

$$(\delta^+ A)_n = A_{n+1} - A_n, \quad (\delta^- A)_n = A_n - A_{n-1},$$

we observe that

$$G(U^0) = -\delta^+(-\delta^- U^0)_+^\alpha = -\delta^+(-\delta^- B(\tau) - \kappa\delta^- A(\tau)e^{i\omega t} - \kappa\delta^- \bar{A}(\tau)e^{-i\omega t})_+^\alpha,$$

where we used the first of (3.8) to obtain the second equality. Substituting this in (3.13) and (3.14) and using (3.15), (3.16) with $z = -\delta^- A$ and $b = \delta^- B$, we obtain the *generalized DpS equations*

$$2i\kappa\omega^3 \partial_\tau A = \delta^+[h_\alpha(\delta^- B, |\delta^- A|)\delta^- A] \tag{3.17}$$

and

$$\delta^+ g_\alpha(\delta^- B, |\delta^- A|) = 0. \tag{3.18}$$

3.2.2 DpS equation at large ρ

We now investigate the case of large ρ. Consider first the "critical" case when $\rho = \varepsilon^{1-\alpha}$. The 0th order problem is

$$\partial_t^2 U^0 = \kappa(V^0 - U^0), \quad \partial_t^2 V^0 = 0,$$

which yields

$$U^0 = B(\tau) + \kappa[A(\tau)e^{i\sqrt{\kappa}t} + \bar{A}(\tau)e^{-i\sqrt{\kappa}t}], \quad V^0 = B(\tau). \tag{3.19}$$

where we used the fact that $\omega = \sqrt{\kappa}$ when $\rho \to \infty$. Meanwhile, the $O(\varepsilon^{\alpha-1})$ problem becomes

$$\begin{aligned}
&(\partial_t^2 + \kappa)U^1 - \kappa V^1 = -2i\kappa^{3/2}\partial_\tau A e^{i\sqrt{\kappa}t} + c.c. + G(U^0) \\
&\partial_t^2 V^1 = \kappa^2 A e^{i\sqrt{\kappa}t} + c.c.
\end{aligned}$$

Note that the right hand side of the second equation has zero time average, as it should to be consistent with the left hand side, and the equation yields

$$V^1 = -\kappa A(\tau)e^{i\sqrt{\kappa}t} + c.c. + D^0(\tau).$$

Putting this back into the first equation and projecting on $e^{i\sqrt{\kappa}t}$, we get

$$2\kappa^{3/2} i\partial_\tau A + \kappa^2 A = J[G(U^0)],$$

which is *almost* like the DpS equation in [20] if we set $\kappa = 1$. Note, however, the additional term $\kappa^2 A$ in the left hand side and the fact that U^0 also includes $B(\tau)$. Observe further that there are no conditions to determine B at this order. If $B = 0$, we get (a modified) DpS equation for A only.

Now suppose $\rho = \varepsilon^{1-\gamma}$, $\gamma > \alpha$. Then the 0th order equation is the same, so the solution is still given by (3.19), while on $O(\varepsilon^{\alpha-1})$ we get

$$\begin{aligned}
&(\partial_t^2 + \kappa)U^1 - \kappa V^1 = -2\kappa^{3/2}\partial_\tau A i e^{i\sqrt{\kappa}t} + c.c. + G(U^0) \\
&\partial_t^2 V^1 = 0,
\end{aligned}$$

so the second equation yields $V^1 = D_0(\tau)$, while the projection of the first on $e^{i\sqrt{\kappa}t}$ yields the DpS equation for Newton's cradle model:

$$2\kappa^{3/2} i\partial_\tau A = J[G(U^0)].$$

Note that $B(\tau)$ in (3.19) is again not determined at this order. Observe, however, that in the limit $\rho \to \infty$ the initial conditions $v(0) = \dot{v}(0) = 0$ yield $v(t) \equiv 0$ (and thus $V^0 = V^1 = 0$), and we recover (3.6) and the DpS equation (3.5) at $\kappa = 1$:

$$i\,\partial_\tau A = \omega_0\,\delta^+[|\delta^- A|^{\alpha-1}\delta^- A] \tag{3.20}$$

with (see [20])

$$\omega_0 = \frac{2^{\alpha-2}}{\sqrt{\pi}}\frac{\Gamma(\alpha/2+1)}{\Gamma((\alpha+1)/2+1)}. \tag{3.21}$$

In Theorem 3.2.1 below, we justify the DpS equation (3.20) on long time scales, for suitable small-amplitude initial conditions. We obtain error estimates between solutions of (3.2) and modulated profiles described by DpS. We seek solutions of (3.2) and the DpS equation in the usual sequence spaces ℓ_p with $1 \le p \le +\infty$. For simplicity we state Theorem 3.2.1 in the case $\kappa = 1$.

Theorem 3.2.1. *Fix constants $C_{\rm r}, C_{\rm i}, T > 0$ and a solution $A \in \mathcal{C}^2([0,T],\ell_p)$ of the DpS equation (3.20). There exist constants $\varepsilon_T > 0$ and $C_T \ge C_{\rm i}$ such that the following holds: For all $\varepsilon \le \varepsilon_T$ and for $\rho^{-1} \le C_{\rm r}\,\varepsilon^{2(\alpha-1)}$, for all initial condition $(u(0), v(0), \dot{u}(0), \dot{v}(0)) \in \ell_p^4$ satisfying*

$$\|u(0) - 2\varepsilon\,\mathrm{Re}\,A(0)\|_p + \|\dot{u}(0) + 2\varepsilon\,\mathrm{Im}\,A(0)\|_p \le C_{\rm i}\varepsilon^\alpha, \tag{3.22}$$

$$\|v(0)\|_p \le C_{\rm i}\varepsilon^\alpha, \quad \|\dot{v}(0)\|_p \le C_{\rm i}\varepsilon^{2\alpha-1}, \tag{3.23}$$

the corresponding solution of (3.2) satisfies for all $t \in [0, T/\varepsilon^{\alpha-1}]$

$$\|u(t) - 2\varepsilon\,\mathrm{Re}\,(A(\varepsilon^{\alpha-1}t)\,e^{it})\|_p + \|\dot{u}(t) + 2\varepsilon\,\mathrm{Im}\,(A(\varepsilon^{\alpha-1}t)\,e^{it})\|_p \le C_T\varepsilon^\alpha, \tag{3.24}$$

$$\|v(t)\|_p \le C_T\varepsilon^\alpha, \quad \|\dot{v}(t)\|_p \le C_T\varepsilon^{2\alpha-1}. \tag{3.25}$$

Similarly to what was established in [61] for Newton's cradle problem, Theorem 3.2.1 shows that small $O(\varepsilon)$ solutions of (3.2) are described by the DpS equation over long (but finite) times of order $\varepsilon^{1-\alpha}$. However, there are important differences compared to the results of [61]. Firstly, the DpS approximation is not valid for all small-amplitude initial conditions, since one has to assume that $v(0)$ and $\dot{v}(0)$ are small enough (see (3.23)). Secondly, ρ must be large when ε is small. More precisely, ρ must be greater than $\varepsilon^{2(1-\alpha)}$, which scales as the square of the characteristic time scale of DpS. This is due to the translational invariance of (3.2), which introduces a Jordan block in the linearization of (3.2) around the trivial state, inducing a quadratic growth of secular terms (see the estimate (3.44) below).

Let us now prove Theorem 3.2.1. The main steps are Gronwall estimates to obtain solutions of (3.2) close to solutions of the Newton's cradle problem (3.4) when ρ is large, and the use of the results of [61] to approximate solutions of (3.4) with the DpS equation.

Equation (3.2) at $\kappa = 1$ reads

$$\ddot{u} + u - v = G(u), \tag{3.26}$$

$$\ddot{v} = \sigma\,(u - v), \tag{3.27}$$

where $\sigma := 1/\rho$ is a small parameter satisfying

$$\sigma \leq C_{\rm r}\,\varepsilon^{2(\alpha-1)}, \tag{3.28}$$

as assumed in Theorem 3.2.1. In addition, we have

$$\|G(u)\|_p = O(\|u\|_p^\alpha), \quad \|DG(u)\|_{\mathcal{L}(\ell_p)} = O(\|u\|_p^{\alpha-1}). \tag{3.29}$$

To simplify subsequent estimates, it is convenient to uncouple the linear parts of (3.26) and (3.27), which can be achieved by making the change of variables

$$u = Q + R, \quad v = R - \sigma\,Q.$$

System (3.26)-(3.27) is equivalent to

$$\ddot{Q} + Q = \chi\,G(Q + R) - \sigma\,Q, \tag{3.30}$$

$$\ddot{R} = \chi\sigma\,G(Q + R), \tag{3.31}$$

where $\chi = (1+\sigma)^{-1}$ is close to unity.

To approximate the dynamics of (3.30)-(3.31) when σ is small, we first consider the case $\sigma = 0$ and $R = 0$ of (3.30) (leading to the Newton's cradle problem) and use the results of [61] relating Newton's cradle problem to the DpS equation. More precisely, given the solution A of the DpS equation considered in Theorem 3.2.1, we introduce the solution $Q_{\rm a}$ of

$$\ddot{Q}_{\rm a} + Q_{\rm a} = G(Q_{\rm a})$$

with initial condition $Q_{\rm a}(0) = 2\varepsilon\,\mathrm{Re}\,A(0)$, $\dot{Q}_{\rm a}(0) = -2\varepsilon\,\mathrm{Im}\,A(0)$. According to Theorem 2.10 of [61], for ε small enough, the solution $Q_{\rm a}$ is defined on a maximal interval of existence (t^-, t^+) containing $[0, T\,\varepsilon^{1-\alpha}]$ and satisfies for all $t \in [0, T\,\varepsilon^{1-\alpha}]$

$$\|Q_{\rm a}(t) - 2\varepsilon\,\mathrm{Re}\,(A(\varepsilon^{\alpha-1}t)\,e^{it})\|_p + \|\dot{Q}_{\rm a}(t) + 2\varepsilon\,\mathrm{Im}\,(A(\varepsilon^{\alpha-1}t)\,e^{it})\|_p \leq C\,\varepsilon^{\alpha}. \tag{3.32}$$

This implies in particular that

$$\|Q_{\rm a}\|_{L^\infty((0,T\,\varepsilon^{1-\alpha}),\ell_p)} + \|\dot{Q}_{\rm a}\|_{L^\infty((0,T\,\varepsilon^{1-\alpha}),\ell_p)} \leq M\,\varepsilon. \tag{3.33}$$

Next, our aim is to show that Q remains close to $Q_{\rm a}$ (and its DpS approximation) and R remains small over long times, for suitable initial conditions, ε small enough and ρ large enough (i.e. σ small enough). Setting $Q = Q_{\rm a} + W$ in (3.30)-(3.31) yields

$$\ddot{W} + W = N(W,R) \tag{3.34}$$

$$\ddot{R} = \chi\sigma\,G(Q_{\rm a} + W + R), \tag{3.35}$$

where

$$N(W,R) = -\sigma(Q_{\rm a} + \chi\,G(Q_{\rm a})) + \chi\,[\,G(Q_{\rm a} + W + R) - G(Q_{\rm a})\,] - \sigma\,W. \tag{3.36}$$

Moreover, from the identities

$$W = Q - Q_{\rm a} = (1+\sigma)^{-1}\,(u - v) - Q_{\rm a}, \quad R = (1+\sigma)^{-1}\,(\sigma u + v)$$

and the assumptions (3.22)-(3.23) and (3.28), it follows that

$$\|W(0)\|_p + \|\dot{W}(0)\|_p \leq C\,\varepsilon^{\alpha}, \tag{3.37}$$

$$\|R(0)\|_p \leq C\,\varepsilon^{\alpha}, \quad \|\dot{R}(0)\|_p \leq C\,\varepsilon^{2\alpha-1}. \tag{3.38}$$

Let $X = (W, R, \dot{W}, \dot{R})$ and $\|X\|_p$ denote the sum of the ℓ_p norms of each component. We shall now use Gronwall estimates to bound $\|X(t)\|_p$ on the time scale considered in Theorem 3.2.1.

The solutions of (3.34)-(3.35) corresponding to initial conditions satisfying (3.37)-(3.38) are defined on a maximal interval of existence $(t_{\min}, t_{\max})$ with $t_{\min} < 0$ and $t_{\max} \leq t^+$, which depends a priori on the initial condition and parameters (in particular ε). From (3.37)-(3.38), one can infer that $\|X(0)\|_p < M\,\varepsilon$ (the size of $Q_{\rm a}$ in (3.33)) for ε small enough. Let

$$t_\varepsilon = \sup\{t \in (0, \min(T\,\varepsilon^{1-\alpha}, t_{\max})) :\ \forall s \in (0,t),\ \|X(s)\|_p \leq M\,\varepsilon\}. \tag{3.39}$$

From (3.33) and the triangle inequality, we obtain

$$\|Q_{\rm a}(t) + W(t) + R(t)\|_p \leq 2\,M\,\varepsilon, \quad \forall\, t \in [0, t_\varepsilon]. \tag{3.40}$$

In addition, from definition (3.39) we have either

$$t_\varepsilon < \min(T\,\varepsilon^{1-\alpha}, t_{\max}) \text{ and } \|X(t_\varepsilon)\|_p = M\,\varepsilon \tag{3.41}$$

or

$$t_\varepsilon = T\,\varepsilon^{1-\alpha} < t_{\max} \tag{3.42}$$

(if $\|X\|_p$ is bounded on $[0, t_{\max})$, then $t_{\max} = t^+ > T\,\varepsilon^{1-\alpha}$). Integrating (3.35) twice yields

$$R(t) = \dot{r}(0)\,t + R(0) + \chi\sigma \int_0^t (t-s)\,G(Q_{\rm a} + W + R)(s)\,ds. \tag{3.43}$$

Using the fact that $t_\varepsilon \leq T\,\varepsilon^{1-\alpha}$, estimate (3.40) and the first bound in (3.29), one obtains from the above identity the following inequality:

$$\forall t \in [0, t_\varepsilon],\ \|R(t)\|_p \leq T\,\varepsilon^{1-\alpha}\|\dot{R}(0)\|_p + \|R(0)\|_p + C_1\,\sigma\,\varepsilon^{2-\alpha}. \tag{3.44}$$

Then the assumption (3.28) and the property (3.38) yield

$$\forall t \in [0, t_\varepsilon],\ \|R(t)\|_p \leq C\,\varepsilon^{\alpha}. \tag{3.45}$$

Similarly, we have

$$\dot{R}(t) = \dot{R}(0) + \chi\sigma \int_0^t G(Q_{\mathrm{a}} + W + R)(s)\, ds, \tag{3.46}$$

which implies

$$\forall t \in [0, t_\varepsilon],\ \|\dot{R}(t)\|_p \leq \|\dot{R}(0)\|_p + O(\sigma\,\varepsilon) \leq C\,\varepsilon^{2\alpha-1}. \tag{3.47}$$

Moreover, using Duhamel's formula in (3.34) yields

$$W(t) = \cos t\, W(0) + \sin t\, \dot{W}(0) + \int_0^t \sin(t-s)\, [N(W,R)](s)\, ds.$$

Recalling that $t_\varepsilon \leq T\,\varepsilon^{1-\alpha}$, using (3.37), and using (3.33), (3.28), (3.29) and (3.45) to estimate $N(W,R)$ from the definition (3.36), we get

$$\forall t \in [0, t_\varepsilon],\ \|W(t)\|_p \leq C_1\,\varepsilon^\alpha + C_2\,\varepsilon^{\alpha-1} \int_0^t \|W(s)\|_p\, ds. \tag{3.48}$$

By Gronwall's lemma we then have

$$\forall t \in [0, t_\varepsilon],\ \|W(t)\|_p \leq C_1\, e^{C_2\, T}\, \varepsilon^\alpha. \tag{3.49}$$

Similarly, we obtain

$$\dot{W}(t) = -\sin t\, W(0) + \cos t\, \dot{W}(0) + \int_0^t \cos(t-s)\, [N(W,R)](s)\, ds.$$

Using the same estimates as the ones involved in proving (3.48) and estimate (3.49), one can show that the above identity yields

$$\forall t \in [0, t_\varepsilon],\ \|\dot{W}(t)\|_p \leq C\,\varepsilon^\alpha. \tag{3.50}$$

Summing estimates (3.45), (3.47), (3.49), (3.50), we find that $\|X(t)\|_p = O(\varepsilon^\alpha) < M\,\varepsilon$ for all $t \in [0, t_\varepsilon]$ if ε is small enough. Consequently, the property (3.41) is not satisfied, which implies that (3.42) must hold instead. We therefore have

$$t_\varepsilon = T\,\varepsilon^{1-\alpha}$$

in estimates (3.45), (3.47), (3.49) and (3.50). Combining these estimates with the DpS error bound (3.32) and the assumption (3.28), we deduce the error bounds (3.24), (3.25) from the identities

$$u(t) - 2\varepsilon \,\mathrm{Re}\,(A(\varepsilon^{\alpha-1}t)\, e^{it}) = W(t) + R(t) + Q_{\mathrm{a}}(t) - 2\varepsilon \,\mathrm{Re}\,(A(\varepsilon^{\alpha-1}t)\, e^{it}),$$

$$\dot{u}(t) + 2\varepsilon \,\mathrm{Im}\,(A(\varepsilon^{\alpha-1}t)\, e^{it}) = \dot{W}(t) + \dot{R}(t) + \dot{Q}_{\mathrm{a}}(t) + 2\varepsilon \,\mathrm{Im}\,(A(\varepsilon^{\alpha-1}t)\, e^{it}),$$

$$v = R - \sigma\, Q_{\mathrm{a}} - \sigma\, W.$$

This completes the proof of Theorem 3.2.1.

3.3 TIME-PERIODIC TRAVELING WAVES

We now use the DpS equations to investigate time-periodic traveling wave solutions of our system. In what follows, it will be convenient to use the strain formulation (3.3) and also rewrite the DpS equation (3.17) in terms of strain-like variables

$$2i\kappa\omega^3 \partial_\tau \delta^- A_n = \delta^+[h_\alpha(\delta^- B_n, |\delta^- A_n|)\delta^- A_n] - \delta^+[h_\alpha(\delta^- B_{n-1}, |\delta^- A_{n-1}|)\delta^- A_{n-1}]. \tag{3.51}$$

A special class of solution of (3.51), (3.18) has the form of a *periodic traveling wave*

$$\delta^- A_n(\tau) = a e^{i(\Omega\tau - qn - \phi)}, \quad \delta^- B_n(\tau) = b, \tag{3.52}$$

where the frequency Ω depends on the amplitude $a > 0$, the constant b and the wave number q through the nonlinear dispersion relation

$$\Omega = \frac{2}{\kappa\omega^3} \left|\sin\frac{q}{2}\right|^2 h_\alpha(b, a). \tag{3.53}$$

Note that definition of h_α in (3.16) requires that $b \le 2\kappa a$. In particular, the dispersion relation has a closed form when $b = 0$. In fact, as shown in [20] for $\kappa = 1$, in this case

$$h_\alpha(0, r) = 2^{\alpha-1} c_\alpha \kappa^\alpha r^{\alpha-1}, \quad c_\alpha = \frac{1}{\pi} \frac{\Gamma(1/2)\Gamma(\alpha/2+1)}{\Gamma((\alpha+1)/2+1)},$$

and the dispersion relation is given by

$$\Omega_0 = \frac{c_\alpha 2^\alpha (\kappa a)^{\alpha-1}}{\omega^3} \left|\sin\frac{q}{2}\right|^2.$$

Equations (3.8), (3.52) and (3.53) yield the following first-order approximation of the periodic traveling wave solutions of system (3.3):

$$x_n^{tw}(t) = \varepsilon b + 2\kappa\varepsilon a\cos(nq - \omega_{tw}t + \phi), \quad y_n^{tw}(t) = \varepsilon b - \frac{2\kappa\varepsilon a}{\rho}\cos(nq - \omega_{tw}t + \phi), \tag{3.54}$$

where ω_{tw} is the traveling wave frequency given by

$$\omega_{tw} = \Omega\varepsilon^{\alpha-1} + \omega = \omega + \frac{2\varepsilon^{\alpha-1}}{\kappa\omega^3}\left|\sin\frac{q}{2}\right|^2 h_\alpha(b,a). \tag{3.55}$$

To investigate how well the dynamics governed by the DpS equations approximates the traveling wave solutions of (3.3), we consider initial conditions determined from the first-order approximation (3.8):

$$\begin{aligned} x_n^{app}(t) &= \varepsilon\delta^- B_n(\varepsilon^{\alpha-1}t) + \kappa\varepsilon\delta^- A_n(\varepsilon^{\alpha-1}t)e^{i\omega t} + c.c. \\ y_n^{app}(t) &= \varepsilon\delta^- B_n(\varepsilon^{\alpha-1}t) - \frac{\kappa\varepsilon}{\rho}\delta^- A_n(\varepsilon^{\alpha-1}t)e^{i\omega t} + c.c. \end{aligned} \tag{3.56}$$

at $t = 0$, along with initial velocities given by

$$\begin{aligned} \dot{x}_n(0) &= \varepsilon\{\varepsilon^{\alpha-1}\delta^-\dot{B}_n(0) + \kappa\varepsilon^{\alpha-1}\delta^-\dot{A}_n(0) + i\kappa\omega\delta^- A_n(0) + c.c\} \\ \dot{y}_n(0) &= \varepsilon\{\varepsilon^{\alpha-1}\delta^-\dot{B}_n(0) - \frac{\kappa}{\rho}\varepsilon^{\alpha-1}\delta^-\dot{A}_n(0) - i\frac{\kappa}{\rho}\omega\delta^- A_n(0) + c.c\}. \end{aligned} \tag{3.57}$$

Here $\delta^- A_n(0)$ are set to be small perturbations of (3.52) at $\tau = 0$ and $\phi = 0$:

$$\delta^- A_n(0) = a[(1+\zeta_n^{(1)})\cos(nq) - i(1+\zeta_n^{(2)})\sin(nq)], \tag{3.58}$$

where $\zeta_n^{(1)}$ and $\zeta_n^{(2)}$ are uniformly distributed random variables in $[-\zeta,\zeta]$ with small $\zeta > 0$. Let $C = g_\alpha(b,|a|) > 0$ for given constants a and $b < 2\kappa|a|$. Then $\delta^- B_n(\tau)$ is determined from (3.18) by numerically solving

$$g_\alpha(\delta^- B_n(\tau), |\delta^- A_n(\tau)|) = C. \tag{3.59}$$

From the definition of g_α in (3.15), it is clear that the function $b \mapsto g_\alpha(b,r)$ is decreasing on $(-\infty, 2\kappa r)$ and satisfies $\lim_{b\to-\infty} g_\alpha(b,r) = +\infty$ and $g_\alpha(b,r) = 0$ for $b \geq 2\kappa r$. Consequently

equation (3.59) admits a unique solution $\delta^- B_n(\tau) \in (-\infty, 2\kappa|\delta^- A_n(\tau)|)$. In particular, we obtain the value of $\delta^- B_n(0)$ by solving (3.59) at $\tau = 0$. Note that $\delta^- \dot{A}_n(0)$ and $\delta^- \dot{B}_n(0)$ can be computed exactly using DpS equations (3.51), (3.59), although their contribution is negligible since they correspond to higher order terms in the expression of initial velocities $\dot{x}_n(0)$ and $\dot{y}_n(0)$. In particular, when the perturbation is zero (i.e. $\zeta = 0$), the initial condition simplifies to

$$\begin{aligned} x_n(0) &= \varepsilon b + 2\varepsilon\kappa a \cos(nq+\phi), \quad y_n(0) = \varepsilon b - \frac{2\varepsilon\kappa a}{\rho}\cos(nq+\phi), \\ \dot{x}_n(0) &= 2\omega_{tw}\kappa\varepsilon a \sin(nq+\phi), \quad \dot{y}_n(0) = -\frac{2\omega_{tw}\kappa\varepsilon a}{\rho}\sin(nq+\phi). \end{aligned} \tag{3.60}$$

Integrating (3.3) numerically on a finite chain with these initial conditions and using periodic boundary conditions $x_0 = x_N$, $x_{N+1} = x_1$, we can compare the solution of (3.3) (referred to in what follows as the numerical solution) with the ansatz (3.54) when $\zeta = 0$ or the ansatz (3.56) when $\zeta > 0$. The latter is obtained by solving (3.51), (3.59) with periodic boundary conditions $\delta^- A_0(\tau) = \delta^- A_N(\tau)$, $\delta^- A_{N+1}(\tau) = \delta^- A_1(\tau)$, using the Runge-Kutta method and a standard numerical root finding routine to determine $\delta^- B_n(\tau)$ from (3.59) for given $\delta^- A_n(\tau)$ at each step.

3.3.1 Numerical traveling waves and the DpS approximation

We now consider a locally resonant chain with $N = 50$ masses. In what follows, we set $\kappa = 1$, noting that other values of this parameter can be recovered by the appropriate rescaling of time and amplitude. To investigate the accuracy of the DpS approximation of the small-amplitude traveling waves, we first fix mass ratio $\rho = 1/3$ and normalize the traveling wave solution (3.52) by fixing $a = 1$, $\phi = 0$ and $b = 1$. The linear frequency is given by $\omega = \sqrt{\kappa + \kappa/\rho} = 2$.

In the first numerical run, we set $q = \pi/5$, $\zeta = 0$ and consider the traveling wave with frequency $\omega_{tw} = \omega + 0.001$, so that $\varepsilon \approx 0.057$ from the nonlinear dispersion relation (3.55). Equation (3.54) then yields the amplitude of x_n^{tw} approximately equal to 0.114, which corresponds to the small-amplitude regime. As shown in the left panel of Fig. 3.1, the agreement between the numerical and approximate solutions is excellent, even after a

long time $t = 100\,T_{tw}$, where $T_{tw} = 2\pi/\omega_{tw} = 3.126$ is the period of the traveling wave. The relative errors of the approximate solutions

$$E_x(t) = \frac{1}{2\varepsilon\kappa a}||x_n^{app}(t) - x_n(t)||_\infty \quad \text{and} \quad E_y(t) = \frac{\rho}{2\varepsilon\kappa a}||y_n^{app}(t) - y_n(t)||_\infty \tag{3.61}$$

are less than 8% at the final time of computation and remain bounded throughout the reported time evolution, as shown in the right panel of Fig. 3.1. In the second numerical

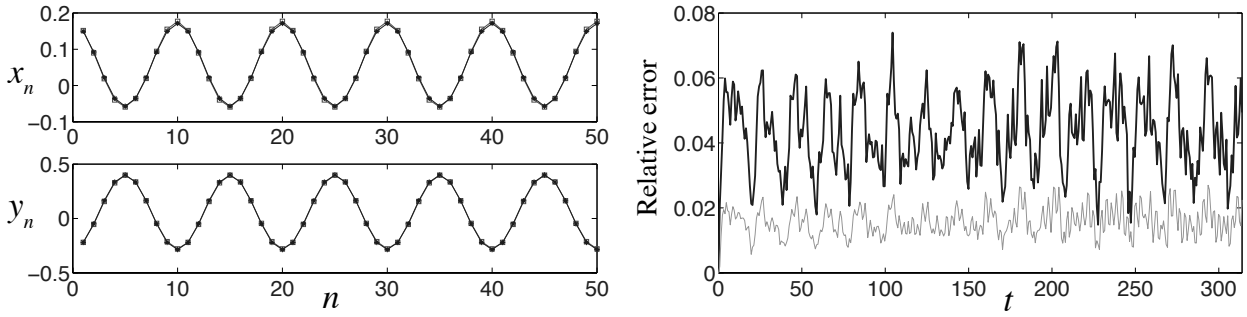

Figure 3.1: Left plot: strain profiles of small-amplitude approximate solution (3.54) (connected stars) and numerical solution of (3.3) (connected squares) at $t = 100\,T_{tw} \approx 314$. Right plot: the relative errors $E_x(t)$ (black curve) and $E_y(t)$ (grey curve) of the DpS approximation. Here $\phi = 0$, $k = 1$, $q = \pi/5$, $b = 1$, $a = 1$, $\zeta = 0$ and $\omega_{tw} = w + 0.001$.

run, we set $\zeta = 0.01$ for the perturbation in (3.58), while the other parameters remain the same. The agreement between the numerical and approximate solutions is still excellent over the same time interval (see the left plot of Fig. 3.2). Moreover, the right plot of Fig. 3.2 shows the normalized differences

$$\widetilde{E}_x(t) = \frac{1}{2\varepsilon\kappa a}||x_n^{ptd}(t) - x_n(t)||_\infty \quad \text{and} \quad \widetilde{E}_y(t) = \frac{\rho}{2\varepsilon\kappa a}||y_n^{ptd}(t) - y_n(t)||_\infty \tag{3.62}$$

between a perturbed traveling wave (x_n^{ptd}, y_n^{ptd}) (numerical solution obtained for the perturbed initial condition) and the unperturbed numerical traveling wave solution (x_n, y_n) shown in Fig. 3.1 with the wave number $q = \pi/5$. As shown by Fig. 3.2, the initial perturbation is not amplified at the early stage of the numerical integration of (3.3) (for $t \leq 50 \approx 16\,T_{tw}$). However, the subsequent growth of perturbations indicates the instability of the traveling wave solution.

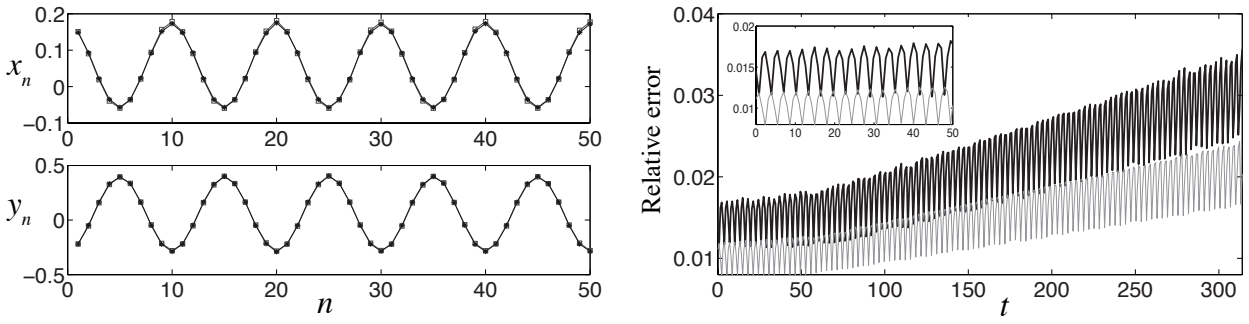

Figure 3.2: Left plot: strain profiles of small-amplitude approximate solution (connected stars) from the ansatz (3.56) and perturbed traveling wave solution (connected squares) at $t = 100\,T_{tw} \approx 314$. Right plot: the normalized differences $\widetilde{E}_x(t)$ (black curve) and $\widetilde{E}_y(t)$ (grey curve) of the perturbed traveling wave and the unperturbed solution shown in Fig. 3.1. Here $\zeta = 0.01$ and all the other parameters are the same as in Fig. 3.1. A growth of the perturbations can be clearly observed in the dynamics.

In the next computation, we increase the wave number up to $q = 4\pi/5$ and keep all the other parameters the same as before. Now the asymptotic scale becomes quite small as $\varepsilon \approx 6.37 \times 10^{-4}$, which yields a very small amplitude of $x_n^{tw} \approx 0.0013$. As shown in Fig. 3.3, the DpS equations can successfully capture the dynamics of the small-amplitude traveling wave solution of the original system. In addition, the small-amplitude traveling wave with $q = 4\pi/5$ appears to be stable on the interval $t \in [0, 600]$. However, this result may be linked with the very small traveling wave amplitude, and instabilities might appear on longer time scales.

It is worth pointing out that the time scale of the validity of the DpS approximation depends not only on the asymptotic scale ε but also on the wave number q. To illustrate this, we first consider the wave number $q = \pi/5$ but increase the traveling wave frequency up to $\omega_{tw} = \omega + 0.003$, which yields $\varepsilon \approx 0.514$ and the amplitude of x_n^{tw} around 1.028. As revealed by the left plot in Fig. 3.4, the DpS equations fail to describe the dynamics of (3.3) appropriately soon after we start the integration. We then increase the wave number up to $q = 4\pi/5$ but choose $\omega_{tw} = \omega + 0.009$ yielding $\varepsilon \approx 0.0516$, which is even smaller than the asymptotic scale ε used in Fig. 3.1. However, notable difference between the traveling wave patterns of the numerical and approximate solutions are observed over the same time interval $[0, 314]$ (see the right plot of Fig. 3.4).

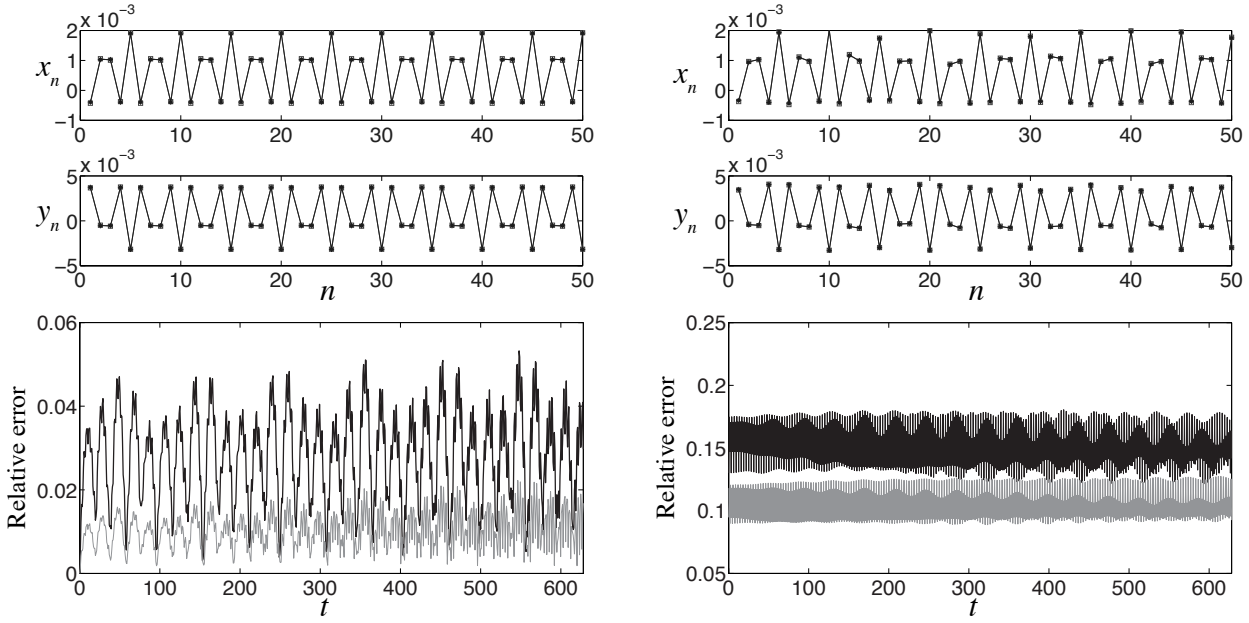

Figure 3.3: Top panels: strain profiles of small-amplitude approximate solution (connected stars) from the ansatz (3.56) and numerical results (connected squares) with both unperturbed (left) and perturbed initial conditions with $\zeta = 0.1$ (right) at $t = 200\,T_{tw} \approx 628$, respectively. Bottom panels: left plot shows the relative errors $E_x(t)$ (black curve) and $E_y(t)$ (grey curve) of the DpS approximation. Right plot shows the normalized differences $\widetilde{E}_x(t)$ (black curve) and $\widetilde{E}_y(t)$ (grey curve) between the perturbed and unperturbed traveling waves. Here $q = 4\pi/5$ and all the other parameters are the same as in Fig. 3.1.

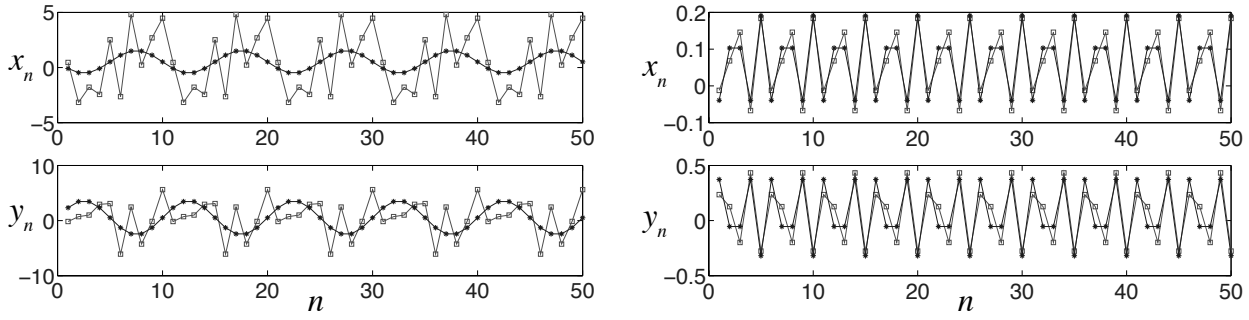

Figure 3.4: Left panel: results of the simulations with the same parameters as in Fig. 3.1 except for $\omega_{tw} = \omega + 0.003$ and the snapshot is taken at $t = 10\,T_{tw} \approx 31.4$. Right panel: results of the simulations with the same parameters as in the left panels of Fig. 3.3 except for $\omega_{tw} = \omega + 0.009$ and the snapshot is taken at $t = 314$.

3.3.2 Effect of mass ratio ρ

To investigate the effect of the mass ratio ρ on the validity of the DpS approximation of the small-amplitude traveling waves, we fix $q = \pi/5$, $\varepsilon = 0.01$ and keep the other parameters the same as before. We choose mass ratio $\rho = 3$ and the traveling wave frequency in (3.55) is now given by $\omega_{tw} \approx \omega + 0.002$, where the linear frequency is $\omega = 1.1547$. The results of the simulations are shown in Fig. 3.5. We observe again that the agreement between the numerical and approximate solutions remains excellent over the time interval $[0, 100\,T_{tw}]$, and the numerical traveling waves appear to be stable over the time interval [0, 100]. However, we note the growing trend of the difference between the perturbed and unperturbed traveling wave solutions after $t \approx 100$, which illustrates the instability of the traveling wave.

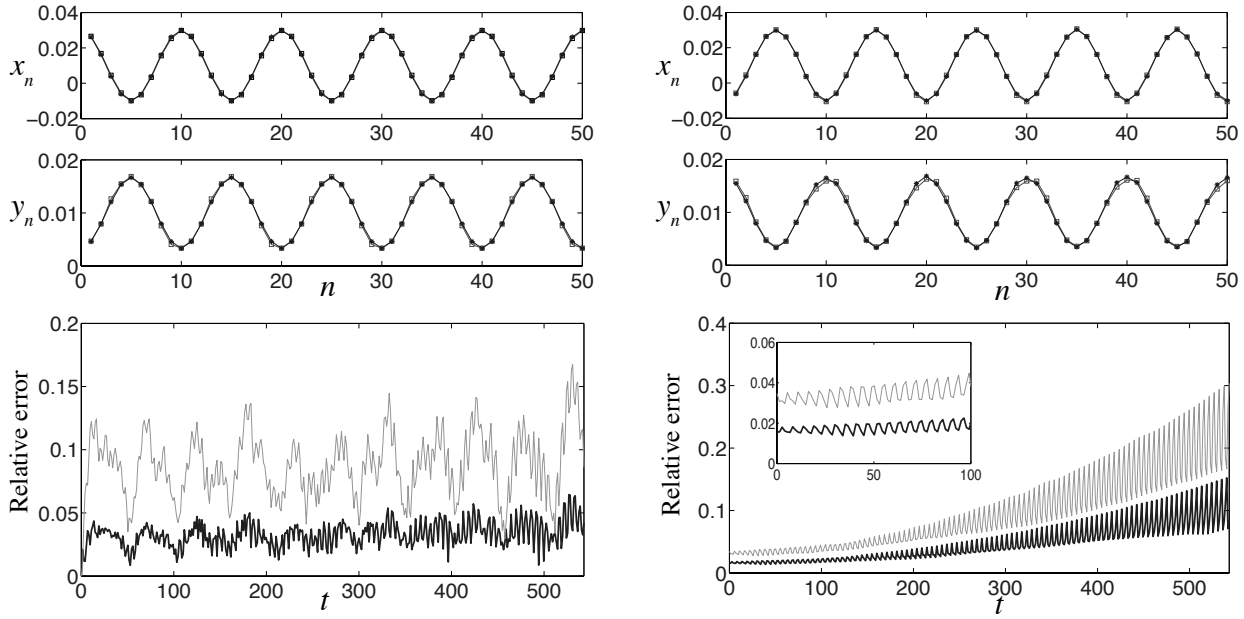

Figure 3.5: Results of the simulations with the same parameters as in Fig. 3.3 except for $\rho = 3$, $q = \pi/5$ and $\varepsilon = 0.01$. The strain profiles of both panels correspond to snapshots taken at $t = 100\,T_{tw}$ and the perturbation added in the initial condition is $\zeta = 0.01$.

We further increase ρ to the critical value $\rho_c = \varepsilon^{1-\alpha} = 10$. The linear and traveling wave frequencies are given by $\omega = 1.0488$ and $\omega_{tw} = 1.0517$, respectively. As shown by the left panel of Fig. 3.6, the wave form of y_n is no longer sinusoidal at $t = 100\,T_{tw}$, while the wave form of x_n remains sinusoidal and matches its DpS approximation very well over the time interval $[0, 100\,T_{tw}]$. We observe also a growing trend in the relative error between the

numerical and approximate solutions, despite the structural similarities of the profiles. To

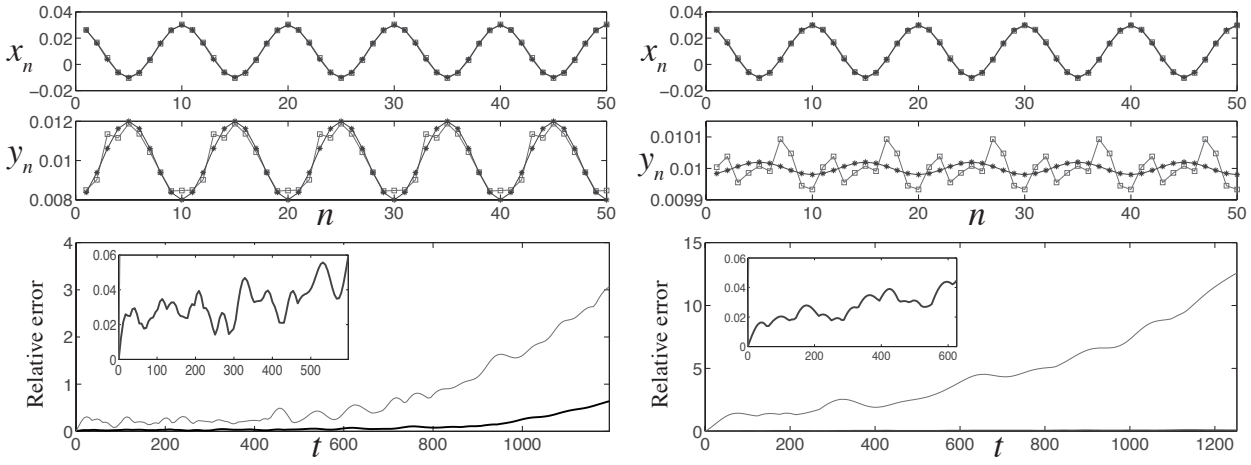

Figure 3.6: Results of the simulations with the same parameters as in the left panel of Fig. 3.5 except for $\rho = 10$ (left panel) and $\rho = 1000$ (right panel). The strain profiles of both panels correspond to the snapshot taken at $t = 100\,T_{tw}$. The insets in the bottom plots show the enlarged plots of the relative error $E_x(t)$.

investigate the case when ρ is large ($O(\varepsilon^{1-\gamma}), \gamma > \alpha$), we now set $\rho = 1000$ and keep all other parameters the same as before. The linear frequency is now given by $\omega = 1.0005$ and approximate frequency is $\omega_{tw} = 1.0038$. Again, over the integration time interval $[0, 100\,T_{tw}]$ the wave form of x_n remains sinusoidal and close to the ansatz (3.54) but the waveform of y_n is non-sinusoidal and significantly deviates from the DpS traveling wave approximation (see the right plots in Fig. 3.6). These results are consistent with the discussion in Sec. 3.2.1, since the derivation of the DpS equations (3.17)-(3.18) requires that ρ is below the critical value $\rho_c = \varepsilon^{1-\alpha}$ for given ε. Note that if we further set $b = 0$, the DpS equation (3.17) reduces to the one capturing the traveling waves in Newton's cradle problem in [20]. Numerical results (not reported here) reveal that the numerical solution of x_n is sinusoidal and very well approximated by the traveling wave ansatz (3.54). However, the difference between exact and approximate solutions of y_n is very substantial. Here the structural characteristics of the solution for y_n are no longer properly captured by the DpS approximation.

These numerical simulations reveal that the validity of the DpS approximation at fixed wave number q is very sensitive to the mass ratio ρ. When ρ is relatively small, the generalized DpS equations (3.17)-(3.18) successfully capture the dynamics of periodic traveling waves. When $\rho \geq \rho_c = \varepsilon^{1-\alpha}$, an increasing deviation between the exact and approximate solutions

of y_n emerges. However, in all cases, the agreement of approximate and numerical solutions for x_n remains excellent over a finite time interval. In addition, traveling wave instabilities can be observed depending on the values of ρ, wave number q, wave amplitude and time scales considered.

3.4 BRIGHT BREATHERS

Bright breathers are time-periodic solutions of (3.2) which converge to constants (zero strain) at infinity, i.e.

$$u_n, v_n \to c_\pm, \quad \text{as} \quad n \to \pm\infty \tag{3.63}$$

uniformly in time. In this section we examine the existence of either exact or *long-lived* bright breather solutions of (3.2). The second class of solutions refers to spatially localized solutions of (3.2) remaining close to a time-periodic oscillation over long times.

We begin by noting the existence of trivial exact bright breather solutions of (3.2) for which particles do not interact, i.e. $(u_{n-1}(t) - u_n(t))_+^\alpha = 0$ for all t and n. This is equivalent to having

$$u_{n-1}(t) \leq u_n(t) \quad \forall\, t \in \mathbb{R},\, \forall n \in \mathbb{Z}, \tag{3.64}$$

$$\begin{aligned} \ddot{u}_n &= \kappa(v_n - u_n), \\ \rho\ddot{v}_n &= \kappa(u_n - v_n). \end{aligned} \tag{3.65}$$

The time-periodic solutions of (3.65) read

$$u_n(t) = \frac{\rho}{1+\rho}\, a_n \cos(\omega\, t + \phi_n) + b_n, \quad v_n(t) = -\frac{1}{1+\rho}\, a_n \cos(\omega\, t + \phi_n) + b_n, \tag{3.66}$$

where we can fix $a_n \geq 0$ and denote $\omega^2 = \kappa\,(1 + 1/\rho)$. Bright breather profiles are obtained for

$$\lim_{n\to\pm\infty} a_n = 0, \quad \lim_{n\to\pm\infty} b_n = c_\pm. \tag{3.67}$$

A solution of (3.2) is obtained if and only if constraint (3.64) is satisfied, which is equivalent to

$$b_n - b_{n-1} \geq \frac{\rho}{1+\rho}\,[\,a_n^2 + a_{n-1}^2 - 2a_n a_{n-1}\cos(\phi_n - \phi_{n-1})\,]^{1/2} \quad \forall\, n \in \mathbb{Z}. \tag{3.68}$$

For $(a_n)_{n\in\mathbb{Z}} \in \ell_1(\mathbb{Z})$, this is equivalent to assuming

$$b_n = d_n + \frac{\rho}{1+\rho}\sum_{k=-\infty}^{n}\,[\,a_k^2 + a_{k-1}^2 - 2a_k a_{k-1}\cos(\phi_k - \phi_{k-1})\,]^{1/2},$$

where $(d_n)_{n\in\mathbb{Z}}$ is a nondecreasing sequence converging as $n \to \pm\infty$. It is clear from this expression that $(b_n)_{n\in\mathbb{Z}}$ corresponds to a kink profile. Moreover, fixing $\phi_n - \phi_{n-1} = \pi$, we can simplify the above expression to obtain

$$b_n = d_n + \frac{\rho}{1+\rho}\,\big(a_n + 2\sum_{k=-\infty}^{n-1} a_k\big).$$

We now prove the following.

Theorem 3.4.1. *The trivial bright breather solutions defined by (3.66)-(3.67)-(3.68) are the only time-periodic bright breather solutions of (3.2).*

To prove Theorem 3.4.1, we follow the method of the proof of nonexistence of breathers in FPU chains with repulsive interactions given in [21]. Suppose (u_n, v_n) is a bright breather, i.e. a T-periodic solution of (3.2) satisfying (3.63). Adding the equations in (3.2), one can see that the bright breather solution must satisfy

$$\ddot{u}_n + \rho\ddot{v}_n = (u_{n-1} - u_n)_+^\alpha - (u_n - u_{n+1})_+^\alpha. \tag{3.69}$$

Integrating (3.69) over one period, we obtain

$$\bar{F}_{n+1} = \bar{F}_n, \qquad \bar{F}_n = \frac{1}{T}\int_0^T (u_{n-1}(t) - u_n(t))_+^\alpha dt. \tag{3.70}$$

Note that $\bar{F} := \bar{F}_n$ is independent of n and one can show that it vanishes. Indeed, by (3.63), we have

$$\lim_{n\to\pm\infty} ||u_n - u_{n-1}||_{L^\infty(0,T)} = 0. \tag{3.71}$$

Meanwhile,

$$|\bar{F}| = \frac{1}{T}\int_0^T (u_{n-1}(t) - u_n(t))_+^\alpha dt \leq ||u_{n-1}(t) - u_n(t)||_{L^\infty(0,T)}^\alpha \tag{3.72}$$

for all n. Taking the limit $n \to \pm\infty$ in (3.72) one obtains $\bar{F} = 0$. Consequently, for each n, we have

$$\int_0^T (u_{n-1}(t) - u_n(t))_+^\alpha dt = 0 \tag{3.73}$$

and since $F_n := (u_{n-1} - u_n)_+^\alpha$ is non-negative, continuous and T-periodic, we have $F_n = 0$ for all t and n. Thus (u_n, v_n) satisfies the linear system (3.65) and corresponds to a trivial bright breather solution. This completes the proof of Theorem 3.4.1.

In what follows we show that, although nontrivial time-periodic bright breathers do not exist for system (3.2), long-lived small-amplitude bright breather solutions can be found when ρ is large. This is due to the connection between (3.2) and the DpS equation (3.20) established in section 3.2.2. Equation (3.20) admits time-periodic solutions of the form

$$A_n(\tau) = \varepsilon\, a_n\, e^{i\,\omega_0\,|\varepsilon|^{\alpha-1}\,\tau}, \tag{3.74}$$

where $a = (a_n)_{n\in\mathbb{Z}}$ is a real sequence and $\varepsilon \in \mathbb{R}$ an arbitrary constant, if and only if a satisfies

$$a = -\delta^+[|\delta^- a|^{\alpha-1}\delta^- a]. \tag{3.75}$$

In particular, nontrivial solutions of (3.75) satisfying $\lim_{n\to\pm\infty} a_n = 0$ correspond to bright breather solutions of (3.20) given by (3.74). These solutions are doubly exponentially decaying, so that they belong to ℓ_p for all $p \in [1, \infty]$. They have been studied in a number of works (see [66] and references therein). The following existence theorem for spatially symmetric breathers has been proved in [66] using a reformulation of (3.75) as a two-dimensional mapping.

Theorem 3.4.2. *The stationary DpS equation (3.75) admits solutions a_n^i $(i = 1, 2)$ satisfying*

$$\lim_{n\to\pm\infty} a_n^i = 0,$$

$$(-1)^n\, a_n^i > 0, \quad |a_n^i| > |a_{n-1}^i| \quad \textit{for all } n \le 0,$$

$$\textit{and} \quad a_n^1 = a_{-n}^1, \quad a_n^2 = -a_{-n+1}^2, \quad \textit{for all } n \in \mathbb{Z}.$$

Furthermore, for all $\bar{q} \in (0,1)$*, there exists* $n_0 \in \mathbb{N}$ *such that the above-mentioned solutions* a_n^i *satisfy, for* $i = 1, 2$*:*

$$\forall n \geq n_0, \quad |a_n^i| \leq \bar{q}^{1+\alpha^{n-n_0}}.$$

Considering the bright breather solutions of (3.20) given by (3.74) with $a = a^i$, $\varepsilon = 1$, and applying Theorem 3.2.1, one obtains stable exact solutions of equations (3.2), close to the bright breathers, over the corresponding time scales. This yields the following result formulated for $\kappa = 1$.

Theorem 3.4.3. *Fix constants* $C_{\mathrm{r}}, C_{\mathrm{i}}, T > 0$*. Consider a solution* $a^i = (a_n^i)_{n\in\mathbb{Z}}$ *(*$i = 1, 2$*) of the stationary DpS equation (3.75) described in Theorem 3.4.2. There exist* $\varepsilon_T, C_T > 0$ *such that for all* $\varepsilon \in (0, \varepsilon_T]$ *and for* $\rho^{-1} \leq C_{\mathrm{r}}\, \varepsilon^{2(\alpha-1)}$*, for all initial condition of (3.2) in* ℓ^4_p *satisfying*

$$\|u(0) - 2\varepsilon\, a^i\|_p + \|\dot{u}(0)\|_p + \|v(0)\|_p \leq C_{\mathrm{i}}\varepsilon^{\alpha}, \quad \|\dot{v}(0)\|_p \leq C_{\mathrm{i}}\varepsilon^{2\alpha-1}, \tag{3.76}$$

the solution to equation (3.2) is defined at least for $t \in [0, T\varepsilon^{1-\alpha}]$ *and satisfies*

$$\|u(t) - 2\varepsilon\, a^i\, \cos(\Omega_b\, t)\|_p + \|\dot{u}(t) + 2\varepsilon\, a^i\, \sin(\Omega_b\, t)\|_p \leq C_T\varepsilon^{\alpha}, \text{ for all } t \in [0, T\varepsilon^{1-\alpha}], \tag{3.77}$$

with $\Omega_b = 1 + \omega_0\, \varepsilon^{\alpha-1}$*,* ω_0 *defined in (3.21) and*

$$\|v(t)\|_p \leq C_T\varepsilon^{\alpha}, \quad \|\dot{v}(t)\|_p \leq C_T\varepsilon^{2\alpha-1}, \text{ for all } t \in [0, T\varepsilon^{1-\alpha}]. \tag{3.78}$$

It is important to stress the differences between the long-lived bright breather solutions provided by Theorem 3.4.3 and the trivial bright breathers analyzed at the beginning of this section. The oscillations described in Theorem 3.4.3 are nontrivial in the sense that Hertzian interactions do not vanish identically. In addition, they are truly localized (for $p < \infty$) whereas the trivial exact breathers are superposed on a nonvanishing kink component b_n. Moreover, the (approximate) frequency Ω_b of long-lived bright breathers satisfies $0 < \Omega_b - 1 = O(\varepsilon^{\alpha-1})$ for breathers with amplitude $O(\varepsilon)$. For trivial exact bright breathers, the frequency ω is independent of amplitude and satisfies $0 < \omega - 1 = O(1/\rho)$ when ρ is large. Under the assumptions of Theorem 3.4.3, we have $1/\rho = O(\varepsilon^{2(\alpha-1)})$ and thus $\Omega_b > \omega$ for ε small enough.

We now investigate the behavior of long-lived bright breathers numerically. Fixing $T = 2\pi/\omega_0 = 19.4158$, $C_r = C_i = 1$ and choosing $\varepsilon = 0.01$, we consider a locally resonant chain of $N = 40$ masses with the mass ratio $\rho = 1000$ so that the inequality $\rho^{-1} \leq C_r \varepsilon^{2(\alpha-1)}$ in Theorem 3.4.3 is satisfied. We then integrate the system (3.2) over a long time interval $[0, 80\,T]$, starting with initial conditions

$$u(0) = 2\varepsilon a^i, \quad v(0) = 0, \quad \dot{u}(0) = \dot{v}(0) = 0 \tag{3.79}$$

where a^i is the numerical solution of (3.75) obtained using the method in [21]. The numerical simulation yields spatially localized solutions of (3.2) that stay close to the time-periodic oscillation

$$\widetilde{u}(t) = 2\varepsilon a^i \cos(\Omega_b t), \quad \dot{\widetilde{u}}(t) = -2\varepsilon a^i \sin(\Omega_b t), \quad \widetilde{v}(t) = \dot{\widetilde{v}}(t) \equiv 0 \tag{3.80}$$

with $i = 2$ over the time interval $[0, T\varepsilon^{1-\alpha}] = [0, 194.158]$, as can be seen in the inset of the right panel of Fig 3.7. Note that the comparison is made at times correspond to multiples of $T_b = 2\pi/\Omega_b = 6.0862$. To measure the relative difference of the numerical solution of (3.2) and the time-periodic oscillations (3.80), we define the rescaled ℓ_1-norms as follows

$$E_u(t) = \frac{||u(t) - \widetilde{u}(t)||_1}{\varepsilon^\alpha}, \quad E_{\dot{u}}(t) = \frac{||\dot{u}(t) - \dot{\widetilde{u}}(t)||_1}{\varepsilon^\alpha} \tag{3.81}$$

and

$$E_v(t) = \frac{||v(t) - \widetilde{v}(t)||_1}{\varepsilon^\alpha}, \quad E_{\dot{v}}(t) = \frac{||\dot{v}(t) - \dot{\widetilde{v}}(t)||_1}{\varepsilon^{2\alpha-1}}. \tag{3.82}$$

The fact that those rescaled norms remains small and bounded over time interval $[0, T\varepsilon^{1-\alpha}]$ is consistent with the result of Theorem 3.4.3 and confirms the existence of the long-lived bright breathers. However, at larger time, part of the energy is radiated away from the vicinity of the initially excited sites. As a result, we observe the breakdown of the localized structure for a long-time ($t \gg T\varepsilon^{1-\alpha}$) evolution, and the solution profile spreads out and eventually approaches to a kink-type structure shown by circles in the left panel of Fig 3.7. This is associated with the growing magnitude of v_n during the simulation.

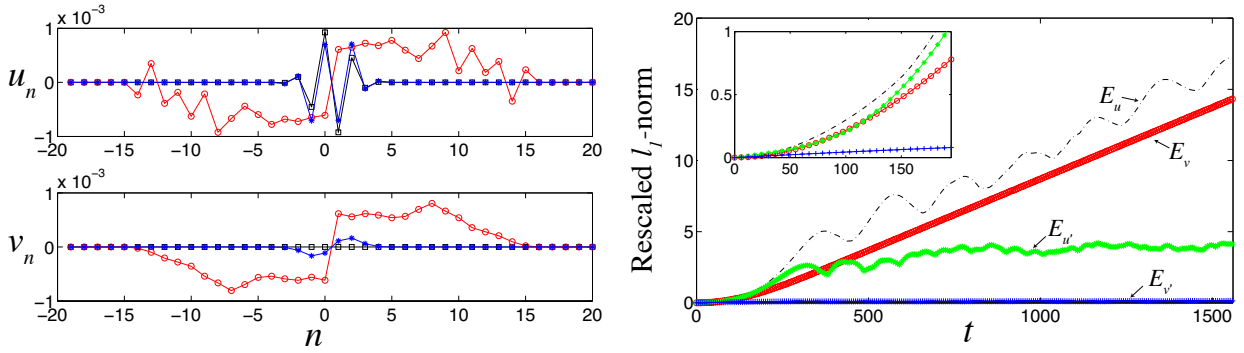

Figure 3.7: Left panels: snapshot of numerical solution of (3.2) at $t = 30\,T_b < 10\,T$ (blue stars) and $t = 80\,T$ (red circles), respectively, starting with initial conditions (3.79) with $i = 2$ (black squares). Right panel: time evolution of the rescaled ℓ_1-norms defined in (3.81) and (3.82), where $E_u(t)$ is represented by connected dots (black curve), $E_{\dot{u}}(t)$ by connected stars (green curve), $E_v(t)$ by connected circles (red curve) and $E_{\dot{v}}(t)$ by connected pluses (blue curve). The inset in the right plot shows time evolution of the same ℓ_1-norms when $t \leq T\varepsilon^{1-\alpha}$.

3.5 DARK BREATHERS

3.5.1 Approximate dark breather solutions

We now turn to dark breather solutions, which, as we will see, are fundamentally different from the waveforms considered in the previous section and are not excluded by the results of Theorem 3.4.1. To construct approximate dark breather solutions, we start by considering *standing wave* solutions of the generalized DpS equations (3.17)-(3.18) in the form

$$\delta^- A_n(\tau) = \delta^- a_n e^{i(\Omega\tau+\phi)} \quad (a_n \in \mathbb{R}), \quad \delta^- B_n(\tau) = \delta^- b_n, \tag{3.83}$$

where a_n and b_n are time-independent. Introducing $\omega_b = \omega + \Omega\varepsilon^{\alpha-1}$, we find that the first-order approximate solution of (3.2) reads

$$\begin{aligned} u_n^{sw}(t) &= \varepsilon b_n + 2\kappa\varepsilon a_n \cos(\omega_b t + \phi), \\ v_n^{sw}(t) &= \varepsilon b_n - \frac{2\kappa}{\rho}\varepsilon a_n \cos(\omega_b t + \phi). \end{aligned} \tag{3.84}$$

Substituting (3.83) in the generalized DpS equations (3.17)-(3.18) we obtain

$$\begin{aligned} -\mu a_n &= h_\alpha(\delta^- b_{n+1}, |\delta^- a_{n+1}|)\delta^- a_{n+1} - h_\alpha(\delta^- b_n, |\delta^- a_n|)\delta^- a_n \\ \delta^+ g_\alpha(\delta^- b_n, |\delta^- a_n|) &= 0, \end{aligned} \tag{3.85}$$

where $\mu = 2\kappa\omega^3\Omega = 2\kappa\omega^3(\omega_b - \omega)\varepsilon^{1-\alpha}$.

Following the approach in [20], for $\mu \neq 0$ one can further show that $\widetilde{a}_n = |\mu|^{\frac{1}{1-\alpha}} a_n$, $\widetilde{b}_n = |\mu|^{\frac{1}{1-\alpha}} b_n$ satisfy the renormalized equation

$$\begin{aligned} -\operatorname{sign}(\mu)\widetilde{a}_n &= h_\alpha(\delta^-\widetilde{b}_{n+1}, |\delta^-\widetilde{a}_{n+1}|)\delta^-\widetilde{a}_{n+1} - h_\alpha(\delta^-\widetilde{b}_n, |\delta^-\widetilde{a}_n|)\delta^-\widetilde{a}_n \\ \delta^+ g_\alpha(\delta^-\widetilde{b}_n, |\delta^-\widetilde{a}_n|) &= 0. \end{aligned} \tag{3.86}$$

where $\operatorname{sign}(\mu) = 1$ for $\mu > 0$ and $\operatorname{sign}(\mu) = -1$ for $\mu < 0$. For simplicity we drop the tilde in (3.86) in what follows. Numerical results suggest that a nontrivial solution for $\{\delta^- a_n\}$ can be found if and only if $\mu > 0$. Thus it suffices to consider the case $\mu = 1$. It is convenient to rewrite (3.86) in terms of $\delta^- a_n$ and $\delta^- b_n$ by subtracting from the first equation in (3.86) the same equation at $n-1$:

$$\begin{aligned} &-\delta^- a_n = h_\alpha(\delta^- b_{n+1}, |\delta^- a_{n+1}|)\delta^- a_{n+1} - 2h_\alpha(\delta^- b_n, |\delta^- a_n|)\delta^- a_n + h_\alpha(\delta^- b_{n-1}, |\delta^- a_{n-1}|)\delta^- a_{n-1} \\ &g_\alpha(\delta^- b_{n+1}, |\delta^- a_{n+1}|) = g_\alpha(\delta^- b_n, |\delta^- a_n|). \end{aligned} \tag{3.87}$$

We now use Newton's iteration to solve (3.87) numerically for $\delta^- a_n$, $\delta^- b_n$, $n = -N, \ldots, N$, with periodic boundary conditions ($\delta^- a_{-N-1} = \delta^- a_N$ and $\delta^- a_{N+1} = \delta^- a_{-N}$). Note that the associated Jacobian matrix is singular due to the structure of second equation in (3.87), and therefore an additional constraint is necessary. It is sufficient to fix $\delta^- b_{-N} = c$, where c is a constant. Since we are looking for dark breathers, it is natural to consider initial values of $\delta^- a_n$ in the form

$$\delta^- a_n^0 = (-1)^n \tanh(n - n_0) \tag{3.88}$$

where n_0 is an arbitrary constant corresponding to spatial translation. One can then use the second equation in (3.87) to solve for initial guess of $\delta^- b_n^0$, $n = -N+1, ..., N$. A standard Newton's iteration procedure of the system (3.87) with $4N+1$ variables $\delta^- b_{-N+1}, \ldots, \delta^- b_N$, $\delta^- a_{-N}, \ldots, \delta^- a_N$ is then performed with the tolerance of 10^{-8}. Setting $n_0 = 0$ in (3.88)

results in a site-centered solution shown in the left panel of Fig. 3.8, whereas the bond-centered solution corresponds to $n_0 = 1/2$ shown the right panel. Typical breather waveforms of both bright [25] and dark [18] type come in these two broad families [27].

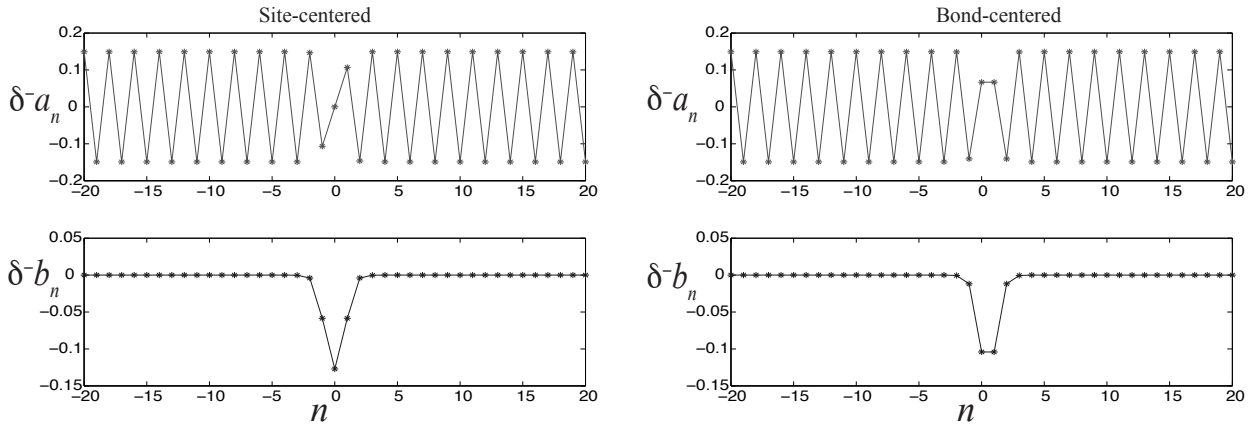

Figure 3.8: Left panel: A site-centered solution of (3.87) with $\delta^- b_{-N} = c = 0$. Right panel: bond-centered solution.

Once the Newton's iteration converges to a fixed point $\{(\delta^- a_n^*, \delta^- b_n^*)\}$, we can compute the first-order approximate solution of (3.3) given by

$$\begin{aligned} x_n^{sw}(t) &= |\bar{\mu}|^{\frac{1}{\alpha-1}}\{\delta^- b_n^* + 2\kappa\delta^- a_n^* \cos(\omega_b t + \phi)\}, \\ y_n^{sw}(t) &= |\bar{\mu}|^{\frac{1}{\alpha-1}}\{\delta^- b_n^* - \frac{2\kappa}{\rho}\delta^- a_n^* \cos(\omega_b t + \phi)\}, \end{aligned} \tag{3.89}$$

where $\bar{\mu} = 2\kappa\omega^3(\omega_b - \omega)$.

3.5.2 Numerically exact dark breathers

Having constructed the initial seed (3.89), we can compute the numerically exact dark breather solution of system (3.3) with periodic boundary conditions. Let $x(t)$, $y(t)$, $\dot{x}(t)$ and $\dot{y}(t)$ denote the row vectors with component $x_n(t)$, $y_n(t)$, $\dot{x}_n(t)$ and $\dot{y}_n(t)$, respectively. Let $Z(t) := (x(t), y(t))$. We seek time-periodic solutions $(Z(t), \dot{Z}(t))$ of Hamiltonian system (3.3) satisfying the initial conditions $(Z(0), \dot{Z}(0))$. For a fixed period of the dark breather solution given by $T_b = 2\pi/\omega_b$, where ω_b is the breather frequency, the problem is equivalent to finding the fixed points of the corresponding Poincaré map $P_{T_b}[(Z(0), \dot{Z}(0))^T] = (Z(T_b), \dot{Z}(T_b))^T$.

Since the system (3.3) has the time-reversal symmetry, we can further restrict the solution space by setting $\dot{Z}(0) \equiv 0$.

We use a Newton-type algorithm (see, for example, Algorithm 2 in [67]) to compute the fixed point. More precisely, let $\Delta Z(0)$ be the small increment of the initial data that needs to be determined. It is then sufficient to minimize $||P_{T_b}[(Z(0)+\Delta Z(0),0)^T]-(Z(0)+\Delta Z(0),0)^T||$ at each iteration step. Notice that $P_{T_b}[(W(0),0)^T]$ can be approximated by $P_{T_b}[(Z(0),0)^T]+M(T_b)(\Delta Z(0),0)^T$ for sufficiently small $\Delta Z(0)$. Here $M(t)$ is the associated monodromy matrix of the variational equations satisfying

$$\frac{d}{dt}M(t) = \mathcal{J}(Z(t),\dot{Z}(t))M(t), \quad M(0) = I, \tag{3.90}$$

where $\mathcal{J}(Z(t),\dot{Z}(t))$ is the Jacobian matrix of the nonlinear system (3.3) at $(Z(t),\dot{Z}(t))$, and I is the identity matrix. The Jacobian for the Newton's iteration is then given by $I-M(T_b)$ and it is singular since it can be shown that $M(T_b)$ has eigenvalue equal to 1. To remove the singularity, we impose the additional constraint that the time average of $x_1(t)+\Delta x_1(t)$, the first component $Z(t)+\Delta Z(t)$, is fixed to be (approximately) zero. Observing that $(Z(t)+\Delta Z(t),\dot{Z}(t)+\Delta\dot{Z}(t))^T \approx (Z(t),\dot{Z}(t))^T + M(t)(Z(0),0)^T$, we obtain

$$\frac{1}{T_b}\int_0^{T_b} x_1(t)dt + \frac{1}{T_b}\int_0^{T_b} M_1(t)\cdot\Delta Z(0)dt = 0. \tag{3.91}$$

where $M_1(t)$ is the first row of $M(t)$.

In the results discussed below we set $\kappa = 1$. To characterize the solution, we define the vertical centers of the solution for x and y components [18],

$$C_x := \frac{\sup_{t\in[0,T_b]} x_1(t) + \inf_{t\in[0,T_b]} x_1(t)}{2}, \quad C_y := \frac{\sup_{t\in[0,T_b]} y_1(t) + \inf_{t\in[0,T_b]} y_1(t)}{2} \tag{3.92}$$

and the amplitudes of the breather,

$$K_x := \frac{\sup_{t\in[0,T_b]} x_1(t) - \inf_{t\in[0,T_b]} x_1(t)}{2}, \quad K_y := \frac{\sup_{t\in[0,T_b]} y_1(t) - \inf_{t\in[0,T_b]} y_1(t)}{2}. \tag{3.93}$$

Note that the vertical center C_x is approximately zero due to the constraint (3.91). However, one can fix any other value of C_x by replacing zero in the right hand side of (3.91) by C_x. To

further investigate the long-term behavior of the dark breather solution, we introduce the relative error

$$E_b(t) = ||Z(mT_b) - Z(0)||_\infty / ||Z(0)||_\infty \tag{3.94}$$

where $m = \lfloor t/T_b \rfloor$ and $Z(mT_b) = (x(mT_b), y(mT_b))$ represents the strain profile after integrating (3.3) over m multiple of time periods, starting with the static dark breather $Z(0)$ as the initial condition.

We first consider the mass ratio $\rho = 1/3$, so that the linear frequency is $\omega = 2$. We choose a value of ω_b that is slightly greater than this value but close enough to it in order to obtain a good initial seed with a small amplitude. Once the Newton-type solver converges to a numerically exact dark breather solution, we use the method of continuation to obtain an entire family of dark breathers that corresponds to different values of ω_b. Sample profiles of both bond-centered and site-centered dark breather solutions with $\omega_b = 2.05$ along with the DpS approximate solutions (3.89) are shown in Fig. 3.9. The amplitudes K_x and K_y increase with ω_b, and the solution approaches zero as $\omega_b \to \omega$.

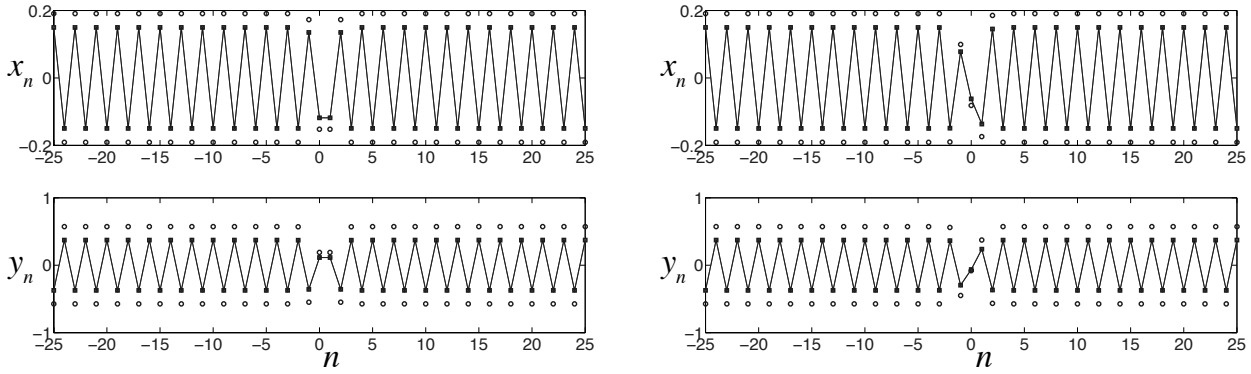

Figure 3.9: Left panel: a bond-centered solution of dark breather solution (connected stars) with frequency $\omega_b = 2.05$. Connected squares represent strain profile after integration over T_b and circles represent the DpS approximate solution from the ansatz (3.89). Right panel: site-centered solution. The relative errors $E_b(T_b)$ of both site-centered and bond-centered solutions are less than 4.5×10^{-9}. Here $\kappa = 1$ and $\rho = 1/3$.

3.6 LINEAR STABILITY ANALYSIS AND BIFURCATION

3.6.1 Floquet analysis

The linear stability of each obtained dark breather solution is examined via a standard Floquet analysis. The eigenvalues (Floquet multipliers) of the associated monodromy matrix $M(T_b)$ determine the linear stability of the breather solution. The moduli of Floquet multipliers for the site-centered and bond-centered solutions of various frequencies are shown in Fig. 3.10, along with the numerically computed Floquet spectrum that corresponds to the sample breather profile at $\omega_b = 2.09$. If any of these Floquet multipliers λ_i satisfies $|\lambda_i| > 1$, the corresponding breather is linearly unstable. We observed two types of instabilities in this Hamiltonian system. The first one is the *real instability*, which corresponds to a real Floquet multiplier with magnitude greater than one; an example is shown in the right top plot of Fig. 3.10 for the bond-centered dark breather with $\omega_b = 2.09$. The second type is the *oscillatory instability*, which corresponds to a quartet of Floquet multipliers outside the unit circle with non-zero imaginary parts (see the right bottom plot of Fig. 3.10 for the site-centered dark breather with $\omega_b = 2.09$).

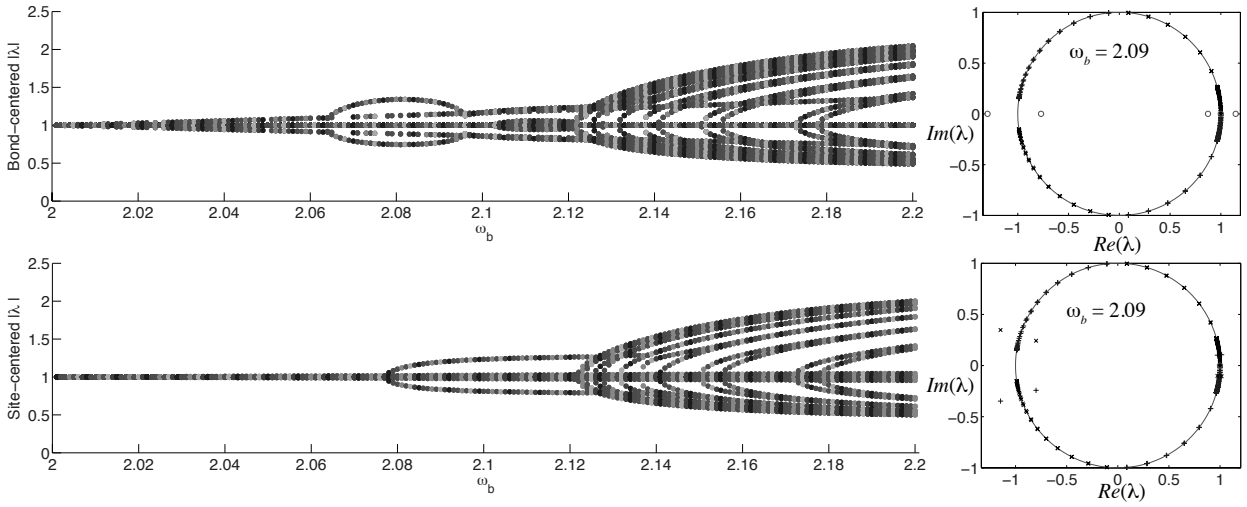

Figure 3.10: Left plots: moduli of the Floquet multipliers versus frequency ω_b for the bond-centered (top) and site-centered (bottom) breathers. The Floquet multipliers for $\omega_b = 2.09$ in the complex plane are shown in the respective plots on the right. Here $\kappa = 1$ and $\rho = 1/3$.

Numerical results reveal that the site-centered dark breathers appear to exhibit only

oscillatory instability. These marginally unstable modes emerge at the beginning of the continuation procedure but remain weak until ω_b reaches $\omega_b \approx 2.078$. As shown in the right plot of Fig. 3.11, the relative error $E_b(1200)$ stays below 7×10^{-7} when $\omega_b \leq 2.077$ but increases dramatically afterwards. The results are consistent with the Floquet spectrum shown in the left plot of Fig. 3.11. In fact, beyond the critical point of $\omega_b \approx 2.078$, we observe the emergence of a new and stronger oscillatory instability mode that corresponds to two pairs of Floquet multipliers distributed symmetrically outside the unit circle around -1 (see also the right bottom plot of Fig. 3.10 for $\omega_b = 2.09$). Representative space-time evolution diagrams of site-centered dark breather solutions are shown in Fig. 3.12, which suggests that the site-centered dark breather solutions with frequency close to the linear frequency ω are long-lived and have marginal oscillatory instability, below the pertinent critical point. However, the oscillatory instability becomes more and more significant as ω_b increases, leading to the breakdown of the dark breather structure of the solution. In fact, beyond the critical point, the breakup of the site-centered breather appears to be accompanied in Fig. 3.12 by a dramatic evolution, whereby the configuration is completely destroyed and a form of lattice dynamical turbulence ensues. This phenomenon is reminiscent of traveling wave instabilities observed in [68] for Hertzian chains and may be worth further study, which, however, is outside the scope of this dissertation.

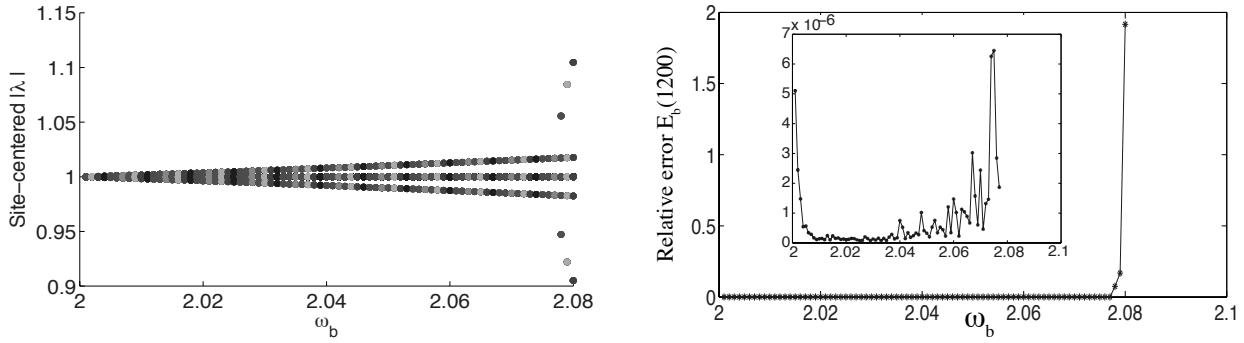

Figure 3.11: Left plot: moduli of the Floquet multipliers of the site-centered breathers for frequency $\omega_b \leq 2.08$. Right plot: the relative error $E_b(t)$ versus frequency at $t = 1200$. Inset shows the relative error for frequencies less than $\omega_b \leq 2.077$. Here $\kappa = 1$ and $\rho = 1/3$.

In contrast to the site-centered solutions, the bond-centered ones exhibit only real instability at the early stage of the continuation when the breather frequency ω_b is greater than

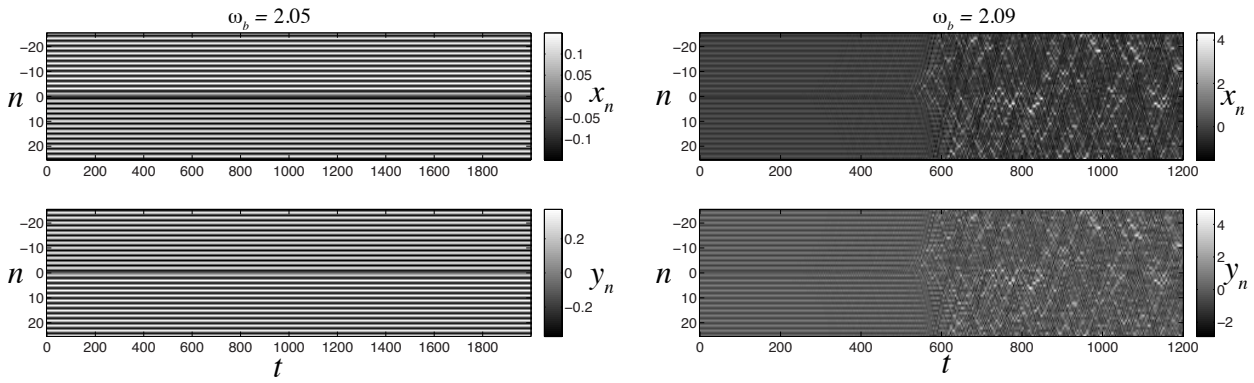

Figure 3.12: Left panel: contour plot of the time evolution of the site-centered solution for $\omega_b = 2.05$. The color bar corresponds to the magnitude of the strain x_n (top) and y_n (bottom). Right panel: same computation as in left panel but for $\omega_b = 2.09$. Here $\kappa = 1$ and $\rho = 1/3$.

but close to ω. At those frequencies, the magnitude of the Floquet multipliers corresponding to the real instability of bond-centered breathers is larger than the moduli of the multipliers describing the oscillatory instability of the site-centered ones, resulting in not only shorter lifetime of the bond-centered solutions, but also setting the dark breather state in motion. A representative space-time evolution diagram for bond-centered dark breather solution of frequency $\omega_b = 2.05$ is shown in the left panel of Fig. 3.13. In the right panel of Fig. 3.13 the manifestation of real instability of the same solution is shown, where the perturbation of the dark breather solution along the direction associated with the unstable mode that corresponds to a real Floquet multiplier is used as the initial condition for the integration. One can see that the instability results in a dark breather moving with constant velocity after some initial transient time in the left panel, while the pertinent motion is initiated essentially immediately by the perturbation induced in the right panel. However, as ω_b is increased the same phenomenology (dismantling of the breather and chaotic evolution) is also taking place for the bond-centered breathers, as shown in Fig. 3.14.

3.6.2 Period-doubling bifurcation

The large arc seen in the middle of the Floquet multiplier diagram of the bond-centered breather solutions (the top left plot in Fig. 3.10) corresponds to the *period-doubling bifurca-*

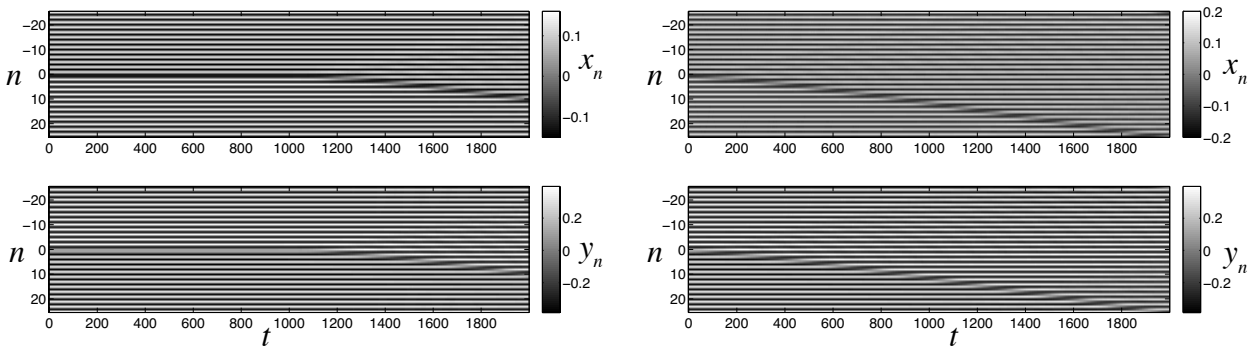

Figure 3.13: Left panel: contour plot of the time evolution of the bond-centered solution for $\omega_b = 2.05$. The color bar corresponds to the magnitude of the strain x_n (top) and y_n (bottom). Right panel: same simulation as in the left panel but with the perturbed dark breather as the initial condition. Here $\kappa = 1$ and $\rho = 1/3$.

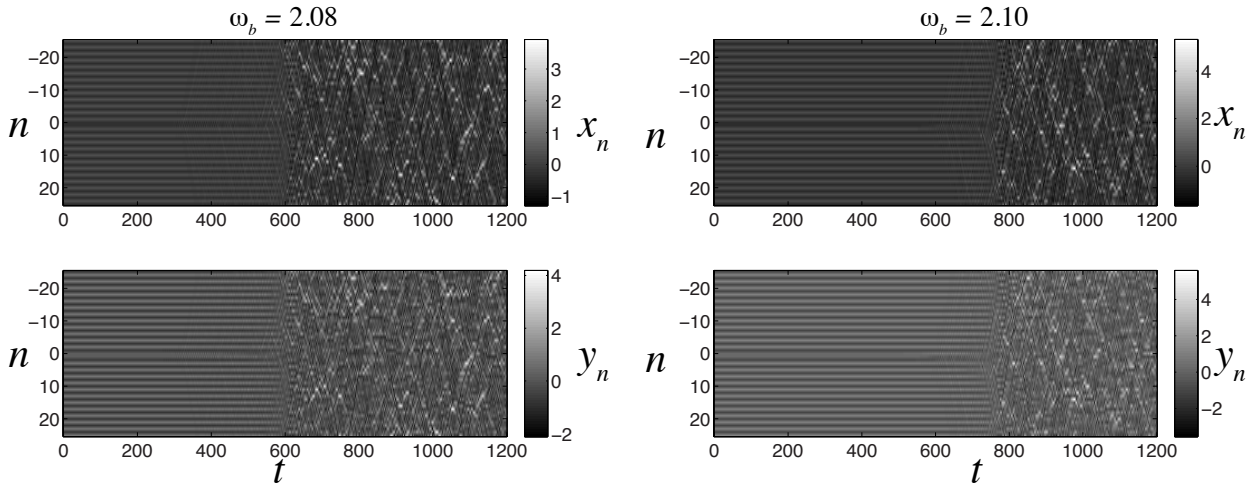

Figure 3.14: Left panel: contour plot of the time evolution of the bond-centered solution for $\omega_b = 2.08$. The color bar corresponds to the magnitude of the strain x_n (top) and y_n (bottom). Right panel: same simulation as in the left panel but at frequency $\omega_b = 2.10$. Here $\kappa = 1$ and $\rho = 1/3$.

tion. As the frequency approaches $\omega_b \approx 2.063$, two complex conjugate eigenvalues collide on the real axis at -1. Two real eigenvalues then form and move in opposite directions as ω_b increases. After the difference between the real eigenvalues reaches a maximum value, they start moving toward each other and collide at $\omega_b \approx 2.096$. Breathers with double the period (half the frequency) of the ones on the main branch exist between these two frequencies.

To explore the numerically exact period-doubling orbits, we constructed an initial seed by slightly perturbing the dark breather solution at the bifurcation point along the direction of eigenvector associated with the eigenvalue -1. As shown in Fig. 3.15, the eigenvector is spatially localized at the middle of the chain. As a consequence, the initial seed only differs from the previous dark breather solution in the middle part of the chain. Sample

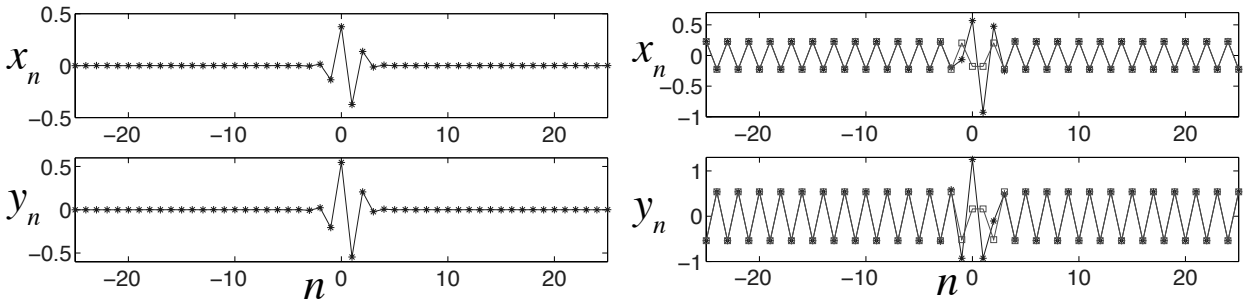

Figure 3.15: Left panel: the eigenvector associated with the eigenvalue -1. Right panel: numerically exact dark breather solution of frequency $\omega_b = 1.032$ (connected squares) and initial seed (connected stars) after perturbing numerically exact dark breather solution of frequency $\omega_b = 2.063$.

profiles of period-doubling dark breather solution at $\omega_b = 1.032$ are shown in the top of Fig. 3.16. To check that these solutions differ from the main branch, we integrated the solution for both the full period $T_b = 2\pi/\omega_b$ and its half $T_b/2$ and verified that the period of the obtained new solution is doubled compared with the previously obtained dark breathers. The continuation method is used to obtain all the period-doubling dark breather solutions for different frequencies. Note that the continuation stops at $\omega_b \approx 1.051$ and also cannot proceed for ω_b below 1.032, which agrees with the (doubled) frequency range of the large arc in the top left plot of Fig. 3.10. All of these solutions exhibit both real and oscillatory instabilities (see the bottom plots of Fig. 3.16).

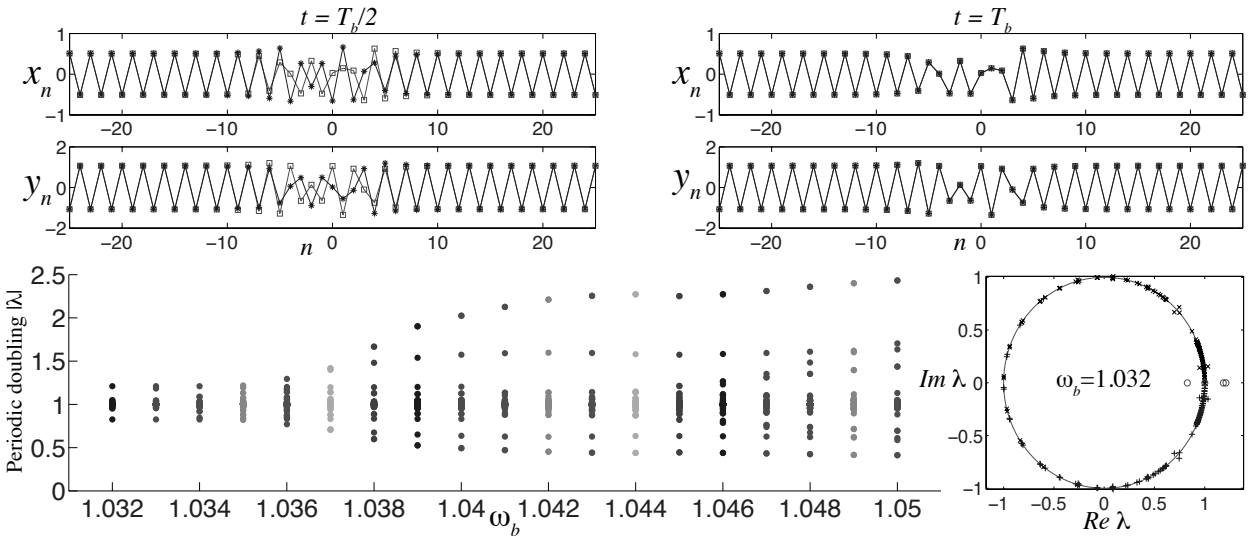

Figure 3.16: Top panel: comparison of the numerically exact double-period solution at $\omega_b = 1.032$ (connected squares) and the result of its integration (connected stars) at $t = T_b/2$ and $t = T_b$. Bottom left: moduli of Floquet multipliers versus frequency ω_b for the period-doubling solutions. The Floquet multipliers for $\omega_b = 1.032$ in the complex plane are shown in the right plot. Here $\kappa = 1$ and $\rho = 1/3$.

3.6.3 Effect of mass ratio

We now investigate the effect of mass ratio on stability of the dark breathers by considering different values of ρ. Recall that the linear frequency $\omega = \sqrt{\kappa + \kappa/\rho}$ decreases and approaches $\sqrt{\kappa}$ as ρ increases. In what follows, we start the continuation at frequency $\omega_b = \omega + 0.01$ to make sure that the amplitude of initial seed (3.89) is small. We first test the case when $\rho = 3$ with linear frequency given by $\omega = 1.1547$. Sample profiles of bond-centered and site-centered dark breather solutions at the frequency $\omega_b = \omega + 0.1 = 1.2547$ and their space-time evolution diagrams are shown in Fig. 3.17. We observe the bond-centered solution starts to move in form of a traveling dark breather after the integration for a sufficiently long time, while the site-centered solution persists for a longer time in the simulation and hence can be considered to be long-lived. The dynamic behavior of both solutions is consistent with their numerically computed Floquet spectrum shown in the right of Fig. 3.18. Moreover, the diagrams of Floquet multipliers' moduli in the right panel of Fig. 3.18 suggest that the bond-centered solutions exhibit only real instability for a wide range of frequencies

$[\omega + 0.001, \omega + 0.2]$, while the site-centered dark breathers have just marginal oscillatory instability.

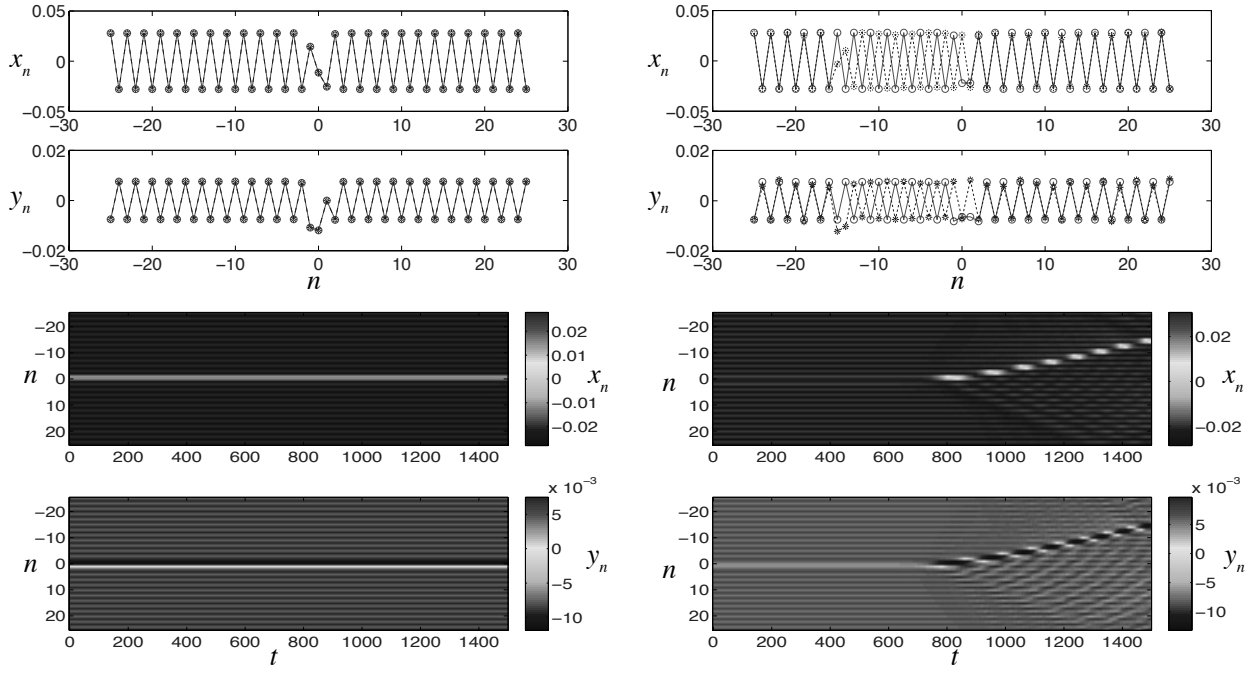

Figure 3.17: Top panel: sample profiles (circles) of site-centered (left) and bond-centered (right) dark breathers at the frequency $\omega_b = 1.2547$. Stars connected by dashed lines represent strain profiles after the integration over $299T_b \approx 1500$. Note that the site-centered solution has relative error $E_b(1500) = 9.21 \times 10^{-5}$. Bottom panel: space-time evolution diagrams for site-centered (left) and bond-centered (right) solutions. Here $\kappa = 1$ and $\rho = 3$.

Next, we repeat the simulation with $\rho = 10$ and $\omega = 1.0488$. Note that the amplitude of dark breather solution at frequency $\omega_b = \omega + 0.01$ is close to 1.6×10^{-4}. As shown in Fig. 3.19, the pattern of Floquet multipliers moduli is very similar to the $\rho = 3$ case for breather frequencies close to ω. However, as ω_b becomes larger, we observed significant oscillatory instability of both the bond-centered and site-centered solutions. Note that the distribution of Floquet multipliers at large mass ratios (for example, $\rho = 3$, 10) is completely different than that at smaller ones (such as $\rho = 1/3$), given the same magnitude of frequency difference $\omega_b - \omega$.

We now fix the breather frequency ω_b and perform the continuation in the mass ratio ρ. The results of numerical continuation are shown in Fig. 3.20. At a given breather frequency, the real instability is only exhibited by solutions of the bond-centered type, and its signif-

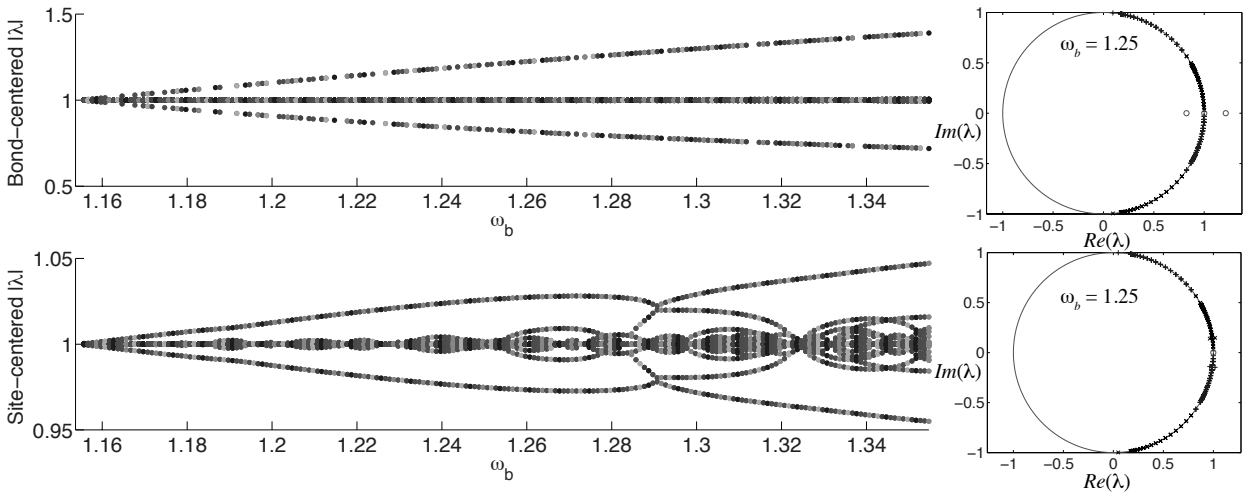

Figure 3.18: Left panel: moduli of Floquet multipliers versus frequency ω_b for the bond-centered (top) and site-centered (bottom) types. Right panel: Floquet multipliers of dark breather solutions of frequency $\omega_b = 1.2547$ in the complex plane. Here $\kappa = 1$ and $\rho = 3$.

icance is gradually increasing as mass ratio becomes larger. In contrast, the site-centered solutions have marginal oscillatory instability and persist for a long time. Moreover, the lifetime of those solutions decreases as the mass ratio increases. At a larger frequency like $\omega_b = 2.05$ and small mass ratio, the emergence of many unstable quartets suggests that both bond-centered and site-centered solutions share strong modulational instabilty of the background, which leads to a chaotic evolution of both solutions after a short time of integration.

3.7 CONCLUDING REMARKS

In this chapter, we studied nonlinear waves in a resonant granular material modeled by a Hertzian chain of identical particles with a secondary mass attached to each bead in the chain by a linear spring. Following the approach developed in [20] for a limiting case of the present model, we derived generalized modulation equations of DpS type. We showed that for suitable initial data and large enough mass ratio, these equations reduce to the DpS

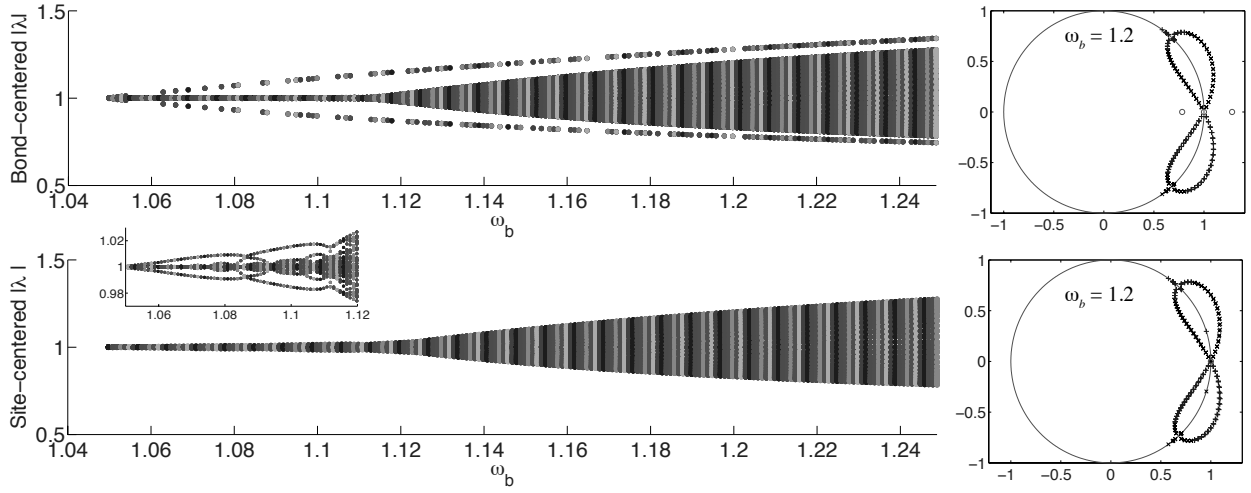

Figure 3.19: Left panel: moduli of Floquet multipliers versus frequency ω_b for the bond-centered (top) and site-centered (bottom) types. Right panel: Floquet spectrum of dark breather solutions of frequency $\omega_b = 1.20$ in the complex plane. Inset represents the zoom-in of moduli of Floquet multipliers for the site-centered solution at frequency $\omega_b \in [w + 0.001, w + 0.07]$. Here $\kappa = 1$ and $\rho = 10$.

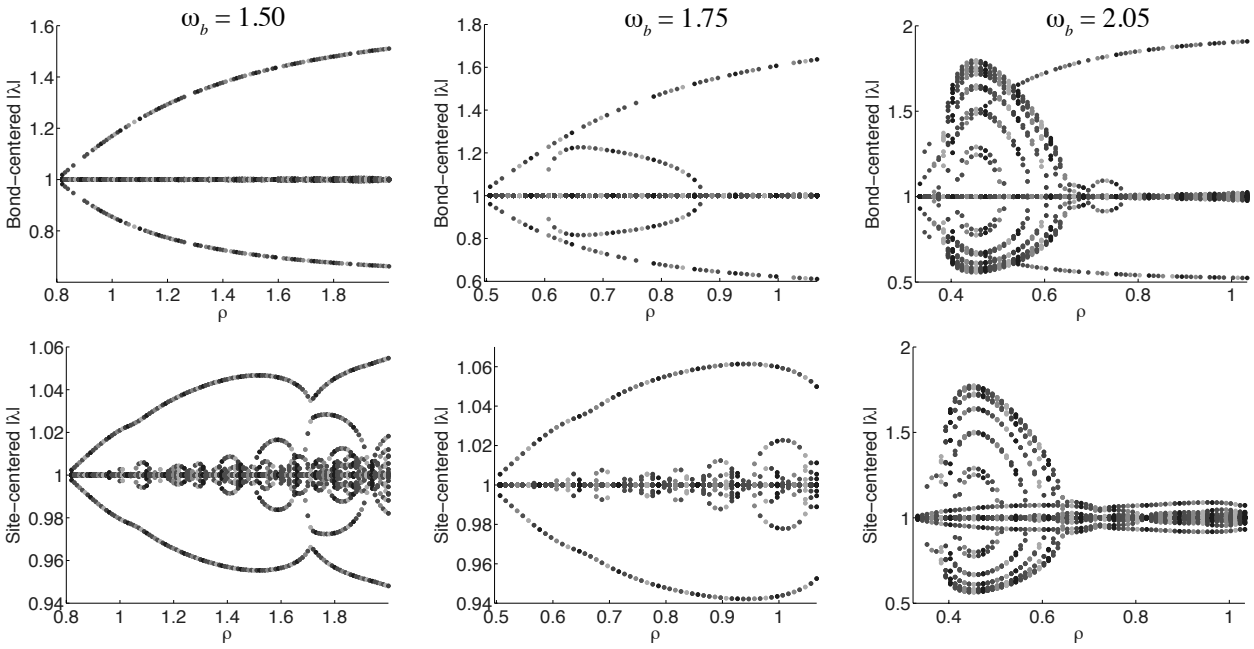

Figure 3.20: Moduli of Floquet multipliers versus mass ratio ρ for the bond-centered (top) and site-centered (bottom) type. The tested frequencies of dark breather are $\omega_b = 1.50, 1.75$ and 2.05. Here $\kappa = 1$.

equation derived in [20] and rigorously justified the equation in this limit on the long time scales. We then used the DpS equations to investigate the time-periodic traveling wave of the system at finite mass ratio. We showed numerically that these equations can successfully capture the dynamics of small-amplitude periodic traveling waves.

Turning our attention to the breather-type solutions, we proved non-existence of nontrivial bright breathers at finite mass ratio. However, we also showed that at sufficiently large mass ratio and suitable initial data, the problem has long-lived bright breather solutions.

The generalized DpS equations were also used to construct well-prepared initial conditions for the numerical computation of dark breather solutions. A continuation procedure based on a Newton-type fixed point method and initiated by the approximate dark breather solutions obtained from the DpS equations was utilized to compute numerically exact dark breathers for a wide range of frequencies and at different mass ratios. The stability and the bifurcation structure of the numerically exact dark breathers of both bond-centered and site-centered types were examined. Our numerical results strongly suggest that the bond-centered solutions exhibit real instability that may give rise to steady propagation of a dark breather after large enough time. In addition, period-doubling bifurcations of these solutions were identified at small mass ratios. The site-centered solutions, in contrast to the bond-centered ones, appeared to exhibit only oscillatory instability, which is much weaker than the real instability of the bond-centered breathers for a range of breather frequencies that are close enough to the natural frequency of the system, i.e., the frequency of out-of-phase motion within each unit cell of the chain involving the particle and the secondary mass. As a consequence, these low-frequency site-centered solutions persisted for a long time in the numerical simulation, and thus the effect of oscillatory instability is quite weak. However, we also provided case examples of their (long-time) instabilities that led to their complete destruction and ensuing apparently chaotic dynamics within the lattice. We showed that the distribution of Floquet multipliers and hence stability of the dark breather solutions are significantly affected by the mass ratio and breather frequency.

A challenge left for the future work is to rigorously prove the existence of small-amplitude exact periodic traveling wave and dark breather solutions of system (3.2) using the approximate solutions obtained from the generalized DpS equations. Another intriguing aspect to

further consider involves the mobility of the dark breathers, and its association with the dynamical instability of the states, as well as possibly with the famous Peierls-Nabarro barrier associated with the energy difference between bond- and site-centered solutions, i.e., the energy barrier that needs to be "overcome" in order to have mobility of the dark breathers. Equally important and relevant would be an effort to analytically understand the modulational stability properties of the lattice, perhaps at the DpS level and compare them with corresponding systematic numerical computations. On the experimental side, it will be interesting to investigate whether we can generate dark breathers by exciting the both ends of a finite chain in a way similar to [19]. Additionally, exciting small-amplitude traveling waves through boundary excitations, e.g. in the woodpile chain of [31] and observing experimentally their evolution through lased Doppler vibrometry would also be particularly relevant.

4.0 BREATHERS IN A LOCALLY RESONANT GRANULAR CHAIN WITH PRECOMPRESSION

In this chapter, we study discrete breathers in the locally resonant granular chain under nonzero precompression. In the non-resonant limit (regular granular chain, zero mass ratio), such a system belongs to the general class of Fermi-Pasta-Ulam (FPU) lattice models (e.g. see [36,69–78] and references therein), with dispersion relation for plane wave solutions of the linearized problem possessing only acoustic spectrum. At finite mass ratio, the dispersion relation has both acoustic and optical branches. In this respect the problem is somewhat reminiscent of diatomic FPU chains, although the optical branch is quite different in our case. In the small-amplitude limit the dynamics of the system is weakly nonlinear. This dynamical regime has been well studied for the FPU problem, as has its generalized version with an additional onsite potential [27,34–36,71–73,75–77]. In particular, the established conditions for bifurcation of discrete breathers for this class of problems [27,75,76] rule out the existence of bright breathers in the homogeneous non-resonant granular chain under precompression, the limiting case of our problem when the mass ratio is zero and the dispersion relation has only an acoustic branch. In this case, dark breathers were identified in [18] as the *only* possible type of intrinsically localized mode. The *defocusing* nonlinear Schrödinger equation (NLS), which has tanh-type solutions, is derived in [18] as the modulation equation for waves with frequencies near the edge of the linear acoustic spectrum and used to construct initial conditions for numerical computation and analysis of the dark breathers. In another limiting case, when the mass ratio goes to infinity and the secondary masses have zero initial conditions, the system approaches the Newton's cradle model with precompression, a problem with purely an optical dispersion branch. In this case, traveling bright breathers were investigated in [21] via the analysis of the corresponding *focusing* NLS, which admits

sech-type solutions.

To explore the weakly nonlinear dynamics at finite mass ratio, we use a multiscale asymptotic method (see [34–36] and references therein) and derive the classical NLS equation, yielding closed-form solutions of sech-type and tanh-type in the focusing and defocusing cases, respectively.

We investigate how well the dynamics governed by the focusing NLS equation approximates the dynamics of the moving bright breather solutions of the original system. Provided that certain non-resonance conditions are satisfied, the approximation remains valid until the wave number approaches zero, which corresponds to a singular point for the NLS solution; we discuss the relevant details below. We find that the focusing NLS successfully captures the dynamics of small-amplitude optical bright breathers at various mass ratios and some wave numbers, for which robust motion of the breather is observed. At some other wave numbers for the optical branch and in the acoustic case the numerical solutions tend to deviate from the NLS approximation. In particular, in both optical and acoustic cases we observe formation of additional small-amplitude bright breathers associated with the other dispersion branch that eventually detach from its parent breather and move in either the same or the opposite direction.

Following the approach in [18], we then analyze the defocusing NLS at the edges of both optical and acoustic branches that correspond to wave number equal to π, and use the static solutions of the modulation equation to construct the approximate standing dark breather solutions. A continuation procedure based on a Newton-type method with initial conditions built from the approximation ansatz is employed to compute numerically exact dark breathers for a wide range of frequencies and at different mass ratios. Interestingly, the resulting branches of solutions also include large-amplitude dark breathers, whose dynamics is *strongly nonlinear*.

We examine the stability of the numerically exact dark breathers of both weakly and strongly nonlinear types. Our numerical results suggest that small-amplitude weakly nonlinear dark breather solutions with frequencies close to the linear frequencies of the system are stable, in analogy to what was found for the homogeneous granular chain in [18]. As the amplitude of the dark breather solution becomes relatively large compared to the amount of

precompression, the solutions start to exhibit a very strong modulational instability of the background, eventually leading to their complete destruction and the emergence of chaotic dynamics. However, when the real instability of the solution is dominant, it may give rise to steady propagation of a dark breather at large enough time. We also show that the mass ratio plays a substantial role in the oscillatory instability of the background of the dark breathers. In contrast, the value of the mass ratio has a less significant effect on the real instability modes for both the strongly and weakly nonlinear solutions, as we infer from the similar patterns of positive real Floquet multipliers at different mass ratios.

The chapter is organized as follows. Sec. 4.1 introduces the model and the dispersion relation for plane waves. We derive the modulation equations of NLS type in Sec. 4.2, with more technical details included in Appendix C. In Sec. 4.3 we investigate the focusing NLS equation and the validity of its approximation of the moving breather solutions of the original system. In Sec. 4.4 we construct the approximate standing dark breathers using the defocusing NLS equations. A continuation procedure is used in Sec. 4.5 to compute numerically exact dark breathers bifurcating from the edges of optical and acoustic spectra, and the linear stability of the obtained solutions is studied in Sec. 4.6. Concluding remarks can be found in Sec. 4.7.

4.1 THE MODEL

We consider the model described in Sec. 3.1, with the primary masses in the granular chain precompressed by the static load F_0. The dynamics of the system is then governed by

$$\begin{aligned} m_1 \frac{d^2\tilde{u}_n}{d\tilde{t}^2} &= \mathcal{A}(\tilde{\delta}_0 + \tilde{u}_{n-1} - \tilde{u}_n)_+^\alpha - \mathcal{A}(\tilde{\delta}_0 + \tilde{u}_n - \tilde{u}_{n+1})_+^\alpha - K(\tilde{u}_n - \tilde{v}_n), \\ m_2 \frac{d^2\tilde{v}_n}{d\tilde{t}^2} &= K(\tilde{u}_n - \tilde{v}_n). \end{aligned} \tag{4.1}$$

where the new parameter $\tilde{\delta}_0 = (F_0/\mathcal{A})^{1/\alpha}$ is the equilibrium overlap of the adjacent primary masses due to the precompression, and all the other parameters have the same meaning as

in (3.1). Rescaling the equations as in Sec. 3.1, we obtain the dimensionless system

$$\begin{aligned} \ddot{u}_n &= V'(\delta^+ u_n) - V'(\delta^- u_n) - \kappa(u_n - v_n) \\ \rho\ddot{v}_n &= \kappa(u_n - v_n), \end{aligned} \tag{4.2}$$

where $\delta_0 = \tilde{\delta}_0/R$ is the rescaled static overlap, and $V(r)$ is the interaction potential in the form

$$V(r) = \frac{1}{\alpha+1}(\delta_0 - r)_+^{\alpha+1} + \delta_0^\alpha r - \frac{1}{\alpha+1}\delta_0^{\alpha+1} \tag{4.3}$$

that satisfies $V(0) = V'(0) = 0$. Here we recall that $\ddot{u}_n$ and $\ddot{v}_n$ are the accelerations of the primary and secondary masses, respectively, $\rho = m_2/m_1$ is the ratio of two masses, κ measures the relative strength of the linearly elastic springs connecting primary and secondary masses, and $\delta^+ u_n = u_{n+1} - u_n$ and $\delta^- u_n = u_n - u_{n-1}$ define the forward and backward shift operators, respectively. Notice that when $r \ll \delta_0$, it is relevant to consider the Taylor expansion

$$V(r) = K_2\frac{r^2}{2} + K_3\frac{r^3}{3} + K_4\frac{r^4}{4} + O(|r|^5), \tag{4.4}$$

where $K_2 = \alpha\delta_0^{\alpha-1}$, $K_3 = -\frac{1}{2}\alpha(\alpha-1)\delta_0^{\alpha-2}$ and $K_4 = \frac{1}{6}\alpha(\alpha-1)(\alpha-2)\delta_0^{\alpha-3}$. Linearizing the system (4.2) about the equilibrium state, we obtain

$$\ddot{u}_n = K_2(u_{n+1} - 2u_n + u_{n-1}) - \kappa(u_n - v_n), \quad \rho\ddot{v}_n = -\kappa(v_n - u_n). \tag{4.5}$$

The linear system has nontrivial plane wave solutions in the form

$$u_n(t) = Ae^{i(n\theta - \omega t)}, \quad v_n(t) = Be^{i(n\theta - \omega t)}$$

with wave number $\theta \in (-\pi, \pi]$, frequency ω and amplitudes A and B, provided that the matrix

$$\mathbf{M} = \begin{pmatrix} \omega^2 - D - \kappa & \kappa \\ \kappa/\rho & \omega^2 - \kappa/\rho \end{pmatrix} \tag{4.6}$$

with $D = D(\theta) = 4K_2\sin^2(\theta/2)$ has a vanishing determinant. This yields the dispersion relation

$$\omega^2 = \omega_\pm^2(\theta) = \frac{D + \kappa + \kappa/\rho \pm \sqrt{(D + \kappa + \kappa/\rho)^2 - 4D\kappa/\rho}}{2}. \tag{4.7}$$

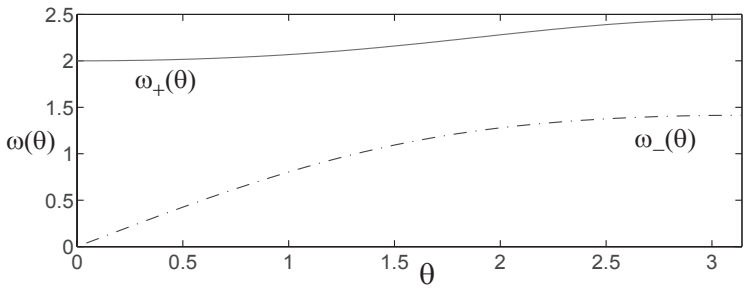

Figure 4.1: The optical (solid) and acoustic (dashed) branches of the dispersion relation (4.7). Due to the even symmetry about $\theta = 0$, only $[0, \pi]$ interval is shown. Here $\delta_0 = 4/9$, $\kappa = 1$ and $\rho = 1/3$.

The relation has two branches: optical, $\omega_+(\theta)$, and acoustic, $\omega_-(\theta)$, as shown in Fig. 4.1. One can show that $\omega_+(\theta)$ and $\omega_-(\theta)$ are increasing functions of θ in $[0, \pi]$ and that $\omega_-(\pi) < \omega_+(0)$, implying the existence of a gap between the two branches.

Note that in the limit $\rho \to 0$, the model reduces to the one for a regular (non-resonant) homogeneous granular chain with precompression, which is governed by [14]

$$\ddot{u}_n = (\delta_0 + u_{n-1} - u_n)_+^\alpha - (\delta_0 + u_n - u_{n+1})_+^\alpha. \tag{4.8}$$

In this case the dispersion relation for the linearized problem only has the acoustic branch

$$\omega^2(\theta) = 4K_2 \sin^2(\theta/2). \tag{4.9}$$

In the opposite limit of $\rho \to \infty$ and for zero initial conditions for $v_n(t)$, the system approaches a precompressed granular chain with quadratic onsite potential, i.e., a Newton's cradle model with precompression [21], described by

$$\ddot{u}_n + \kappa u_n = (\delta_0 + u_{n-1} - u_n)_+^\alpha - (\delta_0 + u_n - u_{n+1})_+^\alpha. \tag{4.10}$$

In this limit, the dispersion relation is purely optical and given by

$$\omega^2(\theta) = 4K_2 \sin^2(\theta/2) + \kappa. \tag{4.11}$$

4.2 DERIVATION OF THE NONLINEAR SCHRÖDINGER (NLS) EQUATION

To study the weakly nonlinear dynamics of the locally resonant chain, we begin by deriving the modulation equations for the plane-wave mode $E(t,n) := e^{i(n\theta-\omega t)}$, with $\theta \in (-\pi, \pi]$ and $\omega = \omega_+$ or ω_- defined in (4.7). Using a small parameter $\varepsilon > 0$, we introduce the slow time $\tau = \varepsilon^2 t$ and the macroscopic traveling wave coordinate $\xi = \varepsilon(n - ct)$, where $c = c_\pm := \omega'_\pm(\theta)$ is the group velocity. We seek solutions of (4.2) in the form of fast oscillating, small-amplitude patterns modulated by envelopes that vary slowly in space and time:

$$\begin{aligned} u_n(t) &= u_n^A(t) + O(\varepsilon^2) = \varepsilon\{A_{1,0}(\tau,\xi) + A_{1,1}(\tau,\xi)E(t,n) + c.c.\} + O(\varepsilon^2) \\ v_n(t) &= v_n^B(t) + O(\varepsilon^2) = \varepsilon\{B_{1,0}(\tau,\xi) + B_{1,1}(\tau,\xi)E(t,n) + c.c.\} + O(\varepsilon^2), \end{aligned} \tag{4.12}$$

where *c.c.* denotes complex conjugate. More precisely, following [34, 35] (see also [36]), we substitute the multiple-scale ansatz

$$u_n(t) = \sum_{k\in\mathbb{N}_1} \varepsilon^k \sum_{j=-k}^{k} A_{k,j}(\tau,\xi)E^j(t,n), \qquad v_n(t) = \sum_{k\in\mathbb{N}_1} \varepsilon^k \sum_{j=-k}^{k} B_{k,j}(\tau,\xi)E^j(t,n), \tag{4.13}$$

where $\mathbb{N}_1$ is the set of natural numbers $k \in \mathbb{N}, k \geq 1$, $A_{k,j}, B_{k,j} \in \mathbb{C}$, $A_{k,-j} = \bar{A}_{k,j}$ and $B_{k,-j} = \bar{B}_{k,j}$, into (4.2). As shown in Appendix C, this leads to the coupled modulation equations

$$i\partial_\tau A_{1,1} + \beta\partial_\xi A_{1,0}A_{1,1} + \frac{1}{2}\omega''\partial_\xi^2 A_{1,1} - h|A_{1,1}|^2 A_{1,1} = 0, \tag{4.14}$$

$$[c^2(1+\rho) - K_2]\partial_\xi^2 A_{1,0} = 8K_3 \sin^2(\theta/2)\bar{A}_{1,1}\partial_\xi A_{1,1} + c.c. \tag{4.15}$$

and the identities

$$B_{1,0} = A_{1,0}, \quad B_{1,1} = \frac{\kappa}{\kappa - \rho\omega^2} A_{1,1} \tag{4.16}$$

(one can check that $\kappa - \rho\omega_\pm^2 \neq 0$). In equations (4.14)-(4.15), we assume two *non-resonance conditions*,

$$(4\omega^2 - 4K_2\sin^2\theta - \kappa)(\kappa - 4\omega^2\rho) + \kappa^2 \neq 0 \tag{4.17}$$

and

$$c^2(1+\rho) - K_2 \neq 0, \tag{4.18}$$

and set

$$\beta = -4K_3 \sin^2(\theta/2)\gamma, \qquad \omega'' = \left\{ K_2 \cos\theta - c^2 \left[1 - \frac{3\omega^2\rho^2\kappa^2 + \rho\kappa^3}{(\rho\omega^2 - \kappa)^3} \right] \right\} \gamma \tag{4.19}$$

and

$$h = \left\{ \frac{16K_3^2 \sin^2\theta(1-\cos\theta)^2(\kappa - 4\omega^2\rho)}{(4\omega^2 - 4K_2\sin^2\theta - \kappa)(\kappa - 4\omega^2\rho) + \kappa^2} + 6K_4(1-\cos\theta)^2 \right\} \gamma, \tag{4.20}$$

where

$$\gamma = \frac{(\rho\omega^2 - \kappa)^2}{\omega[\rho\kappa^2 + (\rho\omega^2 - \kappa)^2]}. \tag{4.21}$$

Note that h is non-singular when (4.17) holds. Observe also that (4.15) can be rewritten as

$$\partial_\xi^2 A_{1,0} = \lambda \partial_\xi |A_{1,1}|^2, \tag{4.22}$$

where

$$\lambda = \frac{8K_3 \sin^2(\theta/2)}{c^2(1+\rho) - K_2} \tag{4.23}$$

is well-defined under (4.18). Integrating both sides of (4.22) with respect to ξ yields

$$\partial_\xi A_{1,0} = \lambda |A_{1,1}|^2 + f(\tau), \tag{4.24}$$

where $f(\tau)$ is an arbitrary time-dependent function. Substituting $\partial_\xi A_{1,0}$ into (4.14) then gives

$$i\partial_\tau A_{1,1} + \beta f(\tau) A_{1,1} + \frac{1}{2}\omega'' \partial_\xi^2 A_{1,1} + (\lambda\beta - h)|A_{1,1}|^2 A_{1,1} = 0. \tag{4.25}$$

Let

$$A(\xi, \tau) = A_{1,1}(\xi, \tau) e^{-i\beta F(\tau)}, \tag{4.26}$$

where $F(\tau)$ is the antiderivative of $f(\tau)$. From (4.25) it then follows that $A(\xi, \tau)$ satisfies the classical time-dependent nonlinear Schrödinger (NLS) equation

$$i\partial_\tau A(\xi, \tau) + \frac{1}{2}\omega'' \partial_\xi^2 A(\xi, \tau) - \widetilde{h}|A(\xi, \tau)|^2 A(\xi, \tau) = 0, \tag{4.27}$$

where we set

$$\widetilde{h} = h - \lambda\beta. \tag{4.28}$$

Equation (4.27) has solutions in the form

$$A(\xi,\tau) = \widetilde{A}(\xi)e^{i\mu\tau}, \tag{4.29}$$

where $\mu \in \mathbb{R}$ and $\widetilde{A}(\xi)$ is a real-valued function satisfying the stationary NLS equation

$$-\mu\widetilde{A}(\xi) + \frac{1}{2}\omega''\partial_\xi^2\widetilde{A}(\xi) - \widetilde{h}\widetilde{A}^3(\xi) = 0. \tag{4.30}$$

The *focusing case* of the NLS equation (4.27) occurs for $\omega''\widetilde{h} < 0$. In this case (4.30) admits sech-type solution

$$\widetilde{A}(\xi) = \sqrt{\frac{-2\mu}{\widetilde{h}}}\operatorname{sech}\left(\sqrt{\frac{2\mu}{\omega''}}\xi\right) \tag{4.31}$$

for μ such that $\mu\omega'' > 0$ and $\mu\widetilde{h} < 0$. Using (4.26) and (4.29), we then obtain

$$A_{1,1}(\xi,\tau) = \sqrt{\frac{-2\mu}{\widetilde{h}}}\operatorname{sech}\left(\sqrt{\frac{2\mu}{\omega''}}\xi\right)e^{i[\mu\tau+\beta F(\tau)]}, \tag{4.32}$$

and integrating (4.24) yields

$$A_{1,0}(\xi,\tau) = \frac{\lambda\sqrt{2\omega''\mu}}{|\widetilde{h}|}\tanh\left(\sqrt{\frac{2\mu}{\omega''}}\xi\right) + f(\tau)\xi + C(\tau). \tag{4.33}$$

On the other hand, when $\omega''\widetilde{h} > 0$, equation (4.27) becomes *self-defocusing*, and (4.30) has a tanh-type solution

$$\widetilde{A}(\xi) = \sqrt{\frac{-\mu}{\widetilde{h}}}\tanh\left(\sqrt{\frac{-\mu}{\omega''}}\xi\right) \tag{4.34}$$

for μ satisfying $\mu\omega'' < 0$ and $\mu\widetilde{h} < 0$. We then have

$$A_{1,1}(\xi,\tau) = \sqrt{\frac{-\mu}{\widetilde{h}}}\tanh\left(\sqrt{\frac{-\mu}{\omega''}}\xi\right)e^{i[\mu\tau+\beta F(\tau)]}. \tag{4.35}$$

Integrating (4.24), we obtain

$$A_{1,0}(\tau) = -\frac{\lambda\sqrt{-\omega''\mu}}{|\widetilde{h}|}\tanh\left(\sqrt{\frac{-\mu}{\omega''}}\xi\right) + \left(f(\tau) - \frac{\lambda\mu}{\widetilde{h}}\right)\xi + C(\tau). \tag{4.36}$$

Representative plots of $\operatorname{sign}(\omega''\widetilde{h})$ as a function of θ and ρ for optical and acoustic branches are shown in Fig. 4.2, where we vary ρ but fix the other parameters at the same values as in Fig. 4.1 ($\kappa = 1$, $\delta_0 = 4/9$ and $\alpha = 3/2$). From (4.19), (4.20), (4.23) and (4.28), one can

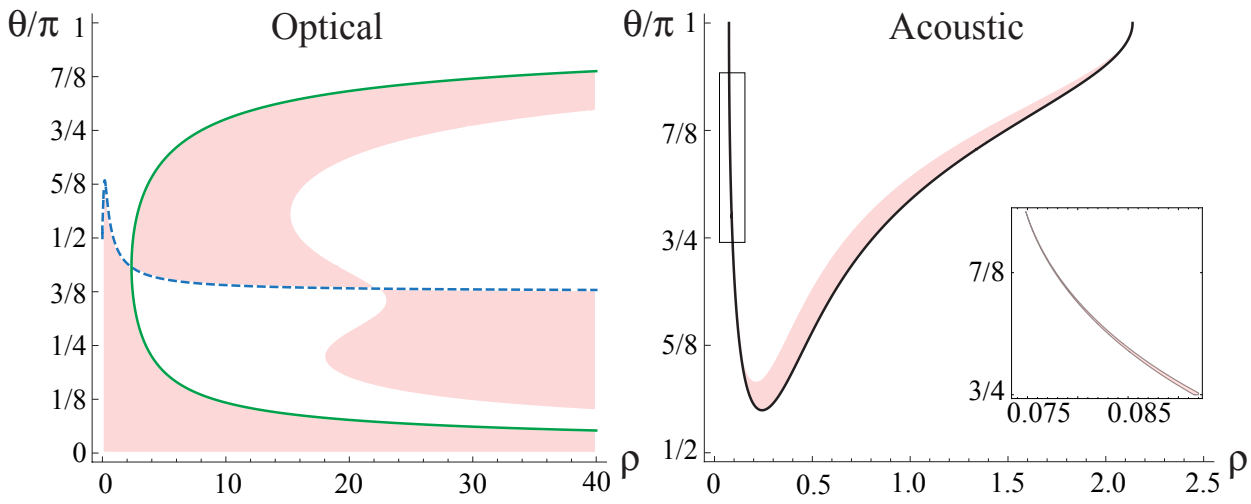

Figure 4.2: Plots of sign($\omega''\widetilde{h}$) for optical (left) and acoustic (right) branches. The focusing region is shaded in pink. Its boundaries for the optical case include $\omega''_+ = 0$ (blue dashed line) and the curve along which the second non-resonance condition (4.18) is violated (greed solid line). Black solid line in the acoustic case (right plot) corresponds to the curve along which the first non-resonance condition (4.17) breaks down. The remaining boundaries separating focusing (pink) and defocusing (white) regions corresponds to $\widetilde{h} = 0$. Inset zooms in on the region inside the rectangle. Here $\alpha = 3/2$, $\delta_0 = 4/9$, $\kappa = 1$.

see that $\omega''\widetilde{h}$ can change sign when $\omega'' = 0$, $\tilde{h} = 0$ or when $\tilde{h}$ has a singularity which occurs when either of the two non-resonance conditions, (4.17) and (4.18), is violated for $\theta \in (0, \pi)$.

For the optical branch of the dispersion relation, (4.17) always holds for the parameters we consider here, but the other non-resonance condition, (4.18), breaks down at some wave numbers for sufficiently large ρ (solid curve in the left plot of Fig. 4.2). In this case the sign of $\omega''_+\widetilde{h}_+$ also changes for any $\rho > 0$ at the inflection point of the dispersion relation ($\omega''_+ = 0$, dashed curve) and, for large enough ρ, when the numerator of $\tilde{h}$ in (4.28) vanishes. Thus, for sufficiently small ρ, $0 < \rho < 2.356$, we have the focusing regime (shaded in Fig. 4.2) for $\theta < \theta_c$, where $\omega''_+(\theta_c) = 0$, and the defocusing NLS otherwise. For larger ρ, focusing and defocusing regimes alternate, due to breakdown of (4.18), the inflection point, and, for $\rho \gtrsim 15.335$, $\tilde{h} = 0$. Interestingly, the focusing and defocusing regions "flip" at $\rho \approx 2.356$ and $\rho \approx 22.298$, where the boundary curves intersect, with focusing regime below the $\omega''_+ = 0$ curve at small ρ, above it for a range of wave numbers at intermediate mass ratios and below

the curve again for a θ-range at larger ρ.

We now turn to $\text{sign}(\omega''_- \widetilde{h}_-)$ and examine the acoustic dispersion branch shown in the right plot of Fig. 4.2. One can show that in this case the curvature of the dispersion curve is always negative, $\omega''_-(\theta) < 0$, for $\theta \in (0, \pi]$, yielding $0 \leq c_- = \omega'_-(\theta) < \omega'_-(0) = \sqrt{K_2/(1+\rho)}$. As a result, the second non-resonance condition (4.18) always holds for the acoustic branch at nonzero wave numbers. However, the first non-resonance condition breaks along the solid curve, changing the sign of $\tilde{h}_-$ from negative to positive, and hence the sign of $\omega''_- \widetilde{h}_-$ from positive to negative, at sufficiently large $\theta < \pi$ in the interval of mass ratios $0.074 < \rho < 2.137$. For each ρ in this interval, $\text{sign}(\omega''_- \widetilde{h}_-)$ changes again to positive (defocusing regime) at slightly larger θ due to $\tilde{h} = 0$. This yields a very narrow shaded focusing region, with the lower boundary for $\theta < \pi$ coinciding with the solid curve where (4.18) is violated. It should be noted that although this singularity curve includes points where $\theta = \pi$, the focusing region approaches this value at its ends but does not include it because $h(\theta)$ in (4.20), and therefore $\tilde{h}(\theta)$ in (4.28), does not have a singularity at $\theta = \pi$. Instead, as we approach each of the two end points of the focusing region where $\theta \to \pi$, the values of θ where $\tilde{h}_-$ is singular and where it vanishes for given ρ both approach π, so that at $\theta = \pi$ we have the defocusing case, $\tilde{h}_-(\pi)\omega''_-(\pi) > 0$ for $\rho > 0$. The focusing region is particularly narrow at smaller mass ratios, $\rho \gtrsim 0.074$ (see the inset in Fig. 4.2). Outside this region one has the defocusing regime. This includes $0 < \rho < 0.074$, in agreement with the non-resonant chain studied in [18] ($\rho = 0$), where only the defocusing case is possible.

To further illustrate these results, we show some plots of group velocity c, curvature ω'' and $\widetilde{h}$ as functions of the wave number θ in Fig. 4.3. One can see that at $\rho = 1/3$ the optical branch has negative $\tilde{h}_+$ in $(0, \pi]$ with no singularities, and the single transition from focusing to defocusing regime occurs due to the inflection point at $\theta = \theta_c \approx 1.892$ in the dispersion curve ($\omega''_+(\theta_c) = 0$). At $\rho = 3$, however, $\tilde{h}_+$ changes sign twice via singularities (breakdown of (4.18)), and together with the inflection point this yields three transition points separating focusing and defocusing regions (see also the left plot in Fig. 4.2). Meanwhile, the acoustic branch, as already noted, has no inflection points in $(0, \pi]$, $\omega''_- < 0$, and the transition from defocusing to focusing (for $\theta \in (1.784, 1.949)$) and back at $\rho = 1/3$ occurs through the change of sign of $\tilde{h}_-$ due to singularity (breakdown of (4.18)) and going through zero. At $\rho = 3$ we

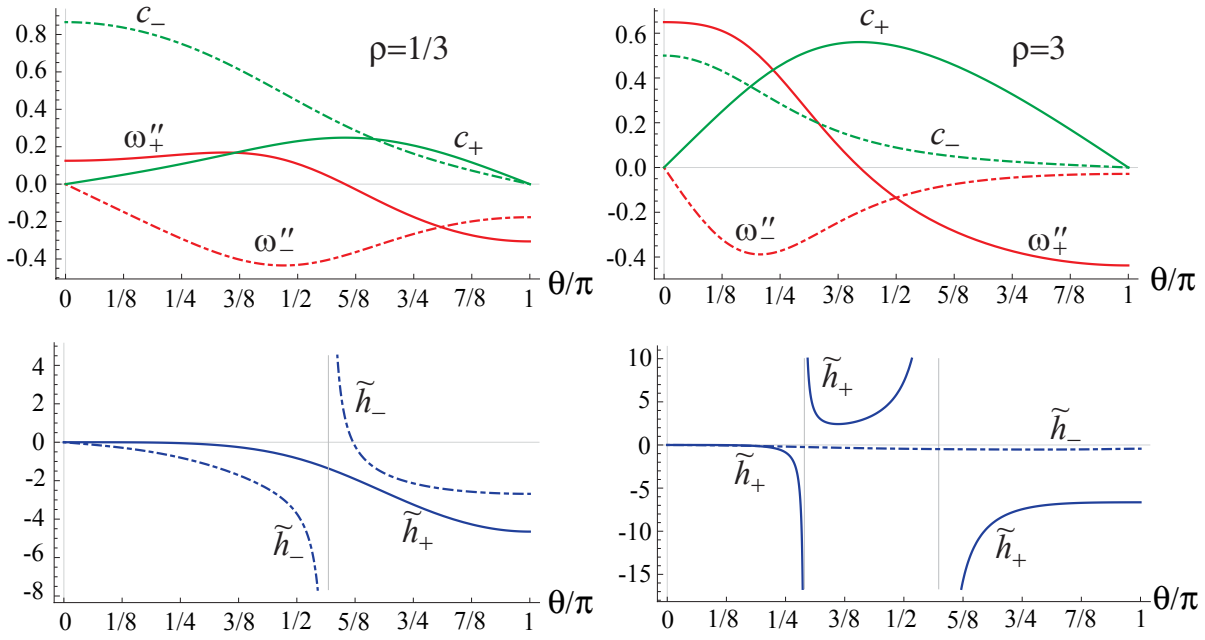

Figure 4.3: Representative plots of group velocity c (green), curvature ω'' (red) and $\widetilde{h}$ (blue) as functions of the scaled wave number θ/π at different mass ratios for optical (solid) and acoustic (dashed) branches. Here $\alpha = 3/2$, $\delta_0 = 4/9$, $\kappa = 1$.

have $\tilde{h}_- < 0$ in $(0, \pi]$ without singularities, so the regime is defocusing.

4.3 FOCUSING NLS AND MOVING BRIGHT BREATHERS

We now proceed to investigate how well the dynamics governed by the focusing NLS equations ($\omega''\widetilde{h} < 0$) approximates the solutions of original system (4.2). As before, it is convenient to rewrite (4.2) in terms of strain variables $x_n = u_n - u_{n-1}$ and $y_n = v_n - v_{n-1}$:

$$\begin{aligned} \ddot{x}_n &= V'(x_{n+1}) - 2V'(x_n) + V'(x_{n-1}) - \kappa(x_n - y_n) \\ \rho\ddot{y}_n &= \kappa(x_n - y_n). \end{aligned} \tag{4.37}$$

Using (4.12), (4.16), (4.32) and (4.33), we find that the approximate solutions given by the focusing NLS equation take the form

$$\begin{aligned} x_n^A(t) &= \delta^- u_n^A(t) = 2M_2\delta^-\{\mathrm{sech}[a(n - n_0 - ct)]\cos(n\theta - \omega_b t + \beta F(\varepsilon^2 t))\} \\ &+ M_1\delta^-\tanh[a(n - n_0 - ct)] + \varepsilon^2 f(\varepsilon^2 t) \\ y_n^A(t) &= \delta^- v_n^A(t) = \frac{2\kappa M_2}{\kappa - \rho\omega^2}\delta^-\{\mathrm{sech}[a(n - n_0 - ct)]\cos(n\theta - \omega_b t + \beta F(\varepsilon^2 t))\} \\ &+ M_1\delta^-\tanh[a(n - n_0 - ct)] + \varepsilon^2 f(\varepsilon^2 t), \end{aligned} \tag{4.38}$$

with arbitrary spatial translation by n_0. Here instead of $\mu\varepsilon^2$ we introduce the breather frequency $\omega_b = \omega - \mu\varepsilon^2$, a real number such that $|\omega - \omega_b| = O(\varepsilon^2)$, $(\omega - \omega_b)\omega'' > 0$, $(\omega - \omega_b)\tilde{h} < 0$, and set

$$M_1 = \frac{\lambda\sqrt{2\omega''(\omega - \omega_b)}}{|\widetilde{h}|}, \quad M_2 = \sqrt{\frac{2(\omega_b - \omega)}{\widetilde{h}}} \quad \text{and} \quad a = \sqrt{\frac{2(\omega - \omega_b)}{\omega''}}.$$

Recall that $f(\tau)$ is a slow-time varying function, independent of n and $F(\tau)$ is its antiderivative. In what follows we simply set $F(\tau) \equiv 0$ so that $f(\tau) \equiv 0$.

To numerically integrate (4.37), we start with initial condition determined from the first order approximation (4.38) at $t = 0$, along with initial velocities given by

$$\begin{aligned}
\dot{x}_n(0) &= c\,a\left\{-M_1\delta^-\mathrm{sech}^2[a(n-n_0)] + 2M_2\delta^-\tanh[a(n-n_0)]\mathrm{sech}[a(n-n_0)]\cos(n\theta)\right\} \\
&+ 2\omega_b M_2\delta^-\mathrm{sech}[a(n-n_0)]\sin(n\theta) \\
\dot{y}_n(0) &= c\,a\left\{-M_1\delta^-\mathrm{sech}^2[a(n-n_0)] + \frac{2\kappa M_2}{\kappa-\rho\omega^2}\delta^-\tanh[a(n-n_0)]\mathrm{sech}[a(n-n_0)]\cos(n\theta)\right\} \\
&+ \frac{2\omega_b\kappa M_2}{\kappa-\rho\omega^2}\delta^-\mathrm{sech}[a(n-n_0)]\sin(n\theta).
\end{aligned} \tag{4.39}$$

We use the same parameters as before ($\alpha = 3/2$, $\delta_0 = 4/9$, $\kappa = 1$), choose a relatively small mass ratio, $\rho = 1/3$ and start by considering the optical case. Recall from the discussion in Sec. 4.2 (see also the left plots in Fig. 4.2 and Fig. 4.3) that for this mass ratio the focusing regime takes place at $0 < \theta < \theta_c$, where $\theta_c \approx 1.892$ satisfies $\omega_+''(\theta_c) = 0$. We first consider the wave number $\theta = \pi/2 < \theta_c$. Numerical integration is performed on the lattice of size $2N+1$ with free-end boundary conditions $x_{-N-1} = x_{-N}$ and $x_{N+1} = x_N$. As shown in Fig. 4.4, the agreement between the numerical evolution of (4.37) and the approximate analytical solution is excellent, even after a long time at $t = 200\,T_b$, where $T_b = 2\pi/\omega_b = 2.8885$ is the period of the modulated wave. The relative errors of the approximation (4.38), defined by $E_x(t) = ||x_n^A(t) - x_n(t)||_\infty/||x_n(0)||_\infty$ and $E_y(t) = ||y_n^A(t) - y_n(t)||_\infty/||y_n(0)||_\infty$, remain less than 3.5% over the time of computation. In the simulation, we observe that the numerically exact solutions have a localized structure which moves to the right end at the speed approximately equal to the group velocity $c_+ \approx 0.23$. Meanwhile, the amplitudes of the oscillations vary during the simulation and are well captured by the NLS approximation (4.38). Snapshots of these *moving bright breathers* at different times are also shown in Fig. 4.4.

To further illustrate the strong mobility of the bright breather, we consider the energy density (energy stored at the nth site):

$$e_n = \frac{1}{2}\dot{u}_n^2 + \frac{\rho}{2}\dot{v}_n^2 + \frac{\kappa}{2}(u_n - v_n)^2 + \frac{1}{5}[(\delta_0 - \delta^- u_n)_+^{5/2} + (\delta_0 - \delta^+ u_n)_+^{5/2}] + \frac{1}{2}\delta_0^{3/2}(u_{n+1} - u_{n-1}) - \frac{2}{5}\delta_0^{5/2}. \tag{4.40}$$

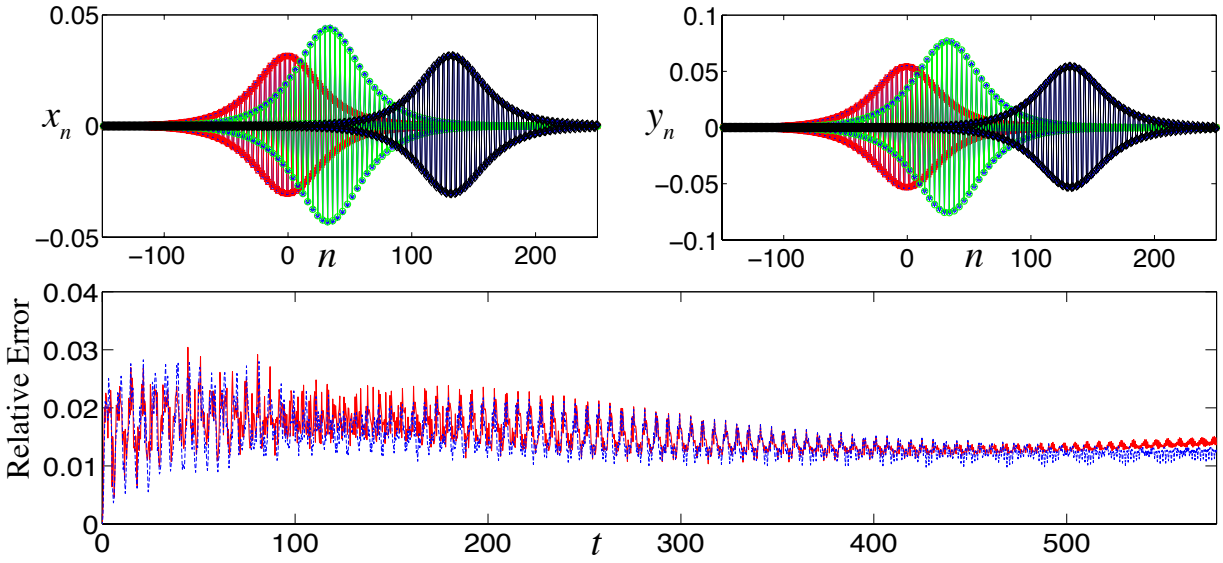

Figure 4.4: Top plots: snapshots of a moving bright breather solution x_n and y_n of the original system (4.2), with initial data determined from (4.38), (4.39). The breather moving from the middle of the chain to the right is shown here at $t = 0$ (connected red squares), $t = 50.125\,T_b \approx 145$ (connected green circles) and $t = 200\,T_b \approx 578$ (connected black squares). The same plots compare the time snapshots of the approximate analytical solution (connected blue stars) and the numerical evolution result at the same times. Bottom plot: relative errors $E_x(t)$ (solid red curve) and $E_y(t)$ (dashed blue curve). Here $\theta = \pi/2$, $\kappa = 1$, $\rho = 1/3$, $\delta_0 = 4/9$, $\omega_b = \omega - 0.0001 = 2.1752$, $N = 500$ and $n_0 = 0$.

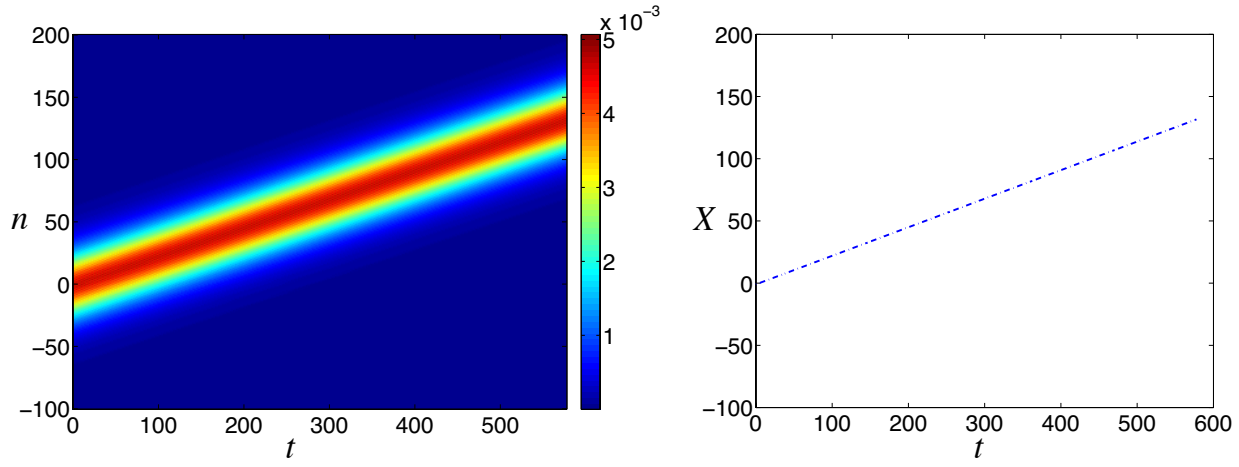

Figure 4.5: Left plot: energy density of a moving bright breather in the system (4.2). Right plot: time evolution of the breather's energy center. Here all the parameters are the same as in Fig. 4.4.

The left plot in Fig. 4.5 shows the energy density in the system (4.2), and the right plot displays the time evolution of the (local) energy center of mass, which is defined by

$$X = \frac{\sum_{i=n'-m}^{n'+m} i e_i}{\sum_{i=n'-m}^{n'+m} e_i}, \tag{4.41}$$

with n' being the location of the maximum energy density of the breather and $m > 0$ an integer which accounts for the width of the breather (we set $m = 100$).

In the second numerical run, we choose a smaller wave number $\theta = \pi/8$, while the other parameters remain the same. The linear frequency is now given by $\omega = 2.0098$ which is fairly close to the $\theta = 0$ edge of the optical branch. As shown in Fig. 4.3, the corresponding value of $|\widetilde{h}|$ decreases dramatically, so that the amplitude of the strain profiles increases. In fact, we now have $||x_n(0)||_\infty \approx 0.208 < \delta_0$, which is of the same order as $\delta_0 = 0.444$. We perform the same numerical integration over the time interval $[0, 150\, T_b]$, where $T_b = 2\pi/\omega_b = 3.1265$ and $\omega_b = \omega - 0.0001 = 2.0097$. As shown in the bottom plot of Fig. 4.6, the NLS approximation remains excellent at the early stage of the simulation, with relative errors less than 3 % when $t \leq 150$. However, later the approximation error becomes large, and the energy spreads out towards both ends of the chain, as shown in Fig. 4.7. The ensuing waveform no longer preserves the structure of a breather.

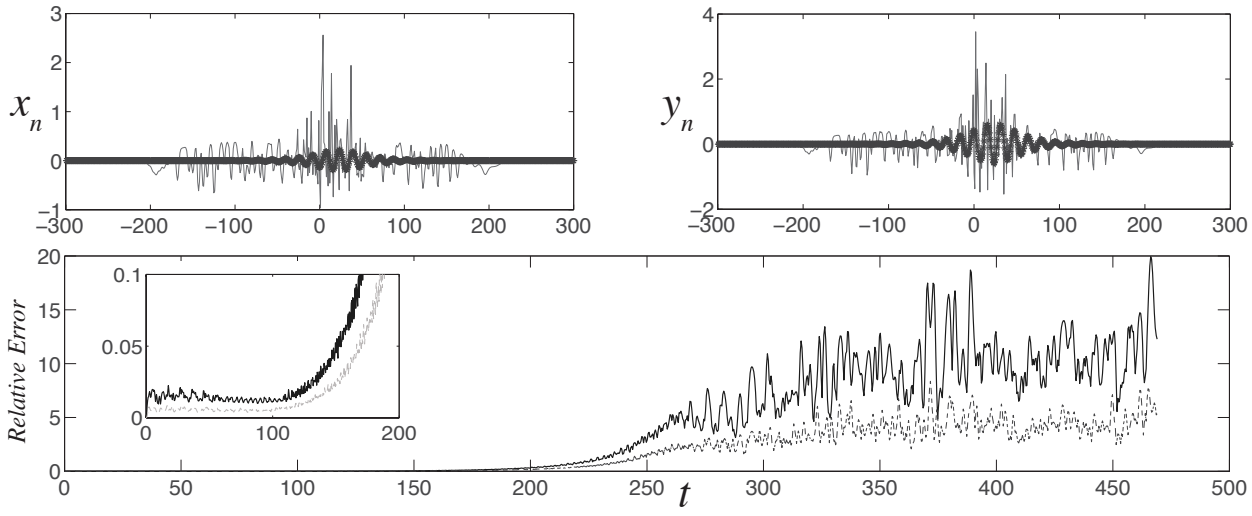

Figure 4.6: Top plots: comparison of time snapshot of approximate solution (connected stars) and exact solution (grey curve) at $t = 150\,T_b \approx 469$. Bottom plot: relative errors $E_x(t)$ (solid curve) and $E_y(t)$ (dashed curve). Inset: the relative error for $t \in [0, 200]$. Here $\theta = \pi/8$, $\omega_b = \omega - 0.0001 = 2.0097$, and the other parameters are the same as in Fig. 4.4.

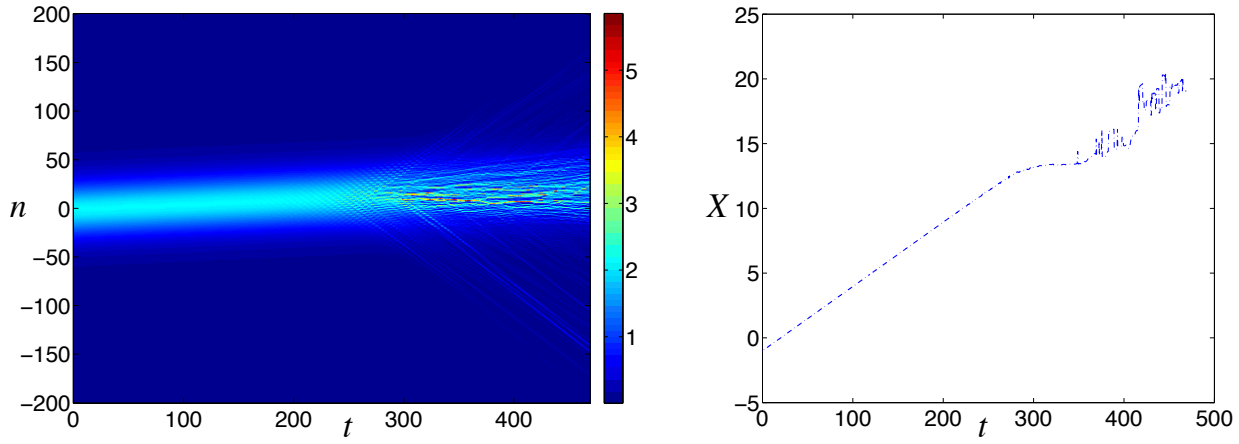

Figure 4.7: Left plot: energy density of a moving breather in system (4.2). Right plot: time evolution of the breather's energy center. Here $\theta = \pi/8$, $\omega_b = \omega - 0.0001 = 2.0097$, and the other parameters are the same as in Fig. 4.4.

An interesting question is whether there exist static bright breathers at the $\theta = 0$ edge of optical branch. Recall that the order of the approximate solution (4.38) roughly depends on the magnitude of M_1 and M_2 and thus on $\widetilde{h}$ that appears in their denominators. As shown in Fig. 4.3, the value of $\widetilde{h}$ becomes extremely small when θ is close to zero. Hence we need to choose ω_b very close to ω to ensure that the approximate solutions are within the small-amplitude regime. Meanwhile, the width of the moving breather is $\sim |\omega - \omega_b|^{-1/2}$ when $\omega \to \omega_b$ (it is determined by the factor $1/a$ according to the sech functional form in (4.38)). When $|\omega - \omega_b|$ is very small, we have to run simulations on an extremely long chain in order to observe the localized structure with a decaying tail. Therefore, it is numerically impractical to investigate static bright breathers as a limit of the moving ones using the focusing NLS approximation (4.38). However, the multiscale analysis used to derive the modulation equations still holds for $\theta = 0$, yielding $\beta = h = c = 0$ so that (4.14)-(4.15) become the linear equations

$$i\partial_\tau A_{1,1} + \frac{1}{2}\omega''\partial_\xi^2 A_{1,1} = 0, \quad \partial_\xi^2 A_{1,0} = 0 \tag{4.42}$$

where $\omega'' = K_2\gamma = \kappa K_2/\omega^3$. Given the absence of localization at this order of the asymptotic expansion (4.12), we do not have any evidence of the existence of static bright breathers in this limit.

We now consider wave numbers above $\pi/2$ but below θ_c at the same mass ratio $\rho = 1/3$. In the numerical simulation, we observe that the NLS approximation of the moving bright breathers remains excellent over a finite time interval until the wave number is close to $\theta_c \approx 1.892$, which, as we recall, marks the boundary between focusing and defocusing regions at our parameter values. To illustrate what happens below but very close to this boundary, we consider the wave number $\theta = 3\pi/5 \approx 1.885$ and perform the numerical integration over the time interval $[0, 200\,T_b]$, where $T_b = 2\pi/\omega_b = 2.791$ and $\omega_b = \omega - 0.0001 = 2.2512$. As illustrated by the snapshots of the strain profiles of x_n and y_n at time $t = 200\,T_b \approx 558.2$, as well as by the space-time evolution of the energy density in Fig. 4.8, the resulting waveform mostly preserves its localized structure and moves to the right at the velocity approximately equal to c_+. However, we observe the growing trend of the relative error of the NLS approximation emerging from the very beginning of the simulation. Note also that the

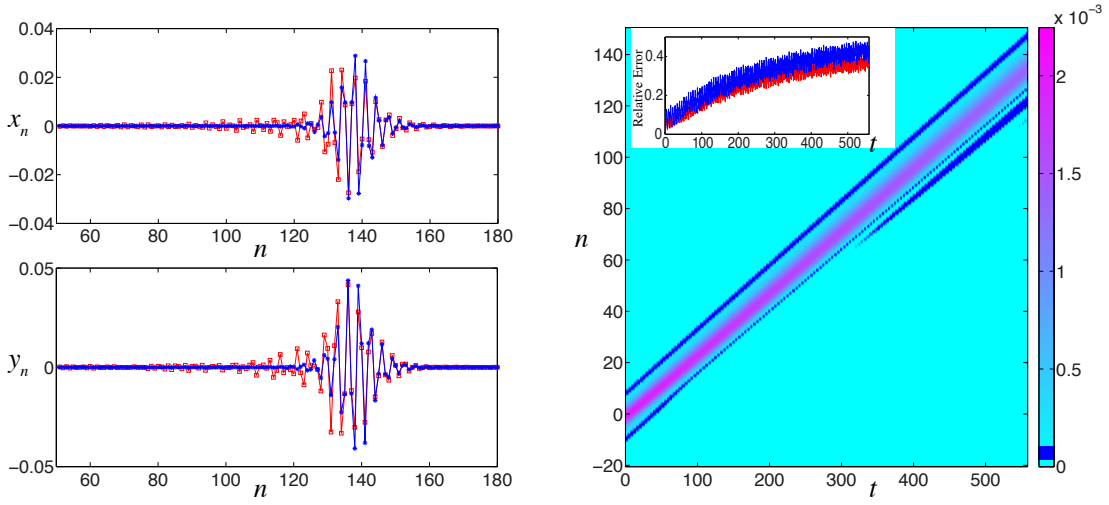

Figure 4.8: Left panels: comparison of the time snapshots of the approximate analytical solution (connected blue stars) and the numerical evolution result (red squares) at $t = 200\,T_b \approx 558.2$ for $\theta = 3\pi/5$, $\omega_b = \omega - 0.0001 = 2.2512$, $N = 1000$; the other parameters are the same as in Fig. 4.4. Right panels: energy density of the moving bright breather in the system (4.2). The dark blue color marks a range of small energy densities in order to better show the growing size of the tail behind the breather. The inset depicts the relative errors $E_x(t)$ (red) and $E_y(t)$ (blue).

approximation fails to capture the increasing size of the tail in the numerical solution, which suggests that the optical bright breathers with wave numbers near θ_c cannot be robustly sustained for long-time dynamical evolutions.

We next investigate bright breathers associated with the acoustic branch. From the discussion in Sec. 4.2 (see also the right plot in Fig. 4.2 and the left plots in Fig. 4.3), we recall that in this case the focusing regime takes place only in a narrow interval of wave numbers for a range of small enough mass ratios. In the case $\rho = 1/3$, with other parameters kept the same as before, this θ-interval is $(1.7841, 1.949)$. For moving acoustic bright breathers associated with wave numbers θ in the lower part of the focusing θ-interval, we observed dynamical features similar to the one discussed above for optical breathers and illustrated in Fig. 4.8. At wave numbers near the upper bound of this interval, when $\widetilde{h}_-$ decreases and approaches zero, yielding a relatively large amplitude of $||x_n(0)||_\infty$, we observed another small-amplitude bright breather eventually detaching from the original waveform and moving to the left with constant velocity near $-c_+$, suggesting that this second breather is an *optical*

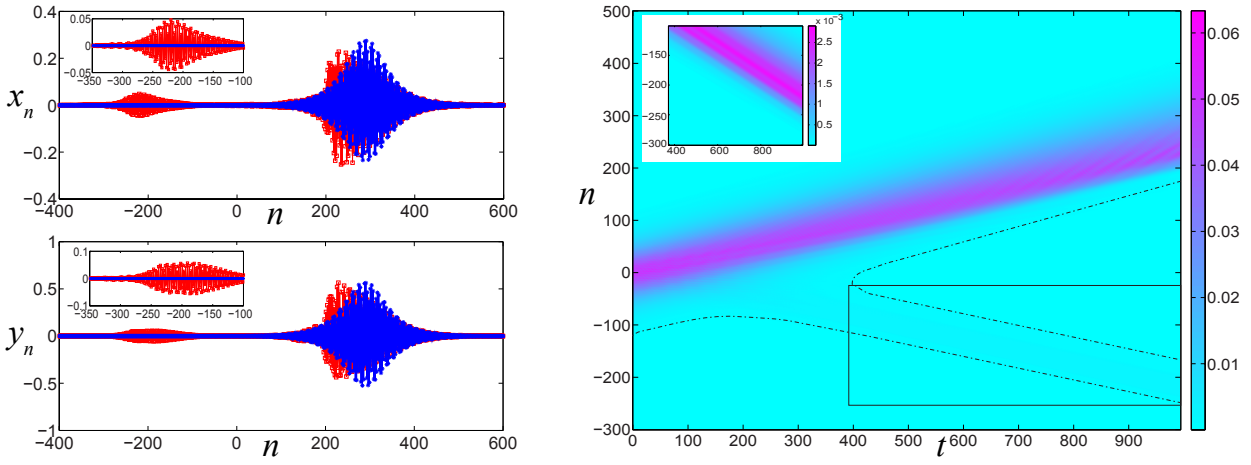

Figure 4.9: Left panels: comparison of the time snapshots of the approximate analytical solution (acoustic bright breather, connected blue stars) and the numerical evolution result (connected red squares) at $t = 200\,T_b \approx 994$ for $\theta = 1.948$, $\omega_b = \omega - 0.0001 = 1.264$, $N = 1000$; the other parameters are the same as in Fig. 4.4. Insets zoom in on the small-amplitude optical breather that eventually separates from the initial acoustic breather. Right panel: energy density of the numerical solution of the system (4.2) showing the energy density of the parent breather (darker color) and the small-amplitude breather detaching from it (faint lighter color bounded by the dash-dotted lines for better visibility), also shown in the inset that enlarges the region inside the rectangle.

one. See, for example, the results of the numerical simulation for $\theta = 1.948$ shown in Fig. 4.9. Clearly, the NLS approximation does not capture this feature.

We now investigate the effect of larger mass ratios on the optical bright breathers and their NLS approximation (recall that in the acoustic case the NLS equation is defocusing at large enough ρ). We first consider the mass ratio $\rho = 10$, at which the focusing regime corresponds to two disjoint θ-intervals: $(0, 0.3681)$ and $(1.2263, 2.4389)$. At wave numbers in the upper part of each interval, we found that NLS provides an excellent approximation of the corresponding small-amplitude moving bright breather over a finite time. Similarly to the results shown in Fig. 4.6 and Fig. 4.7 for the case $\rho = 1/3$, at sufficiently small wave numbers the localized structure eventually breaks down. At wave numbers near the lower bound of the θ-interval $(1.2263, 2.4389)$, we observe not only the increasing size of the tail in the numerical solution, similar to the example shown in Fig. 4.8 for the case $\rho = 1/3$, but also the emergence of a train of bright-breather-like structures clearly visible in the y_n variable that separate from the initial breather and slowly move in both directions with

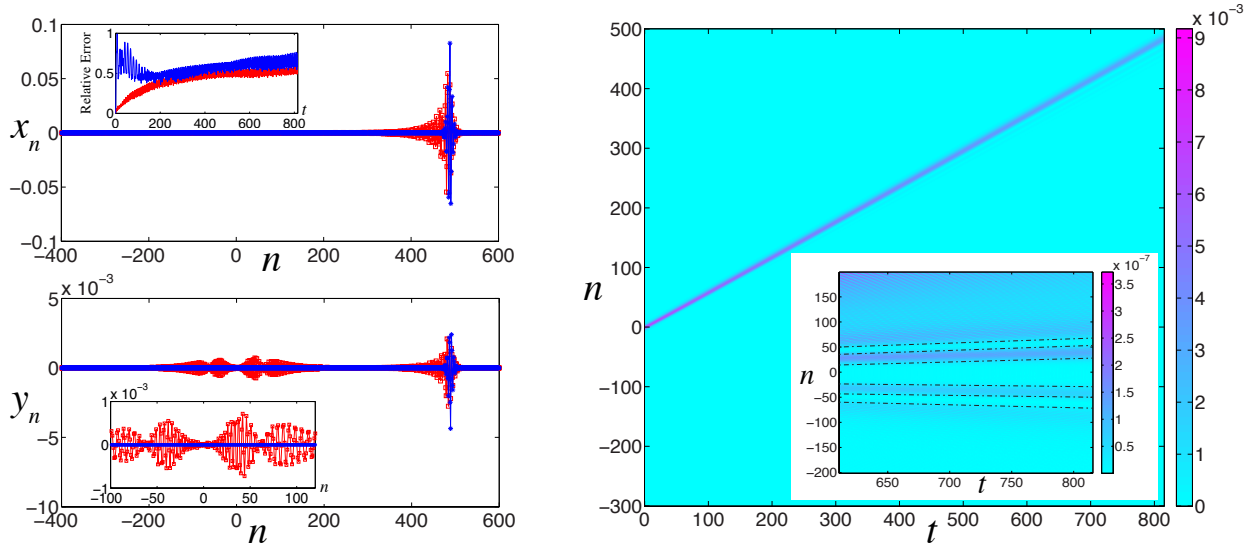

Figure 4.10: Left panels: comparison of the time snapshots of the approximate analytical solution (optical bright breather, connected blue stars) and the numerical evolution result (connected red squares) at $t = 200\,T_b \approx 815.28$ for $\rho = 10$, $\theta = 1.23$, $\omega_b = \omega - 0.0001 = 1.5414$, $N = 1000$; the other parameters are the same as in Fig. 4.4. Relative errors $E_x(t)$ (red) and $E_y(t)$ (blue) are shown in the top left inset. Bottom left inset zooms in on the train of acoustic waveforms that eventually separate from the initial optical breather. Right panel: energy density of the numerical solution of the system (4.2). The inset zooms in on the train of acoustic breather-like structures (not visible in the main energy plot), with dash-dotted lines added for better visibility.

speed approximately equal to c_-, suggesting their acoustic nature. Meanwhile, the optical breather initiated by the NLS approximation propagates to the right with velocity close to c_+. See, for example, Fig. 4.10, where the wave number is $\theta = 1.23$, and we have $c_- \approx 0.0754$ and $c_+ \approx 0.6$.

At $\rho = 30$, there are three focusing intervals, with θ in $(0, 0.1927)$, $(0.3775, 1.1952)$ and $(2.3814, 2.7346)$, respectively. We observed stable motion of small-amplitude optical bright breathers with wave numbers in the first and third intervals over a finite time. At wave numbers in the second (middle) interval, we obtained results similar to the one shown in Fig. 4.10.

4.4 DEFOCUSING NLS AND STANDING WAVE SOLUTIONS

We now turn our attention to the defocusing case ($\omega''\widetilde{h} > 0$). Using (4.12), (4.35) and (4.36), we obtain the approximate solutions in terms of strain variables given by

$$\begin{aligned} x_n^A(t) = \delta^- u_n^A(t) &= \varepsilon\delta^-\{M_3 + 2M_4\cos\left[n\theta - \widetilde{\omega}_b t + \beta F(\varepsilon^2 t)\right]\}\tanh[\eta\varepsilon(n - n_0 - ct)] \\ &\quad + \varepsilon^2\left\{f(\varepsilon^2 t) - \frac{\lambda\mu}{\widetilde{h}}\right\} \\ y_n^A(t) = \delta^- v_n^A(t) &= \varepsilon\delta^-\{M_3 + \frac{2\kappa M_4}{\kappa - \rho\omega^2}\cos\left[n\theta - \widetilde{\omega}_b t + \beta F(\varepsilon^2 t)\right]\}\tanh[\eta\varepsilon(n - n_0 - ct)] \\ &\quad + \varepsilon^2\left\{f(\varepsilon^2 t) - \frac{\lambda\mu}{\widetilde{h}}\right\}, \end{aligned} \tag{4.43}$$

where we define

$$M_3 = -\frac{\lambda\sqrt{-\omega''\mu}}{|\widetilde{h}|}, \quad M_4 = \sqrt{\frac{-\mu}{\widetilde{h}}}, \quad \text{and} \quad \eta = \sqrt{-\frac{\mu}{\omega''}}.$$

Here n_0 corresponds to the spatial translation and $\widetilde{\omega}_b = \omega - \mu\varepsilon^2$, where μ is any real number such that $\mu\omega'' < 0$, $\mu\tilde{h} < 0$. Again, $f(\tau)$ in the $O(\varepsilon^2)$ term is undetermined.

We are particularly interested in seeking standing wave solutions (i.e. stationary dark breathers) when the wave number is on the $\theta = \pi$ edges of the optical or acoustic branches, so that the group velocity c vanishes. This yields in (4.19), (4.23) and (4.28)

$$\beta = -4K_3\gamma, \quad \widetilde{h} = (24K_4 - 32K_3^2/K_2)\gamma, \quad \omega'' = -K_2\gamma, \quad \lambda = -\frac{8K_3}{K_2}. \tag{4.44}$$

Then $\omega''\widetilde{h} = -(24K_2K_4 - 32K_3^2)\gamma^2 > 0$, which corresponds to the defocusing case. The same condition was obtained, e.g., in [18]; see also the discussion therein. Since $f(\tau)$ is an arbitrary function independent of ξ, we set

$$f(\varepsilon^2 t) \equiv \frac{\lambda\mu}{\widetilde{h}} \tag{4.45}$$

to eliminate the ε^2-term in (4.43). The antiderivative of $f(\tau)$ is now given by $F(\tau) = \lambda\mu\tau/\widetilde{h}$, which leads to

$$\beta F(\tau) = -\frac{2\mu\tau}{3} \tag{4.46}$$

after evaluating K_2, K_3, K_4 for $\alpha = 3/2$ (see (4.4)). Substituting (4.46) into the cosine terms of (4.43) yields

$$\cos\left[n\theta - \widetilde{\omega}_b t + \beta F(\varepsilon^2 t)\right] = \cos\left(\omega - \frac{1}{3}\mu\varepsilon^2\right)t$$

and the leading order NLS approximation (4.43) is now given by

$$\begin{aligned} x_n^A(t) &\approx \delta^- \left\{-\frac{2}{\sqrt{3}} + 2(-1)^n \cos\left(\omega_b t\right)\right\} \sqrt{\frac{3(\omega_b - \omega)}{\widetilde{h}}} \tanh\left[\sqrt{\frac{3(\omega_b - \omega)}{\omega''}}(n - n_0)\right] \\ y_n^A(t) &\approx \delta^- \left\{-\frac{2}{\sqrt{3}} + \frac{2(-1)^n\kappa}{\kappa - \rho\omega^2} \cos\left(\omega_b t\right)\right\} \sqrt{\frac{3(\omega_b - \omega)}{\widetilde{h}}} \tanh\left[\sqrt{\frac{3(\omega_b - \omega)}{\omega''}}(n - n_0)\right], \end{aligned} \tag{4.47}$$

where we have converted μ and ε into a new single parameter $\omega_b = \omega - \frac{1}{3}\mu\varepsilon^2$ measuring the breather frequency. Choosing $n_0 = 0$ in (4.47) results in a *site-centered* solution, whereas the *bond-centered* solution corresponds to $n_0 = 1/2$. When ω_b is close enough to ω, the ansatz (4.47) with $t = 0$ can be used as an initial seed for a Newton-type iteration to compute the numerically exact stationary dark breather solutions of the discrete system (4.37) of both site-centered and bond-centered type. Notice that although the continuum envelope approximation developed here permits an arbitrary selection of n_0, discrete models typically only support such site- and bond-centered solutions with the corresponding selection of n_0 discussed above; see e.g. [27].

4.5 WEAKLY AND STRONGLY NONLINEAR DARK BREATHERS

We now use the Newton-type algorithm described in Sec. 3.5.2 with the initial seed (4.47) to compute the numerically exact dark stationary breather solutions of the system (4.37) with periodic boundary conditions.

In what follows we set $\alpha = 3/2$, $\kappa = 1$ and $\delta_0 = 4/9$. Also, the vertical center C_x (recall (3.92)) is set to be approximately zero. The renormalized ℓ^2 norm of $Z(0)$ can be defined as

$$||Z(0)||^2_{\widetilde{\ell}^2} = \sum_n K_x^2 - |x_n(0) - C_x|^2 + \sum_n K_y^2 - |y_n(0) - C_y|^2. \tag{4.48}$$

We first consider the mass ratio $\rho = 1/3$, so that the linear frequencies of plane waves at the $\theta = \pi$ edge of optical and acoustic branches are $\omega_{opt} = 2.4495$ and $\omega_{acs} = 1.4142$, respectively. We choose a value of ω_b that is slightly smaller than but close enough to ω_{opt} or ω_{acs} to obtain a good initial seed with a small amplitude. Once the Newton-type solver converges to an exact dark breather solution, we use the method of continuation to obtain an entire family of dark breathers that corresponds to different values of ω_b. Sample profiles of both bond-centered and site-centered dark breather solutions with frequency $\omega_b = 2.42$, along with their corresponding initial seeds from the NLS approximation (4.47) are shown in Fig. 4.11. In the left plots in Fig. 4.12, we show the renormalized ℓ^2 norm of the numerically exact bond-centered dark breathers that bifurcate from $\theta = \pi$ edge of the optical branch. The solutions do not exist for arbitrary values of ω_b; rather, there is a turning point at $\omega_b \approx 2.37$. We are able to continue the relevant solution branch past this turning point, obtaining dark breather solutions making up the top part of the branch with increasing amplitude as ω_b increases. Therefore, dark breathers above the turning point can be regarded as *strongly nonlinear* solutions, while solutions along the bottom part are *weakly nonlinear*. As explained in the next section, solutions along the segments marked by red dots possess real instability, and the ones along the blue segments do not.

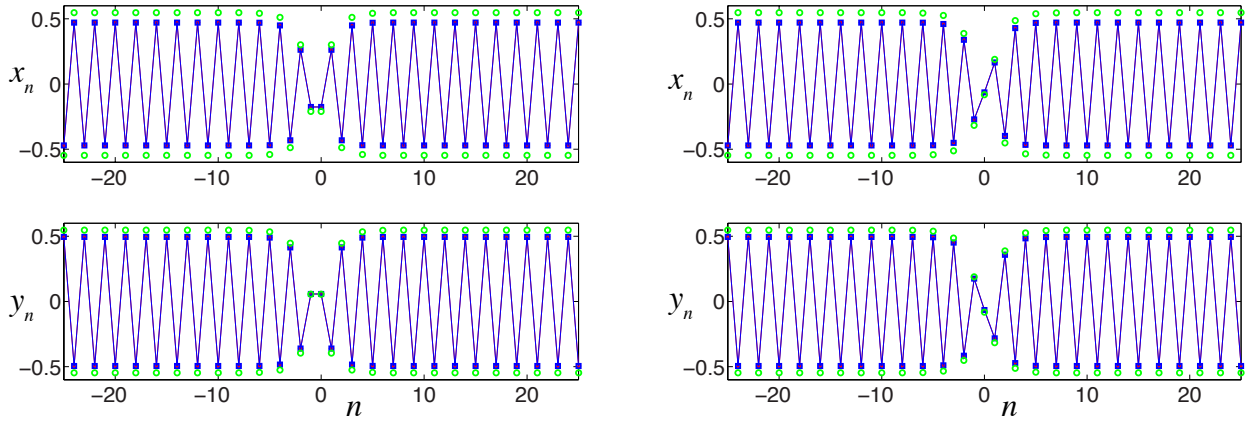

Figure 4.11: Left plot: a bond-centered dark breather solution (connected stars) with frequency $\omega_b = 2.42$. Squares represent the strain profile after integration over T_b. Circles represent the initial profiles computed from the approximation (4.47). Right plot: a site-centered solution. The relative errors $E_b(T_b)$ of both solutions are less than 3×10^{-9}. Here $\alpha = 3/2$, $\kappa = 1$, $\delta_0 = 4/9$ and $\rho = 1/3$.

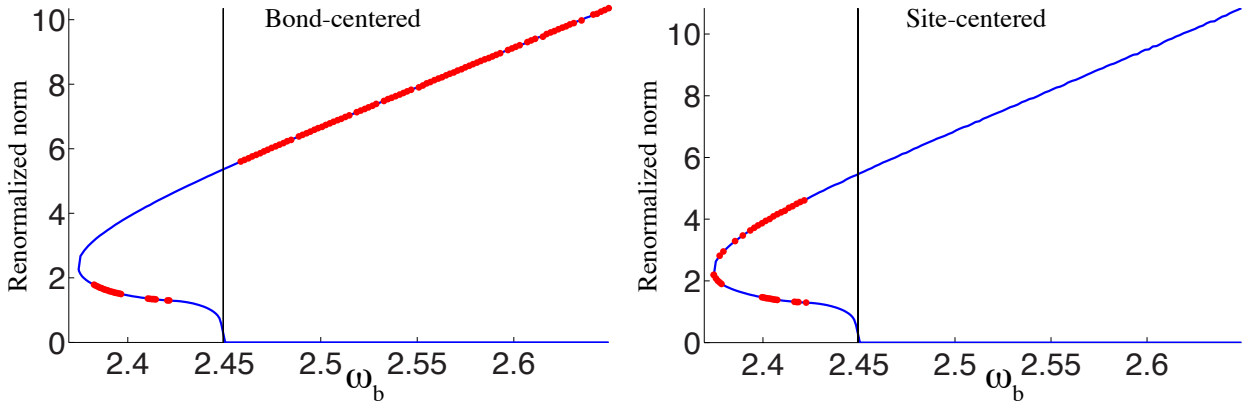

Figure 4.12: Left plot: renormalized ℓ^2 norm of the bond-centered dark breather solution versus frequency ω_b with the vertical center $C_x = 0$. The black vertical line shows the edge of the optical branch $\omega_{opt} = 2.4495$. Right plot: same as the left, but for site-centered solution. Regions where a real instability is present are indicated by red dots. Here $\alpha = 3/2$, $\kappa = 1$, $\delta_0 = 4/9$ and $\rho = 1/3$.

4.6 LINEAR STABILITY ANALYSIS

We now examine the linear stability of the obtained dark breather solutions via the standard Floquet analysis introduced in Sec. 3.6.1. The moduli of Floquet multipliers of the site-centered and bond-centered solutions, for both strongly and weakly nonlinear types, are shown in Fig. 4.13, along with the numerically computed Floquet spectrum corresponding to the sample breather profile at $\omega_b = 2.42$. As in Sec. 3.6.1, we observe real and oscillatory instability modes.

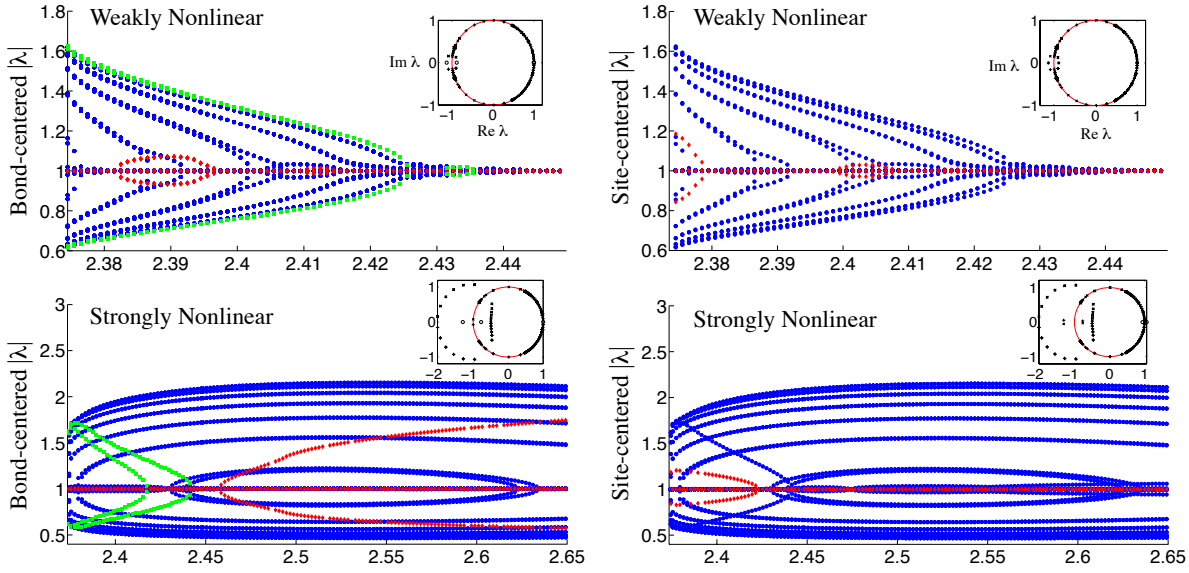

Figure 4.13: Moduli of Floquet multipliers versus frequency ω_b for weakly nonlinear (top) and strongly nonlinear (bottom) types. Recall that these refer to solutions below and above the turning point in Fig. 4.12, respectively. Left and right plots corresponds to bond- and site-centered dark breathers respectively. Blue dots represent $\mathrm{Im}(\lambda) \neq 0$, red diamonds represent $\mathrm{Im}(\lambda) = 0, \lambda > 0$ and green squares represent $\mathrm{Im}(\lambda) = 0, \lambda < 0$. The Floquet multipliers for $\omega_b = 2.42$ in the complex plane are shown in the respective insets. Here $\alpha = 3/2$, $\kappa = 1$, $\delta = 4/9$ and $\rho = 1/3$.

Numerical results suggest that both bond-centered and site-centered weakly nonlinear solutions are stable at the beginning of the continuation procedure, as shown in the top panels of Fig. 4.13, similarly to what was found in the homogeneous granular chain [18]. However, as the corresponding frequency decreases, the amplitude of the breathers increases and they start to exhibit oscillatory instabilities. These marginally unstable modes remain weak until ω_b reaches $\omega_b \approx 2.4255$ in the left plot of Fig. 4.14. The relative error $E_b(1200)$ defined in

(3.94) stays below 2×10^{-4} when $2.4255 \leq \omega_b \leq \omega_{opt}$ and increases dramatically at smaller frequencies. A representative space-time evolution diagram of bond-centered dark breather solution at $\omega_b = 2.4255$ is shown in the right plots of Fig. 4.14, and the time evolution of site-centered solution is similar. This suggests that the dark breathers solutions of both types with frequency close to the linear frequency ω_{opt} are long-lived and have marginal oscillatory instability. As ω_b further decreases, we observe the emergence of many new and stronger modes of oscillatory instability, with Floquet multipliers distributed symmetrically outside the unit circle around -1. In addition, for bond-centered dark breathers, pairs of real Floquet multipliers collide at -1 and move in the opposite directions as ω_b decreases. This is associated with a period-doubling instability. Moduli of these multipliers are indicated by the green squares in Fig. 4.13 and in the left plot of Fig. 4.14.

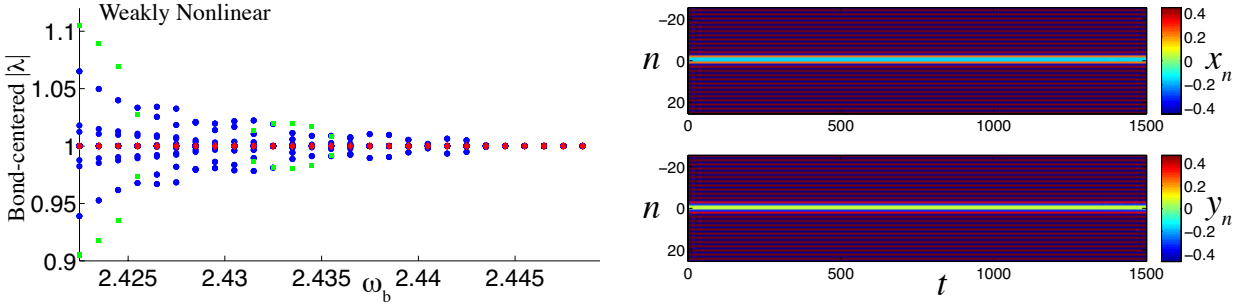

Figure 4.14: Left plot: moduli of Floquet multipliers of bond-centered breathers for frequencies $2.4235 \leq \omega_b \leq \omega_{opt}$. Right plots: contour plot of the time evolution of the bond-centered solution for $\omega_b = 2.4255$. The color bar corresponds to the magnitude of the strain x_n (top) and y_n (bottom). The breather appears to be very long-lived despite the instability suggested by the left panel of the figure. Here $\alpha = 3/2$, $\kappa = 1$, $\delta = 4/9$ and $\rho = 1/3$.

The emergence of many unstable quartets suggests that both bond-centered and site-centered solutions have strong modulational instabilty of the background, which leads to the breakdown of the dark breather structure, accompanied, as shown in Fig. 4.15, by a chaotic evolution of both solutions after a short time. The same phenomenology (dismantling of the breather and chaotic evolution) also takes place for all strongly nonlinear dark breather solutions. For this reason, in the bifurcation diagram of Fig. 4.12 only real instabilities are indicated. It is interesting that the strongly nonlinear bond-centered solutions typically exhibit real instability at frequencies greater than ω_{opt}, while the real instability emerges

only when ω_b is less than ω_{opt} for the site-centered ones.

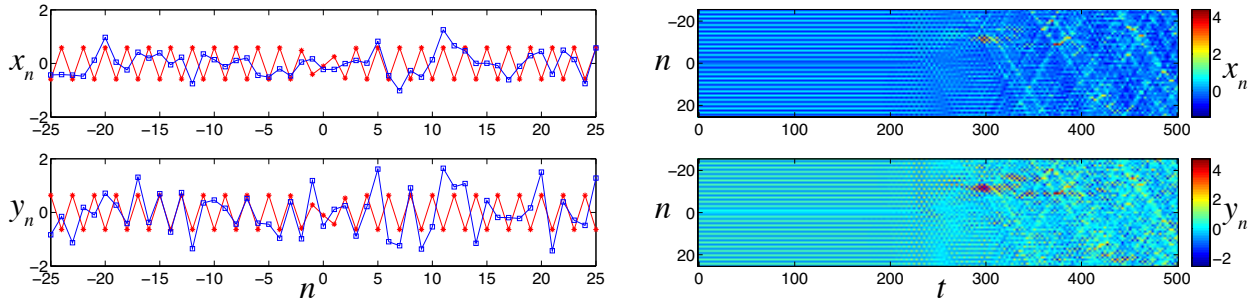

Figure 4.15: Left plot: snapshots of the strain profile of site-centered dark breather solution at time $t = 0$ (connected red stars) and $t = 500$ (connected blue squares). Right plots: contour plot of the time evolution of the site-centered solution for $\omega_b = 2.40$. The color bar corresponds to the magnitude of the strain x_n (top) and y_n (bottom). Here $\alpha = 3/2$, $\kappa = 1$, $\delta = 4/9$ and $\rho = 1/3$. Clearly, the dark breather structure gets destroyed as a result of its spectral instability.

We now examine the stability properties of dark breathers that bifurcate from the $\theta = \pi$ edge of the acoustic branch, where the linear frequency is $\omega_{acs} = 1.414$. The bifurcation diagram for solutions of the bond-centered type and the corresponding diagrams of the moduli of the Floquet multipliers versus frequency are shown in Fig. 4.16. We observe that the distribution of positive real Floquet multipliers in the top right plot (weakly nonlinear dark breathers) follows a pattern similar to the one for such breathers bifurcating from the optical branch (top left plot of Fig. 4.13). Note also that the large arc for strongly nonlinear solutions in the bottom right plot of Fig. 4.16 suggests that these dark breathers exhibit not only an oscillatory instability but also a real instability, which possesses a considerably larger growth rate than the oscillatory one.

We now investigate the effect of the mass ratio on the linear stability of the solutions. We first consider the mass ratio $\rho = 1$ and keep all other parameters the same as in the previous simulation. Using the continuation procedure, we obtain a family of dark breathers bifurcating from the optical branch edge $\omega_{opt} = 2.2882$. As shown in Fig. 4.17, the bifurcation diagrams of the renormalized ℓ^2 norm of these solutions are similar to the $\rho = 1/3$ case. The moduli of Floquet multipliers of the weakly and strongly nonlinear dark breathers solutions for both bond-centered and site-centered types, are shown in Fig. 4.18. We observe that the magnitude of the Floquet multipliers corresponding to the oscillatory instability is much weaker than in the $\rho = 1/3$ case. In addition, the real instability becomes more

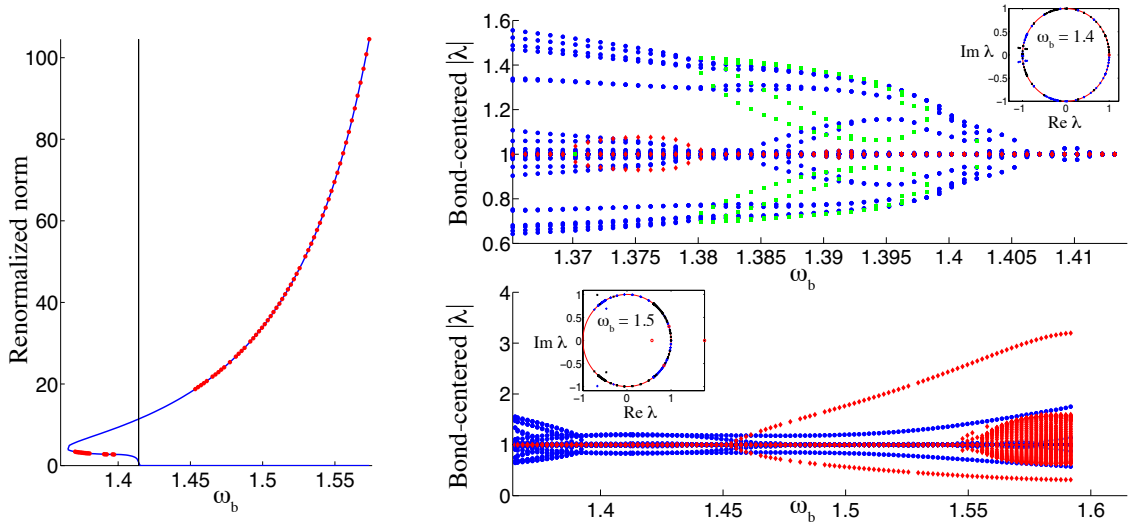

Figure 4.16: Left panel: renormalized ℓ^2 norm of the bond-centered solution bifurcating from the acoustic branch versus ω_b with the vertical center $C_x = 0$. The black vertical line shows the $\theta = \pi$ edge of the acoustic branch $\omega_{acs} = 1.414$. Right panel: moduli of the Floquet multipliers versus frequency ω_b for weakly nonlinear (top) and strongly nonlinear (bottom) types. Insets: the Floquet multipliers in the complex plane. Here $\alpha = 3/2$, $\kappa = 1$, $\delta = 4/9$ and $\rho = 1/3$.

significant than the oscillatory one at some frequencies, resulting in not only shorter lifetime of the solutions, but also setting the dark breathers in motion. A representative space-time evolution diagram for weakly nonlinear bond-centered dark breather solution of frequency $\omega_b = 2.207$ is shown in Fig. 4.19. Note that the positive Floquet multipliers again exhibit the same bifurcation structure as in the previous results.

We also investigate the case of a large mass ratio, $\rho = 10$. The continuation procedure works quite well for dark breathers bifurcating from the optical branch but we encountered difficulty doing computations for the acoustic band due to the rapidly growing amplitude of those solutions as ω_b decreases. As a result, only dark breathers with frequencies very close to ω_{acs} are obtained. The diagrams of the moduli of the Floquet multipliers versus frequency for the dark breathers bifurcating from the optical branch are shown in Fig. 4.20. We observe that the magnitude of Floquet multipliers corresponding to oscillatory instability becomes much larger again than in the $\rho = 1$ case but smaller than in the $\rho = 1/3$ case, which suggests that the significance of oscillatory instability does not depend monotonically on the

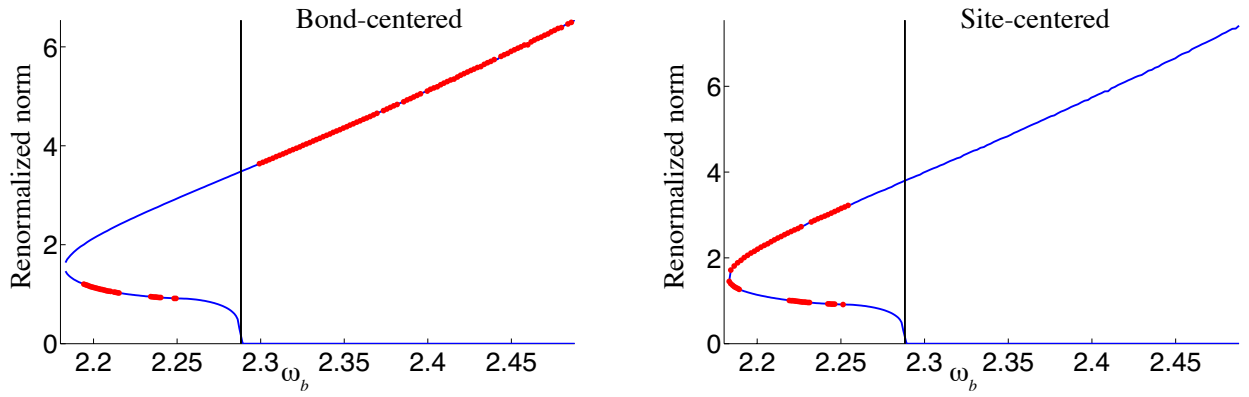

Figure 4.17: Left plot: renormalized ℓ^2 norm of the bond-centered dark breather solution bifurcating from the optical brach versus frequency ω_b with the vertical center $C_x = 0$. The black vertical line shows the edge of the optical branch $\omega_{opt} = 2.2282$. Right plot: same as the left, but for site-centered solution. Portions of the curve where a real instability is present are indicated by red dots. Here $\alpha = 3/2$, $\kappa = 1$, $\delta_0 = 4/9$ and $\rho = 1$.

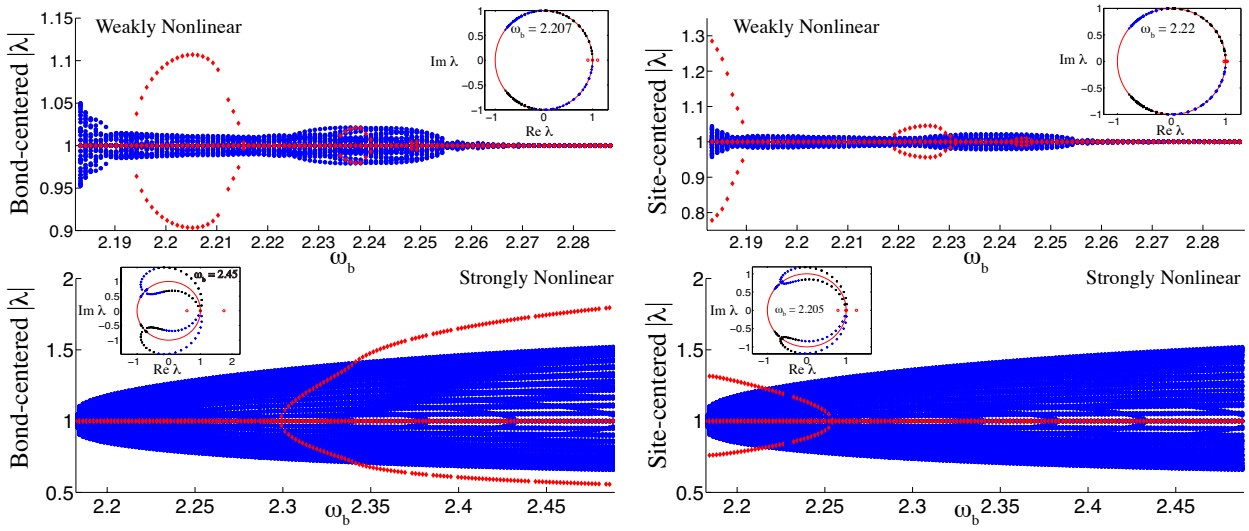

Figure 4.18: Results of the simulation with the same parameters as in Fig. 4.13 except for $\rho = 1$. Here the corresponding dark breathers bifurcate from the optical branch.

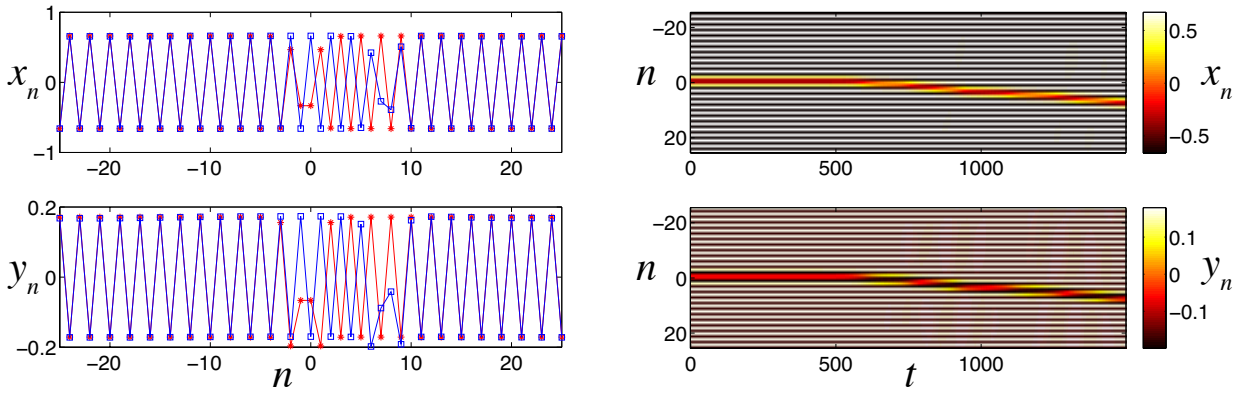

Figure 4.19: Left panel: sample profiles (connected stars) of bond-centered dark breathers at the frequency $\omega_b = 2.207$. Connected squares represent strain profiles after integration over $526T_n \approx 1500$. Right panel: contour plots of the time evolution of the bond-centered solution for $\omega_b = 2.207$. The color bar corresponds to the magnitude of the strain x_n (top) and y_n (bottom). Clearly, the instability of the stationary dark breather solutions sets it into motion.

mass ratio. Furthermore, in this case, the oscillatory instability appears to set in already in the immediate vicinity of the linear limit at the edge of the optical band. Considering now the case of a very small mass ratio, $\rho = 0.1$, we find that in contrast to the large mass ratio like $\rho = 10$, we can only obtain dark breathers bifurcating from the acoustic branch and corresponding to a wide range of frequencies; see Fig. 4.21. It is surprising that the real instability of some of the weakly nonlinear solutions is again more significant than the oscillatory instability, which is also a feature for the optical weakly nonlinear solutions at $\rho = 1$. Again, similar patterns of the distribution of the positive real Floquet multipliers suggest that their bifurcation structure remain unaffected by different mass ratios.

4.7 CONCLUDING REMARKS

In this chapter, we investigated discrete breathers in a precompressed locally resonant granular chain. The precompression effectively suppresses the fully nonlinear character of the Hertzian interactions and leads to the weakly nonlinear dynamics in the small-amplitude limit. Following the approach developed in [18, 21] for two limiting cases of the present

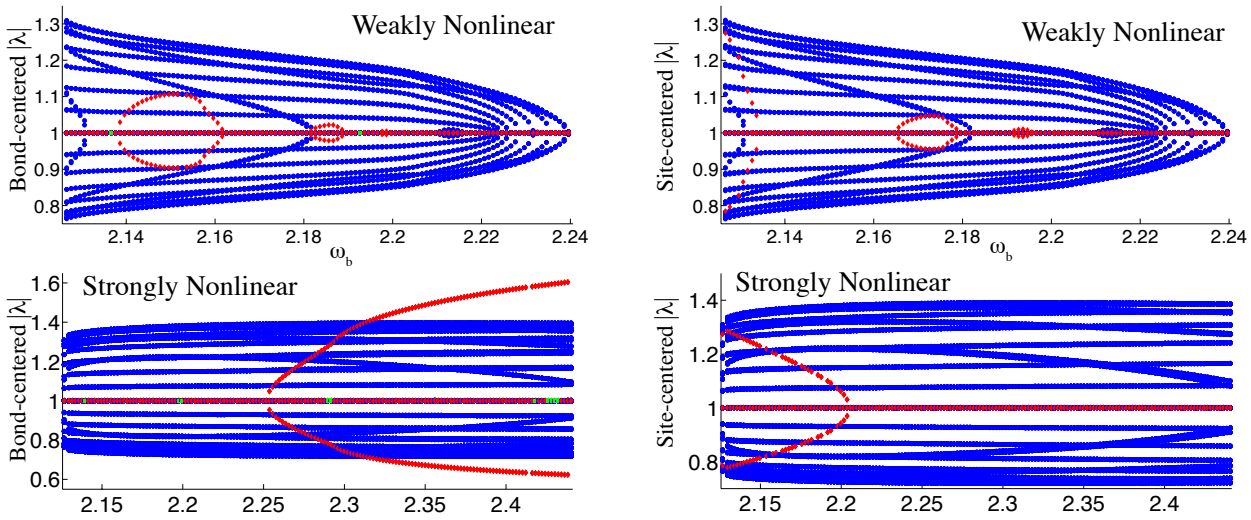

Figure 4.20: Results of the simulation with the same parameters as in Fig. 4.13 except for $\rho = 10$. Here the corresponding dark breathers bifurcate from the optical branch.

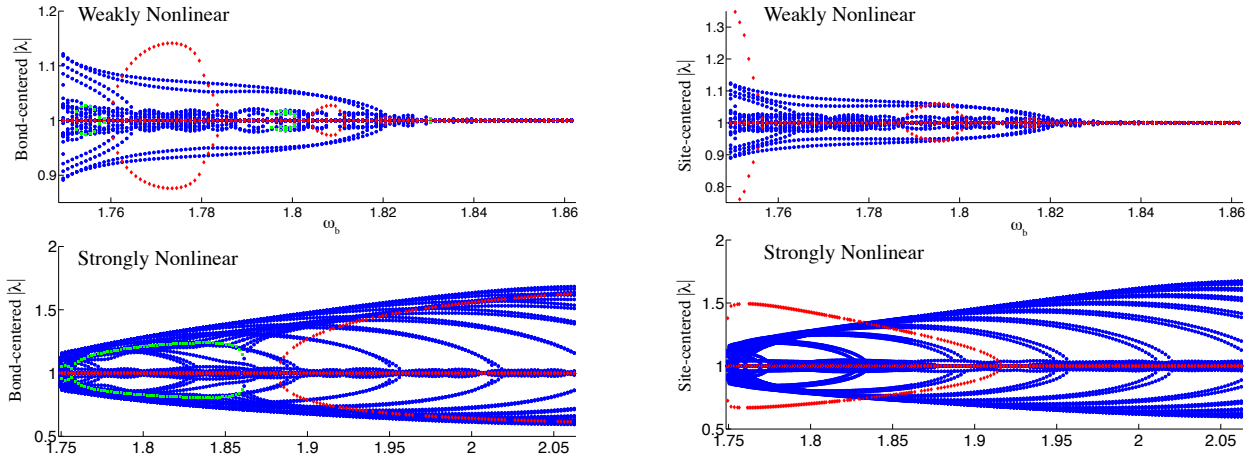

Figure 4.21: Results of the simulation with the same parameters as in Fig. 4.13 except for $\rho = 1/10$. Here the corresponding dark breathers bifurcate from the acoustic branch.

model and adopting the multiscale asymptotic technique [34–36], we derived modulation equations that reduce to the NLS equation at finite mass ratio.

The focusing NLS equations was then used to investigate the moving bright breather solution of the system at finite mass ratios. We showed numerically that these equations can successfully capture the dynamics of small-amplitude moving optical bright breathers on a long but finite time scale at some wave numbers and various mass ratios. At some other wave numbers for the optical branch and in the acoustic case the NLS solution does not capture numerically observed phenomena, including eventual formation and steady motion of smaller breathers that detach from the tail of the initial breather and are associated with the other dispersion branch. Contrary to the more standard dimer case, this resonator problem appears to possess bright breathers in the neighborhood of $\theta = 0$ wave numbers of the optical band. However, that very point is found to be singular, and breathers in its immediate vicinity do not appear to be robust, while bright breathers at larger wave numbers that are below a certain threshold are found to propagate nearly undistorted in the resonator chain at any mass ratio.

In addition, we analyzed the defocusing case of NLS equations and used the analytical solutions of these equations to construct approximate stationary dark breather solutions. Using this approximation as an initial condition for a continuation procedure based on a Newton-type algorithm, we obtained both weakly and strongly nonlinear dark breather solutions of both the site-centered and bond-centered families for a wide range of frequencies. We then studied linear stability of the obtained solutions. The results revealed that only small-amplitude weakly nonlinear solutions with frequencies very close to the linear frequencies of the system are stable (for typical values of the resonator mass ρ). In contrast, large-amplitude dark breather solutions exhibit either real or oscillatory instabilities (or both). In particular, the strongly nonlinear dark breathers have a very unstable background, leading to the dismantling of their structure, accompanied by a chaotic evolution after a short time. We also observed the potential of steady motion of dark breathers due to a long-time evolution subject to real instability. Finally, we showed that the mass ratio strongly affects the strength of the oscillatory instability of the dark breather solutions, but its influence on the distribution patterns of positive real Floquet multipliers is less pronounced.

Future challenges include the rigorous proof of the existence of long-lived or exact small-amplitude moving bright breathers and static dark breathers, the analysis of their modulational stability and comparison with the numerical results presented here. On the experimental side, it will be interesting to investigate whether it is possible to generate either (approximate) moving bright breathers, perhaps actuating one boundary at a suitable, near-band-edge frequency, or stationary dark breathers in a slightly damped finite locally resonant chain driven at the ends in a way similar to [18, 19] but using the woodpile setup [32].

APPENDIX A

ANALYTICAL EXPRESSION FOR $\mathcal{J}$

Recall that the integral form of $\mathcal{J}(k_\xi, n)$ is given by (2.17). Note that $\mathcal{J}(k_\xi, n)$ has the symmetry property that for any integer n

$$\mathcal{J}(k_\xi, -n) + \mathcal{J}(k_\xi, n+1) = 0, \tag{A.1}$$

and hence only the case $n \geq 1$ needs to be considered. Following [10], we rewrite (2.17) as an integral over the unit circle in the complex plane:

$$\mathcal{J}(k_\xi, n) = \oint_{|\zeta|=1} \frac{(1-\zeta)\zeta^{-n}}{i(\zeta^2 - 2\lambda\zeta + 1)} d\zeta, \tag{A.2}$$

where $\zeta = e^{i\kappa}$ and $\lambda(k_\xi)$ is given by (2.21). Applying residue theorem to the integration in (A.2), we obtain an analytic expression:

$$\mathcal{J}(k_\xi, n) = \begin{cases} \pi(1 + \sqrt{\frac{\lambda-1}{\lambda+1}})(\lambda - \sqrt{\lambda^2-1})^{-n}, & \lambda < -1, \\ \pi(1 \mp i\sqrt{\frac{1-\lambda}{1+\lambda}})(\lambda \mp i\sqrt{1-\lambda^2})^{-n}, & |\lambda| < 1, \quad k_\xi \lessgtr 0. \\ \pi(1 + \sqrt{\frac{\lambda-1}{\lambda+1}})(\lambda + \sqrt{\lambda^2-1})^{-n}, & \lambda > 1 \end{cases} \tag{A.3}$$

We remark that the derivation of (A.3) for $|\lambda| < 1$ involves the poles $\zeta = \lambda \pm i\sqrt{1-\lambda^2}$ located on the unit circle $|\zeta| = 1$ (the path of integration in (A.2)), which correspond to the lattice waves emitted by the moving step. To resolve these singularities in a way that selects physically relevant solutions, we follow the approach in [10] and introduce a small damping contribution, which corresponds to replacing λ in (2.21) by $\lambda = \lambda_0 + i\gamma V k_\xi/2$, where λ_0 is

given by the right hand side of (2.21), $\gamma > 0$ is a small damping coefficient, and we recall that $V > 0$. Then for $|\lambda_0| < 1$ one of the poles shifts slightly outside the unit circle, while the other one shifts slightly inside the circle, depending on the sign of k_ξ. In the limit when $\gamma \to 0$ and thus $\lambda \to \lambda_0$, this means that the unit circle should be indented inward around $\zeta = \lambda - i\sqrt{1-\lambda^2}$ and outward around $\zeta = \lambda + i\sqrt{1-\lambda^2}$ when $k_\xi < 0$. Meanwhile, for $k_\xi > 0$ the opposite is true: the path of integration is indented inward around $\zeta = \lambda + i\sqrt{1-\lambda^2}$ and outward around $\zeta = \lambda - i\sqrt{1-\lambda^2}$. This ensures the selection of the relevant pole in the residue theorem calculation and results in a physically meaningful distribution of lattice waves in the final solution, in the sense that it is not destroyed in the presence of small damping. We observe that in [37], the expression corresponding to (A.3) has $\lambda'(k_\xi) \gtrless 0$ instead of $k_\xi \lessgtr 0$, which is equivalent in the region $V > V_1$ above the first resonance velocity that is studied in [37]. However, a formal extension of the formula in [37] to $V < V_1$ does not satisfy the above zero-damping limit criterion.

Using

$$\mathcal{S}(k_\xi, n) \;=\; \frac{\mathcal{J}(k_\xi, n+1) - \mathcal{J}(k_\xi, n)}{2\pi}, \tag{A.4}$$

(A.1) and (A.3), we then obtain the analytic expression (2.20) for $\mathcal{S}(k_\xi, j)$.

APPENDIX B

EQUILIBRIUM STATES AND THE PEIERLS STRESS

In this appendix, we consider the equilibrium states ($V = 0$), which are governed by the system of difference equations

$$\chi(u_{m+1,n} - 2u_{m,n} + u_{m-1,n}) + \Phi'(u_{m,n+1} - u_{m,n}) - \Phi'(u_{m,n} - u_{m,n-1}) = 0 \tag{B.1}$$

and correspond to the configuration like the one shown in Figure 2.2, i.e. satisfy

$$y_{m,n} < -\delta/2, \quad n \geq 2, \qquad y_{m,n} > \delta/2, \quad n \leq 0,$$

$$y_{m,1} \geq \delta/2, \quad m \leq 0, \qquad y_{m,1} \leq -\delta/2, \quad m \geq m_s + 1, \tag{B.2}$$

and

$$|y_{m,1}| \leq \delta/2, \quad m = 1, \ldots, m_s, \quad \text{if } m_s \geq 1,$$

where m_s is the number of $n = 1$ vertical bonds in the spinodal region. Under these assumptions, (B.1) become

$$\begin{aligned} &\chi(u_{m+1,n} + u_{m-1,n} - 2u_{m,n}) + u_{m,n+1} + u_{m,n-1} - 2u_{m,n} \\ &= -2\delta_{n,0} + (\delta_{n,0} - \delta_{n,1}) \left\{ 2\theta(-m) + \left(1 + \frac{2}{\delta}(u_{m,1} - u_{m,0})\right) [\theta(m_s - m) - \theta(-m)] \right\}, \end{aligned} \tag{B.3}$$

where the unit function satisfies $\theta(0) = 1$.

If $m_s = 0$, the displacement field can be obtained using the lattice Green's function as in [38, 79], yielding

$$u_{m,n} = \frac{1}{\pi\chi}\int_0^\pi \mathfrak{J}(m)\frac{\cos(n-1)\kappa - \cos n\kappa}{\sinh s}d\kappa, + \begin{cases} n(\sigma-1), & n \geq 0 \\ n(\sigma+1), & n \leq -1. \end{cases} \tag{B.4}$$

where $s \geq 0$ satisfies $\cosh s = (\chi + 1 - \cos\kappa)/\chi$ and

$$\mathfrak{J}(m) = \begin{cases} \frac{e^s+1-e^{ms}}{e^s-1}, & m < 0 \\ \frac{e^{(1-m)s}}{e^s-1}, & m \geq 0. \end{cases} \tag{B.5}$$

One can show that the solution (B.4) exists if and only if the applied stress is within the *trapping region* $|\sigma| \leq \sigma_P$, where

$$\sigma_P = 1 - \frac{\delta}{2} - \frac{2}{\pi}\int_0^\pi \mathfrak{J}(1)\frac{\cosh s - 1}{\sinh s}d\kappa.$$

is the Peierls stress at which $y_{1,1} \equiv u_{1,1} - u_{1,0} = -\delta/2$. For example, at $\chi = 1$ we obtain $\sigma_P = (1-\delta)/2$.

Since the Peierls stress must be non-negative, the equilibrium solutions with no spinodal bonds exist only for sufficiently narrow spinodal regions, e.g. $0 \leq \delta \leq 1$ for $\chi = 1$. In particular, at $\delta = 0$ (B.4) yields the single stable equilibrium state with the assumed configuration for σ inside the trapping region. For $0 < \delta < 2$ there are solutions with at least one spinodal bond. In general, this problem can be reduced to the one analyzed in [60] for a screw dislocation. Here we simply summarize the results. Let $\alpha(N)$ be the largest eigenvalue of the $N \times N$ matrix $\mathbf{A}$ with the entries $a_{i,j} = \mathcal{A}(i-j)$, where

$$\mathcal{A}(p) = \frac{1}{\pi}\int_0^\pi e^{-|p|s}\frac{\cosh s - 1}{\sinh s}d\kappa$$

and we set $\alpha(0) = 0$. Then for $0 < \delta < 2$ and $|\sigma| < \sigma_P$, there are two equilibrium states, a stable state with m_s spinodal bonds and an unstable state with $m_s + 1$ spinodal bonds, where m_s is uniquely determined from the inequality

$$\alpha(m_s) < \frac{\delta}{2} < \alpha(m_s + 1). \tag{B.6}$$

The two equilibria merge into a saddle point at $\sigma = \sigma_P$. For $m_s \geq 1$ the displacement field is then given by

$$u_{m,n} = \sum_{j=1}^{m_s} \left(1 + \frac{2}{\delta} Y_j\right) \frac{1}{\pi\chi} \int_0^\pi e^{-|m-j|s} \frac{\cos(n-1)\kappa - \cos n\kappa}{2\sinh s} d\kappa$$
$$+ \frac{1}{\pi\chi} \int_0^\pi \mathfrak{J}(m) \frac{\cos(n-1)\kappa - \cos n\kappa}{\sinh s} d\kappa + \begin{cases} n(\sigma - 1), & n \geq 0 \\ n(\sigma + 1), & n \leq -1. \end{cases} \tag{B.7}$$

where $Y_j \equiv y_{j,1}$, $j = 1, ..., m_s$ are the strains in the spinodal bonds found by solving the linear system

$$Y_i = \frac{2}{\delta} \sum_{j=1}^{m_s} \mathcal{A}(i-j) Y_j + \frac{2}{\pi} \int_0^\pi \left[\mathfrak{J}(i) + \frac{1}{2} \sum_{j=1}^{m_s} e^{-|i-j|s}\right] \frac{\cosh s - 1}{\sinh s} d\kappa + \sigma - 1, \quad i = 1, \ldots, m_s. \tag{B.8}$$

To determine the Peierls stress, which corresponds to $y_{m_s+1,1} = -\delta/2$ in a stable equilibrium, define

$$N_S = \begin{cases} N/2 & \text{if} \quad \text{mod } (N,2) = 0 \\ (N+1)/2 & \text{if} \quad \text{mod } (N,2) = 1, \end{cases}$$

$N_A = N - N_S$,

$$\beta(N,j) = \begin{cases} 1/2 & \text{if} \quad \text{mod } (N,2) = 0 \text{ and } j = N_S \\ 1 & \text{otherwise,} \end{cases}$$

and let $\mathbf{B}_S(N)$ be the $N_S \times N_S$ matrix with the entries

$$(b_S)_{i,j} = \frac{\delta}{2}\delta_{i,j} - [\mathcal{A}(i-j) + \mathcal{A}(N+1-i-j)]\beta(N,j),$$

while $\mathbf{B}_A(N)$ is the $N_A \times N_A$ matrix with the entries

$$(b_A)_{i,j} = \frac{\delta}{2}\delta_{i,j} - [\mathcal{A}(i-j) - \mathcal{A}(N+1-i-j)].$$

We then obtain [60]

$$\sigma_P = -\frac{\det \mathbf{B}_S(m_s)}{\det \mathbf{B}_A(m_s)} \cdot \frac{\det \mathbf{B}_S(m_s+1)}{\det \mathbf{B}_A(m_s+1)}, \tag{B.9}$$

where for $m_s = 1$ and $m_s = 0$ the zero-size determinants equal 1. Figure B1 shows the dependence of Peierls stress on the width δ of the spinodal region at different χ. Note that

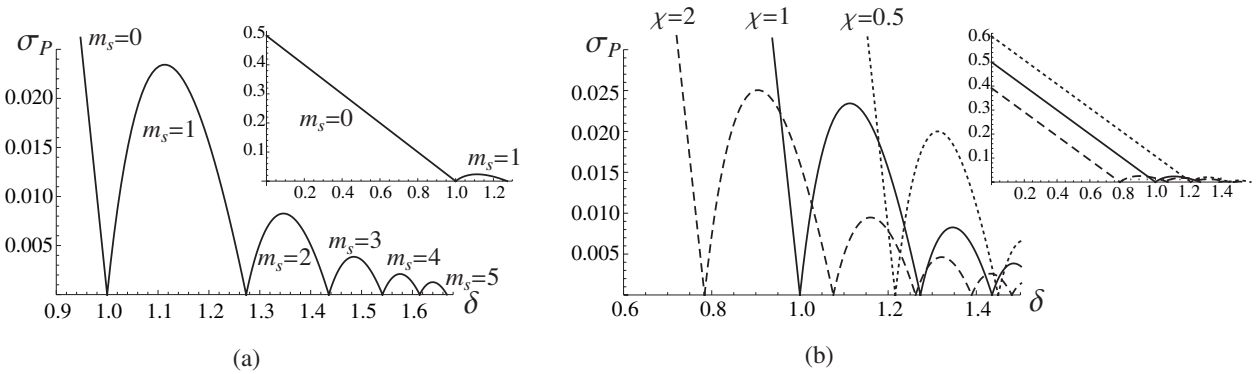

Figure B1: (a) Dependence of the Peierls σ_P stress on the width δ of the spinodal region at $\chi = 1$. Here m_s is the number of spinodal $n = 1$ vertical bonds in a stable equilibrium configuration, while an unstable equilibrium has $m_s + 1$ such bonds. (b) $\sigma_P(\delta)$ at $\chi = 2$ (dashed curve), $\chi = 1$ (solid curve) and $\chi = 0.5$ (dotted curve). Insets show the Peierls stress at smaller δ.

the dependence on δ is no longer linear when spinodal bonds exist ($m_s \geq 1$). At $\delta = 2\alpha(m_s)$, $m_s = 1, 2, \ldots$, there is no trapping region, i.e. $\sigma_P = 0$. This is an artifact of the trilinear model and is not generic. Similar results were obtained for the Frenkel-Kontorova model in [80, 81].

APPENDIX C

DERIVATION OF THE MODULATION EQUATIONS

In this appendix, we show the details of the derivation of the modulation equations (4.14) and (4.15). In what follows, we will use the abbreviation $\sum_{k,j}$ for the summation over $k \in \mathbb{N}_1$ and $j \in \mathbb{Z}$, $|j| \leq k$ in (4.13). The ansatz defined in (4.13) will be denoted by $U_n^A = u_n$ and $V_n^B = v_n$. After substituting (4.13) into (4.2), we find that the right hand side of the second equation in (4.2) reads

$$-\frac{\kappa}{\rho}\sum_{k,j}\varepsilon^k[B_{k,j}(\tau,\xi) - A_{k,j}(\tau,\xi)]E(t,n)^j, \tag{C.1}$$

and its left hand side is

$$\begin{aligned}\ddot{V}_n^B(t) := \sum_{k,j}\varepsilon^k[-(j\omega)^2 B_{k,j} + 2\varepsilon ij\omega c\partial_\xi B_{k,j} + \varepsilon^2(c^2\partial_\xi^2 B_{k,j} - 2ij\omega\partial_\tau B_{k,j}) \\ -2\varepsilon^3 c\partial_\xi\partial_\tau B_{k,j} + \varepsilon^4\partial_\tau^2 B_{k,j}]E^j(t,n).\end{aligned} \tag{C.2}$$

To match the coefficients of each $\varepsilon^k E^j(\tau,\xi)$ term on both sides, we require that

$$\varepsilon^1 E^0: \quad 0 = -\frac{\kappa}{\rho}(B_{1,0} - A_{1,0}) \quad \Rightarrow \quad B_{1,0} = A_{1,0}, \tag{C.3}$$

$$\varepsilon^1 E^1: \quad -\omega^2 B_{1,1} = -\frac{\kappa}{\rho}(B_{1,1} - A_{1,1}) \quad \Rightarrow \quad (\kappa - \rho\omega^2)B_{1,1} = \kappa A_{1,1}, \tag{C.4}$$

$$\varepsilon^2 E^1: \quad -\omega^2 B_{2,1} + 2i\omega c\partial_\xi B_{1,1} = -\frac{\kappa}{\rho}(B_{2,1} - A_{2,1}), \tag{C.5}$$

$$\varepsilon^2 E^2: \quad -4\omega^2 B_{2,2} = -\frac{\kappa}{\rho}(B_{2,2} - A_{2,2}), \tag{C.6}$$

$$\varepsilon^3 E^0: \quad c^2\partial_\xi^2 B_{1,0} = -\frac{\kappa}{\rho}(B_{3,0} - A_{3,0}), \tag{C.7}$$

$$\varepsilon^3 E^1: \quad -\omega^2 B_{3,1} + 2i\omega c\partial_\xi B_{2,1} + c^2\partial_\xi^2 B_{1,1} - 2i\omega\partial_\tau B_{1,1} = -\frac{\kappa}{\rho}(B_{3,1} - A_{3,1}). \tag{C.8}$$

Meanwhile, the right hand side of the first equation of (4.2) can be treated as a sum of linear part $L_n(U^A, V^B)$ and nonlinear part $N_n(U^A)$, where we define

$$L_n(U^A, V^B) := \sum_{k,j} \varepsilon^k \{[2K_2(\cos j\theta - 1) - \kappa)]A_{k,j} + \kappa B_{k,j} + 2iK_2\varepsilon\partial_\xi A_{k,j} \sin j\theta + K_2\varepsilon^2\partial_\xi^2 A_{k,j} \cos j\theta + O(\varepsilon^3)\} E^j \tag{C.9}$$

and

$$\begin{aligned} N_n(U^A) := & -\varepsilon^2(K_3 s D_1 A_{1,1}^2 E^2 + c.c.) \\ & + \varepsilon^3\{2K_3 D_1 \bar{A}_{1,1}\partial_\xi A_{1,1} + (2K_3 s D_1 \bar{A}_{1,1} A_{2,2} - 3K_4 D_1^2 |A_{1,1}|^2 A_{1,1} - 2K_3 D_1 \partial_\xi A_{1,0} A_{1,1})E \\ & + [2K_3 D_1(D_1 - 3)A_{1,1}\partial_\xi A_{1,1} - 2K_3 s D_1 A_{1,1} A_{2,1}]E^2 \\ & + [2K_3 s(D_1 + s^2)A_{1,1}A_{2,2} + K_4 D_1^2(3 - D_1)A_{1,1}^3]E^3 + c.c\} + h.o.t., \end{aligned} \tag{C.10}$$

with the abbreviation h.o.t. meaning higher order terms. Here $s = 2i\sin\theta$ and $D_1 = 4\sin^2(\theta/2)$. The left hand side of the first equation of (4.2) reads

$$\ddot{U}_n^A(t) := \sum_{k,j} \varepsilon^k [-(j\omega)^2 A_{k,j} + 2\varepsilon ij\omega c\partial_\xi A_{k,j} + \varepsilon^2(c^2\partial_\xi^2 A_{k,j} - 2ij\omega\partial_\tau A_{k,j}) - 2\varepsilon^3 c\partial_\xi\partial_\tau A_{k,j} + \varepsilon^4\partial_\tau^2 A_{k,j}]E^j(t,n). \tag{C.11}$$

To match the coefficients of each $\varepsilon^k E^j(\tau,\xi)$ term on both sides, one needs

$$\varepsilon^1 E^0 : 0 = -\kappa A_{1,0} + \kappa B_{1,0} \quad \Rightarrow \quad A_{1,0} = B_{1,0}, \tag{C.12}$$

$$\varepsilon^1 E^1 : -\omega^2 A_{1,1} = (-D - \kappa)A_{1,1} + \kappa B_{1,1}, \tag{C.13}$$

$$\varepsilon^2 E^1 : -\omega^2 A_{2,1} + 2i\omega c\partial_\xi A_{1,1} = (-D - \kappa)A_{2,1} + \kappa B_{2,1} + 2iK_2\partial_\xi A_{1,1}\sin\theta, \tag{C.14}$$

$$\varepsilon^2 E^2 : -4\omega^2 A_{2,2} = (-4K_2\sin^2\theta - \kappa)A_{2,2} + \kappa B_{2,2} - K_3 s D_1 A_{1,1}^2, \tag{C.15}$$

$$\varepsilon^3 E^0 : c^2\partial_\xi^2 A_{1,0} = -\kappa A_{3,0} + \kappa B_{3,0} + K_2\partial_\xi^2 A_{1,0} + 2K_3 D_1 \bar{A}_{1,1}\partial_\xi A_{1,1} + c.c., \tag{C.16}$$

$$\begin{aligned} \varepsilon^3 E^1 : & -\omega^2 A_{3,1} + 2i\omega c\partial_\xi A_{2,1} + c^2\partial_\xi^2 A_{1,1} - 2i\omega\partial_\tau A_{1,1} = (-D - \kappa)A_{3,1} + \kappa B_{3,1} \\ & + 2iK_2\partial_\xi A_{2,1}\sin\theta + K_2\partial_\xi^2 A_{1,1}\cos\theta + 2K_3 s D_1 \bar{A}_{1,1} A_{2,2} - 3K_4 D_1^2 |A_{1,1}|^2 A_{1,1} - 2K_3 D_1 \partial_\xi A_{1,0} A_{1,1}. \end{aligned} \tag{C.17}$$

Note that both (C.3) and (C.12) yield $A_{1,0} = B_{1,0}$ but the two coefficients are not zero, in contrast with the non-resonant homogeneous chain problem ($\rho = 0$). We now derive an equation to determine them. Using (C.7) and (C.16), we obtain

$$[c^2(1+\rho) - K_2]\partial_\xi^2 A_{1,0} = 2K_3 D_1 \bar{A}_{1,1}\partial_\xi A_{1,1} + c.c., \tag{C.18}$$

where we assume the non-resonance condition (4.18).

Now combining (C.4) and (C.13) yields $\mathbf{M}\,(A_{1,1}, B_{1,1})^T = 0$, where the matrix $\mathbf{M}$ is given by (4.6). This yields that $(A_{1,1}, B_{1,1})^T$ is an eigenvector of $\mathbf{M}$ corresponding to zero eigenvalue and $A_{1,1}$ and $B_{1,1}$ are thus connected by

$$B_{1,1} = \frac{\kappa}{\kappa - \rho\omega^2} A_{1,1}. \tag{C.19}$$

Note that $\kappa - \rho\omega^2 \neq 0$, since one can check that $\omega_-^2(\theta) \leq \omega_-^2(\pi) < \kappa/\rho$ and $\omega_+^2(\theta) \geq \omega_+^2(0) > \kappa/\rho$. In addition, (C.5), (C.14) and (C.19) yield

$$\mathbf{M} \begin{pmatrix} A_{2,1} \\ B_{2,1} \end{pmatrix} = 2i\partial_\xi A_{1,1}\, W,$$

with

$$W = \begin{pmatrix} \omega c - K_2 \sin\theta \\ \omega c\kappa/(\kappa - \rho\omega^2) \end{pmatrix} \tag{C.20}$$

and the matrix $\mathbf{M}$ defined in (4.6). The range of $\mathbf{M}$ being orthogonal to

$$W^* = \begin{pmatrix} 1 - \rho\,\omega^2/\kappa \\ \rho \end{pmatrix},$$

we further obtain the compatibility condition $W^* \cdot W = 0$, which reads

$$\frac{\rho\kappa}{\rho\omega^2 - \kappa} = \frac{wc - K_2 \sin\theta}{wc}\,\frac{\kappa - \rho\omega^2}{\kappa}. \tag{C.21}$$

This yields

$$c = \frac{K_2 \sin\theta\,(\kappa - \rho\omega^2)^2}{\omega[\rho\kappa^2 + (\kappa - \rho\omega^2)^2]}, \tag{C.22}$$

and one can check that $c = \omega'(\theta)$ by differentiating the dispersion equation $\det \mathbf{M} = 0$, or

$$\omega^4 - (D + \kappa + \kappa/\rho)\omega^2 + D\kappa/\rho = 0 \tag{C.23}$$

with respect to θ.

Consider now the equations (C.6) and (C.15) for $\varepsilon^2 E^2$, which yield

$$B_{2,2} = \frac{\kappa}{\kappa - 4\rho\omega^2} A_{2,2}, \tag{C.24}$$

$$A_{2,2} = \frac{K_3 s D_1 (\kappa - 4\omega^2\rho)}{(4\omega^2 - 4K_2 \sin^2\theta - \kappa)(\kappa - 4\omega^2\rho) + \kappa^2} A_{1,1}^2. \tag{C.25}$$

This solution exists under the non-resonance condition (4.17), which is equivalent to $\omega(2\theta) \pm 2\omega(\theta) \neq 0$, as can be easily verified by substituting $\omega \to \pm 2\omega$ and $\theta \to 2\theta$ in (C.23).

In the same manner, (C.5), (C.8) and (C.17) yield the following linear system:

$$\mathbf{M} \begin{pmatrix} A_{3,1} \\ B_{3,1} \end{pmatrix} = 2i\partial_\xi A_{2,1} W + \begin{pmatrix} (c^2 - K_2\cos\theta)\partial_\xi^2 A_{1,1} \\ c^2(3\rho\omega^2 + \kappa)/(\kappa - \rho\omega^2)\partial_\xi^2 B_{1,1} \end{pmatrix} - 2i\omega \begin{pmatrix} \partial_\tau A_{1,1} \\ \partial_\tau B_{1,1} \end{pmatrix} + \begin{pmatrix} -2K_3 s D_1 \bar{A}_{1,1} A_{2,2} + 3K_4 D_1^2 |A_{1,1}|^2 A_{1,1} + 2K_3 D_1 \partial_\xi A_{1,0} A_{1,1} \\ 0 \end{pmatrix}.$$

In order for the right hand side to lie in range $\mathbf{M} = (W^*)^\perp$, and in view of (C.21), the following compatibility condition must be satisfied

$$(c^2 - K_2\cos\theta)\partial_\xi^2 A_{1,1} - 2i\omega\partial_\tau A_{1,1} - 2K_3 s D_1 \bar{A}_{1,1} A_{2,2} + 3K_4 D_1^2 |A_{1,1}|^2 A_{1,1} + 2K_3 D_1 \partial_\xi A_{1,0} A_{1,1} = \frac{\rho\kappa}{\rho\omega^2 - \kappa}\{\frac{c^2(3\rho\omega^2 + \kappa)}{(\kappa - \rho\omega^2)}\partial_\xi^2 B_{1,1} - 2i\omega\partial_\tau B_{1,1}\}.$$

Using (C.19), (C.25) and substituting $B_{1,1}$ and $A_{2,2}$ into the above identity yields the following modulation equation in terms of $A_{1,1}$ and $A_{1,0}$:

$$\begin{aligned} -2i\omega\frac{\rho\kappa^2 + (\rho\omega^2 - \kappa)^2}{(\rho\omega^2 - \kappa)^2}\partial_\tau A_{1,1} &= \left\{K_2\cos\theta - c^2[1 - \frac{3\omega^2\rho^2\kappa^2 + \rho\kappa^3}{(\rho\omega^2 - \kappa)^3}]\right\}\partial_\xi^2 A_{1,1} \\ + \left\{\frac{2K_3^2 s^2 D_1^2(\kappa - 4\omega^2\rho)}{(4\omega^2 + K_2 s^2 - \kappa)(\kappa - 4\omega^2\rho) + \kappa^2} - 3K_4 D_1^2\right\}|A_{1,1}|^2 A_{1,1} &- 2K_3 D_1 \partial_\xi A_{1,0} A_{1,1}, \end{aligned} \tag{C.26}$$

which is coupled to (C.18). Introducing

$$\gamma = \frac{(\rho\omega^2 - \kappa)^2}{\omega[\rho\kappa^2 + (\rho\omega^2 - \kappa)^2]},$$

one can show that the curvature is given by

$$\omega'' = \{K_2\cos\theta - c^2[1 - \frac{3\omega^2\rho^2\kappa^2 + \rho\kappa^3}{(\rho\omega^2 - \kappa)^3}]\}\gamma. \tag{C.27}$$

This completes the derivation of the coupled modulation equations (4.14) and (4.15).

BIBLIOGRAPHY

[1] K. Bhattacharya. *Microstructure of martensite*. Oxford University Press, Oxford, 2003.

[2] D. Bray and J. Howe. High-resolution transmission electron microscopy investigation of the face-centered cubic/hexagonal close-packed martensite transformation in Co-31.8 WtPctNi alloy: part I. plate interfaces and growth ledges. *Metll. Mater. Trans. A*, 27A:3362–3370, 1996.

[3] J. P. Hirth and J. Lothe. *Theory of dislocations*. Wiley, New York, 1982.

[4] J. P. Hirth. Ledges and dislocations in phase transformations. *Metll. Mater. Trans. A*, 25A:1885–1894, 1994.

[5] P. Müllner, V. A. Chernenko, and G. Kostorz. Stress-induced twin rearrangement resulting in change of magnetization in a Ni-Mn-Ga ferromagnetic martensite. *Scripta Mater.*, 49:129–133, 2003.

[6] R. Abeyaratne and S. Vedantam. A lattice-based model of the kinetics of twin boundary motion. *J. Mech. Phys. Solids*, 51:1675–1700, 2003.

[7] H. Tsai and P. Rosakis. Quasi-steady growth of twins under stress. *J. Mech. Phys. Solids*, 49:289–312, 2001.

[8] L. Liu, A. Vainchtein, and Y. Wang. Kinetics of a twin step. *Math. Mech. Solids*, 19(7):832–851, 2014.

[9] N. Flytzanis, S. Crowley, and V. Celli. High velocity dislocation motion and interatomic force law. *J. Mech. Phys. Solids*, 38:539–552, 1977.

[10] V. Celli and N. Flytzanis. Motion of a screw dislocation in a crystal. *J. Appl. Phys.*, 41(11):4443–4447, 1970.

[11] S. Ishioka. Uniform motion of a screw dislocation in a lattice. *J. Phys. Soc. Japan*, 30(2):323–327, 1971.

[12] V. F. Nesterenko. *Dynamics of Heterogeneous Materials*. Springer, New York, 2001.

[13] Surajit Sen, Jongbae Hong, Jonghun Bang, Edgar Avalos, and Robert Doney. Solitary waves in the granular chain. *Phys. Rep.*, 462(2):21 – 66, 2008.

[14] C. Coste, E. Falcon, and S. Fauve. Solitary waves in a chain of beads under Hertz contact. *Phys. Rev. E*, 56(5):6104–6117, 1997.

[15] E. B. Herbold and V. F. Nesterenko. Shock wave structure in a strongly nonlinear lattice with viscous dissipation. *Phys. Rev. E*, 75:021304, Feb 2007.

[16] Alain Molinari and Chiara Daraio. Stationary shocks in periodic highly nonlinear granular chains. *Phys. Rev. E*, 80:056602, Nov 2009.

[17] N. Boechler, G. Theocharis, S. Job, P. G. Kevrekidis, Mason A. Porter, and C. Daraio. Discrete breathers in one-dimensional diatomic granular crystals. *Phys. Rev. Lett.*, 104:244302, 2010.

[18] C. Chong, P. G. Kevrekidis, G. Theocharis, and C. Daraio. Dark breathers in granular crystals. *Phys. Rev. E*, 87:042202, 2013.

[19] C. Chong, F. Li, J. Yang, M. O. Williams, I. G. Kevrekidis, P. G. Kevrekidis, and C. Daraio. Damped-driven granular chains: An ideal playground for dark breathers and multibreathers. *Phys. Rev. E*, 89:032924, 2014.

[20] G. James. Nonlinear waves in Newton's cradle and the discrete p-Schrödinger equation. *Math. Mod. Meth. Appl. Sci.*, 21(11):2335–2377, 2011.

[21] G. James, P. G. Kevrekidis, and J. Cuevas. Breathers in oscillator chains with Hertzian interactions. *Phys. D*, 251:39–59, 2013.

[22] Stéphane Job, Francisco Santibanez, Franco Tapia, and Francisco Melo. Wave localization in strongly nonlinear Hertzian chains with mass defect. *Phys. Rev. E*, 80:025602, Aug 2009.

[23] G. Hoogeboom and P. G. Kevrekidis. Breathers in periodic granular chain with multiple band gaps. *Phys. Rev. E*, 86:061305, 2012.

[24] G. Theocharis, M. Kavousanakis, P. G. Kevrekidis, C. Daraio, M. A. Porter, and I. G. Kevrekidis. Localized breathing modes in granular crystals with defects. *Phys. Rev. E*, 80:066601, 2009.

[25] G. Theocharis, N. Boechler, S. Job, P. G. Kevrekidis, M. A. Porter, and C. Daraio. Intrinsic energy localization through discrete gap breathers in one-dimensional diatomic granular crystal. *Phys. Rev. E*, 82:056604, 2010.

[26] S. Aubry. Breathers in nonlinear lattices: Existence, linear stability and quantization. *Phys. D*, 103(14):201–250, 1997.

[27] S. Flach and A. Gorbach. Discrete breathers: advances in theory and applications. *Phys. Rep.*, 467:1–116, 2008.

[28] L. Bonanomi, G. Theocharis, and C. Daraio. Wave propagation in granular chains with local resonances. *Phys. Rev. E*, 91:033208, 2015.

[29] G. Gantzounis, M. Serra-Garcia, K. Homma, J. M. Mendoza, and C. Daraio. Granular metamaterials for vibration mitigation. *J. Appl. Phys.*, 114:093514, 2013.

[30] P. G. Kevrekidis, A. Vainchtein, M. Serra Garcia, and C. Daraio. Interaction of traveling waves with mass-with-mass defects within a Hertzian chain. *Phys. Rev. E*, 87:042911, 2013.

[31] E. Kim and J. Yang. Wave propagation in single column woodpile phononic crystal: Formation of tunable band gaps. *J. Mech. Phys. Solids*, 71:33–45, 2014.

[32] E. Kim, F. Li, C. Chong, G. Theocharis, J. Yang, and P.G. Kevrekidis. Highly nonlinear wave propagation in elastic woodpile periodic structures. *Phys. Rev. Lett.*, 114:118002, 2015.

[33] H. Xu, P.G. Kevrekidis, and A. Stefanov. Traveling Waves and their Tails in Locally Resonant Granular Systems. *J. Phys. A: Math. Theor.*, 48:195204, 2015.

[34] J. Giannoulis and A. Mielke. The nonlinear Schrödinger equation as a macroscopic limit for an osillator chain with cubic nonlinearities. *Nonlinearity*, 17:551–565, 2004.

[35] J. Giannoulis and A. Mielke. Dispersive evolution of pulses in oscillator chains with general interaction potentials. *Discr. Cont. Dyn. Syst. B*, 6(3):493–523, 2006.

[36] G. Schneider. Bounds for the nonlinear Schrödinger approximation of the Fermi-Pasta-Ulam system. *Appl. Anal.*, 89(9):1523–1539, 2010.

[37] Y. Zhen and A. Vainchtein. Dynamics of steps along a martensitic phase boundary I: Semi-analytical solution. *J. Mech. Phys. Solids*, 56:496–520, 2008.

[38] Y. Zhen and A. Vainchtein. Dynamics of steps along a martensitic phase boundary II: Numerical simulations. *J. Mech. Phys. Solids*, 56:521–541, 2008.

[39] B. L. Sharma and A. Vainchtein. Quasistatic propagation of steps along a phase boundary. *Cont. Mech. Thermodyn.*, 19(6):347–377, 2007.

[40] W. Atkinson and N. Cabrera. Motion of a Frenkel-Kontorova dislocation in a one-dimensional crystal. *Phys. Rev. A*, 138(3):763–766, 1965.

[41] A. Carpio and L. L. Bonilla. Oscillatory wave fronts in chains of coupled nonlinear oscillators. *Phys. Rev. E*, 67:056621, 2003.

[42] Y. Y. Earmme and J. H. Weiner. Dislocation dynamics in the the modified Frenkel-Kontorova model. *J. Appl. Phys.*, 48(8):3317–3341, 1977.

[43] O. Kresse and L. Truskinovsky. Mobility of lattice defects: discrete and continuum approaches. *J. Mech. Phys. Solids*, 51:1305–1332, 2003.

[44] M. Marder and S. Gross. Origin of crack tip instabilities. *J. Mech. Phys. Solids*, 43:1–48, 1995.

[45] L. I. Slepyan. *Models and phenomena in Fracture Mechanics*. Springer-Verlag, New York, 2002.

[46] L. I. Slepyan and M. V. Ayzenberg-Stepanenko. Localized transition waves in bistable-bond lattices. *J. Mech. Phys. Solids*, 52:1447–1479, 2004.

[47] L. I. Slepyan, A. Cherkaev, and E. Cherkaev. Transition waves in bistable structures. II. Analytical solution: wave speed and energy dissipation. *J. Mech. Phys. Solids*, 53:407–436, 2005.

[48] L. Truskinovsky and A. Vainchtein. Kinetics of martensitic phase transitions: Lattice model. *SIAM J. Appl. Math.*, 66:533–553, 2005.

[49] A. Vainchtein. Effect of nonlinearity on the steady motion of a twinning dislocation. *Physica D*, 239:1170–1179, 2010.

[50] A. Vainchtein. The role of spinodal region in the kinetics of lattice phase transitions. *J. Mech. Phys. Solids*, 58(2):227–240, 2010.

[51] S. Crowley, N. Flytzanis, and V. Celli. Dynamic Peierls stress in a crystal model with slip anisotropy. *J. Phys. Chem. Solids*, 39(10):1083–1087, 1978.

[52] N. Flytzanis, S. Crowley, and V. Celli. Solitonlike motion of a dislocation in a lattice. *Phys. Rev. Letters*, 39(14):891–894, 1977.

[53] P. Rosakis and A. Vainchtein. New solutions for slow moving kinks in a forced Frenkel-Kontorova chain. *J. Nonlin. Sci.*, 23(6):1089–1110, 2013.

[54] S. Ishioka. Stress field around a high speed screw dislocation. *J. Phys. Chem. Solids*, 36:427–430, 1975.

[55] S. Ishioka. Dynamic formation of a twin in a bcc crystal. *J. Appl. Phys*, 46:4271–4274, 1975.

[56] H. Koizumi, H. O. K. Kirchner, and T. Suzuki. Lattice wave emission from a moving dislocation. *Phys. Rev. B*, 65:214104, 2002.

[57] T. J. Healey and U. Miller. Two-phase equilibria in the anti-plane shear fo an elastic solid with interfacial effect via global bifurcation. *Proc. R. Soc. A*, 463:1117–1134, 2007.

[58] P. J. Swart and P. J. Holmes. Energy minimization and the formation of microstructure in dynamic anti-plane shear. *Arch. Ration. Mech. Anal.*, 121:37–85, 1992.

[59] V. Celli, N. Flytzanis, and S. Crowley. Analysis of the displacement field of a moving dislocation in a crystal. *J. Phys. Chem. Solids*, 37:1125–1133, 1976.

[60] S. Ishioka. A theory of the Peierls stress of a screw dislocation. I. *J. Phys. Soc. Japan*, 36(1):187–195, 1974.

[61] B. Bidégaray-Fesquet, E. Dumas, and G. James. From Newton's cradle to the discrete p-Schrödinger equation. *SIAM J. Math. Anal.*, 45:3404–3430, 2013.

[62] H. Yoshida, C. Chong, E. Charalampidis, P.G. Kevrekidis, and J. Yang. Formation of rarefaction waves in origami-based metamaterials. *arXiv*, page 1505.03752, 2015.

[63] Alexandre Rosas, Aldo H. Romero, Vitali F. Nesterenko, and Katja Lindenberg. Observation of two-wave structure in strongly nonlinear dissipative granular chains. *Phys. Rev. Lett.*, 98:164301, Apr 2007.

[64] R. Carretero-González, D. Khatri, Mason A. Porter, P. G. Kevrekidis, and C. Daraio. Dissipative solitary waves in granular crystals. *Phys. Rev. Lett.*, 102:024102, Jan 2009.

[65] S. Hutzler, G. Delaney, D. Weaire, and F. MacLeod. Rocking Newton's cradle. *Amer. J. Phys.*, 72(12):1508–1516, 2004.

[66] G. James and Y. Starosvetsky. Breather solutions of the discrete p-Schrödinger equation. In R. Carretero-Gonzalez, J. Guevas-Maraver, D. Frantzeskakis, N. Karachalios, P. Kevrekidis, and F. Palmero-Acebedo, editors, *Localized Excitations in Nonlinear Complex Systems*, volume 7 of *Nonlinear Systems and Complexity*, pages 77–115. Springer, 2014.

[67] T. Cretegny and S. Aubry. Spatially inhomogeneous time-periodic propagating waves in anharmonic systems. *Phys. Rev. B*, 55(18):929–932, 1997.

[68] G. James. Periodic travelling waves and compactons in granular chains. *J. Nonlinear Sci.*, 22:813–848, 2012.

[69] E. Fermi, J. Pasta, and S. Ulam. Studies of nonlinear problems. Technical report, I, Los Alamos Scientific Laboratory Report No. LA-1940, 1955.

[70] G. Friesecke and J. A. D. Wattis. Existence theorem for solitary waves on lattices. *Comm. Math. Phys.*, 161(2):391–418, 1994.

[71] G. Friesecke and R. L. Pego. Solitary waves on FPU lattices: I. Qualitative properties, renormalization and continuum limit. *Nonlinearity*, 12:1601–1626, 1999.

[72] G. Friesecke and R. L. Pego. Solitary waves on FPU lattices: II. Linear implies nonlinear stability. *Nonlinearity*, 15(4):1343–1359, 2002.

[73] G. Iooss. Travelling waves in the Fermi-Pasta-Ulam lattice. *Nonlinearity*, 13(3):849, 2000.

[74] G. Iooss and G. James. Localized waves in nonlinear oscillator chains. *Chaos*, 15:015113, 2005.

[75] G. James. Existence of breathers on FPU lattices. *Comptes Rendus de l'Académie des Sciences-Series I-Mathematics*, 332(6):581–586, 2001.

[76] G. James. Centre manifold reduction for quasilinear discrete systems. *J. Nonlin. Sci.*, 13(1):27–63, 2003.

[77] G. Friesecke and R. L. Pego. Solitary waves on Fermi-Pasta-Ulam lattices: IV. Proof of stability at low energy. *Nonlinearity*, 17(1):229–251, 2004.

[78] P. G. Kevrekidis. Non-linear waves in lattices: past, present, future. *IMA J. Appl. Math.*, 76(3):1–35, 2011.

[79] J. Cserti. Application of the lattice Green's function for calculating the resistance of infinite networks of resistors. *Am. J. Phys.*, 85(15):896–960, 2000.

[80] J. Kratovchil and V. L. Indenbom. The mobility of a dislocation in the frenkel-kontorova model. *Czech. J. Phys. B*, 13:891–894, 1963.

[81] J. H. Weiner and W. T. Sanders. Peierls stress and creep in a linear chain. *Phys. Rev.*, 134(4A):1007–1015, 1964.